FÁBIO YE LIN

O papel da morfologia de partícula na sinterização a frio do cerâmico Niobato de Sódio e Potássio (KNN)

The role of particle morphology in the cold sintering of Potassium Sodium Niobate (KNN) ceramic

Universidade de Aveiro
Ano 2021

FÁBIO YE LIN

O papel da morfologia de partícula na sinterização a frio do cerâmico Niobato de Sódio e Potássio (KNN)

The role of particle morphology in the cold sintering of Potassium Sodium Niobate (KNN) ceramic

Dissertação apresentada à Universidade de Aveiro para cumprimento dos requisitos necessários à obtenção do grau de Mestre em Engenharia de Materiais, realizada sob a orientação científica da Professora Doutora Maria Elisabete Jorge Vieira Costa, Professora Auxiliar, e do Doutor Maxim Ivanov, Investigador, ambos do Departamento de Engenharia de Materiais e Cerâmica da Universidade de Aveiro.

Dissertation presented to the University of Aveiro to fulfill the necessary requirements to obtain a Master's degree in Materials Engineering, carried out under the scientific guidance of Professor Maria Elisabete Jorge Vieira Costa, Assistant Professor, and Doctor Maxim Ivanov, Researcher, both from the Department of Materials and Ceramics Engineering at the University of Aveiro.

O júri

Presidente   Prof. Doutora Ana Maria de Oliveira e Rocha Senos
Professora Associada da Universidade de Aveiro

Prof. Doutor José Ramiro Afonso Fernandes
Professor Auxiliar da Universidade de Trás-Os-Montes e Alto Douro

Prof. Doutora Maria Elisabete Jorge Vieira Costa
Professora Auxiliar da Universidade de Aveiro

Agradecimentos

Este trabalho é o culminar de uma longa jornada académica que chegou ao fim. Como não podia deixar de ser, aqui deixo palavras de gratidão a todos aqueles que me acompanharam durante esta etapa, deveras importante, da minha vida.

Em primeiro lugar, agradeço à minha orientadora, professora doutora Elisabete Costa, pelo empenho demonstrado, conhecimento transmitido e, sobretudo, por ter acreditado em mim. Agradeço ao doutor Maxim (coorientador) e à professora doutora Paula Vilarinho, pelo interesse neste trabalho e por terem feito contribuições importantes.

Agradeço à Anna e à Camila, atualmente alunas de doutoramento :), pela paciência que tiveram em ensinar, discutir e ajudar no que fosse possível, dando-me sempre motivação quando o trabalho não corria da melhor maneira.

Agradeço aos meus colegas e amigos, em especial Ricardo, Edna, Patrícia, e Leandro, pelas conversas aleatórias e companhia prestada.

Um obrigado ao Rui e ao Dr. Alex por me terem ajudado nas medidas elétricas. Aos colegas da Electroceramics group, em especial ao João e Manuel, um obrigado pelo ambiente de trabalho descontraído e agradável.

Obrigado ao pessoal do Demac, engenheiras Ana, Célia e Marta, engenheiro Artur e Sr. Jacinto, pelas análises e contribuições para a concretização deste trabalho.

À minha irmã, obrigado pela companhia e preocupação.

Aos meus irmãos gémeos, agradeço a companhia e preocupação. Adorei os nossos fins de semana, com caminhadas e conversas variadas, interessantíssimas, que eram sempre momentos de desabafo, descontração, lazer e muita reflexão. :)

Por fim, aos meus pais e avós, agradeço pelo suporte dado ao longo destes anos todos.

Palavras-chave

Processo de Sinterização a Frio, piezoelétricos livres de chumbo, niobato de sódio e potássio, KNN, tamanho de partícula

Resumo

A sinterização sempre foi uma etapa crítica no ciclo de vida dos cerâmicos técnicos. As elevadas temperaturas de processamento convencional, que se repercutem em acentuados gastos energéticos e elevadas taxas de emissão de CO_2, tem exigido esforços da comunidade científica para identificar alternativas mais sustentáveis. Nesse sentido, a sinterização a frio (CSP) surge como uma técnica alternativa promissora, que combina a pressão com um *solvente*, a baixas temperaturas (<300 ºC), para conseguir cerâmicos com elevada densificação. No presente trabalho, estudou-se a sinterização a frio de um cerâmico piezoelétrico à base de niobato de sódio e potássio (KNN), candidato à substituição dos piezoelétricos à base de chumbo. O estudo incidiu no parâmetro morfologia de partícula, nomeadamente no tamanho e distribuição de tamanho de partícula de partida do KNN, dado tratar-se de um aspeto ainda não explorado na literatura. O controlo do tamanho de partícula foi conseguido através de diferentes tipos de moagem e suas combinações, a planetária convencional (BM) e a moagem por atrito (AM). Foram obtidos pós com tamanho médio e curvas de distribuição de tamanho diferentes, aos quais foram também caracterizados em termos de composição de fases cristalinas (DRX), morfologia de partícula (SEM) e área superficial específica (adsorção gasosa (isotérmica de BET)). Os cerâmicos foram produzidos num sistema de sinterização a frio a 250 ºC, 500 MPa, e assistidos por um fluxo baseado numa mistura de hidróxidos de sódio e de potássio. Comprovou-se que é possível impactar positivamente a sinterização a frio do KNN através da atuação sobre as características do pó de partida, recorrendo a uma distribuição adequada do tamanho de partícula (pós com distribuição bimodal de tamanho de partícula, em torno de ~0.2 e 2 μm). Foi possível alcançar cerâmicos com microestrutura uniforme e densidades relativas elevadas, atingindo cerca de 96%, cujo valores são comparáveis com os dos cerâmicos produzidos convencionalmente a 1120 ºC. Observou-se também que os cerâmicos produzidos a partir das partículas mais finas, nas quais se identificou a presença de agregados, evidenciaram microestruturas não uniformes, caracterizadas pela presença de porosidade e de precipitados em certos locais e aos quais se atribuiu os menores valores de densidade relativa final. Apesar dos elevados valores de densidade de alguns dos cerâmicos obtidos é, todavia, necessário aprofundar ainda outros parâmetros, intrínsecos e extrínsecos ao pó, que conduzam à otimização do desempenho final do cerâmico de KNN, designadamente a sua resistência mecânica e as suas propriedades electricas (coeficiente piezoelétrico d_{33}), que se apresentam ainda modestos se comparados com os dos cerâmicos seus congêneres sinterizados pela via tradicional.

keywords

Cold Sintering Process, lead-free piezoelectrics, potassium sodium niobate, KNN, particle size

abstract

Sintering has always been a critical step during the life cycle of technical ceramics. The high temperatures of conventional processing, which are reflected in high energy costs and CO_2 emission rates, have demanded strong efforts from the scientific community to identify more sustainable alternatives. In this sense, cold sintering (CSP) emerges as a promising technique, which combines pressure with a solvent at low temperatures (<300 ºC) to deliver highly densified ceramics. In this work, it was studied the cold sintering of a piezoelectric ceramic based on potassium and sodium niobate (KNN), a candidate for replacing lead-based piezoelectrics. Herein, the study carried out was focused on the influence of the starting powders characteristics, an aspect scarcely reported in the literature, especially for KNN. The control of particle size and size distribution was achieved through different types of milling, conventional planetary (BM) and attrition milling (AM), or a combination of both. The resulting milled powder particles were further characterized in terms of crystal phase composition (DRX), particle morphology (SEM) and specific surface area (gas adsorption (BET isotherm)). The ceramics were produced in a cold sintering system at 250 ºC, 500 MPa, and assisted by a flux based on a potassium and sodium hydroxides mixture. We could demonstrate that it is possible to positively impact the cold sintering of KNN by acting on the characteristics of the starting powder, using an appropriate particle size distribution (particles with a bimodal size distribution centered on ~0.2 and 2 μm). In this case, ceramics with uniform microstructure and high relative densities up to 96%, which are comparable with those of conventionally produced ceramics (1120 ºC), were obtained. It was also observed that ceramics produced with finer starting particles, exhibiting aggregates, evidenced non-uniform microstructure, where the presence of porosity and local precipitates were identified, accounting for lower relative densities. Despite the high density achieved for some of the ceramics, it is still necessary to explore further other parameters, intrinsic and extrinsic to the powder, to improve the performance of the cold sintered ceramics including its mechanical resistance and electrical behavior which are still modest as compared to the corresponding properties of KNN ceramics obtained via conventional sintering.

Content

Figures Index

Tables Index

Abbreviatures

A	Area of the interface
AFM	Atomic Force Microscopy
a_m	Cross-section area of one adsorbed molecule
CS	Conventional Sintering
CSAS	Cold Sintering Assisted Sintering
CSP	Cold Sintering Process
C_{BET}	BET Constant
D	Crystallite Size
d_{33}	Piezoelectric coefficient
D_{BET}	Equivalent particle diameter by BET
E_c	Coercive field
FAST	Field-Assisted Sintering Technique
FS	Flash Sintering
HIP	Hot Isostatic Pressing
HP	Hot Pressing
ICP	Inductively Coupled Plasma
KNN	Potassium Sodium Niobate
KNN-0.1LB	$0.9K_{0.5}Na_{0.5}NbO_3$-$0.1LiBiO_3$
l_0	Initial length
l_T	Length at temperature T
LPS	Liquid Phase Sintering
MS	Microwave Sintering
P	Pressure
PFM	Piezoelectric Force Microscopy
P_r	Remnant polarization
P_s	Saturation polarization
PZT	Lead Zirconate Titanate
SEM	Scanning Electron Microscopy

SF	Shape Factor
SPS	Spark Plasma Sintering
SSA	Specific Surface Area
STEM	Scanning Transmission Electron Microscopy
t	Time
T	Temperature
Tanδ	Dielectric Loss
T_C	Curie Temperature
TEM	Transmission Electron Microscopy
T_m	Melting Temperature
T_{O-T}	Orthorrombic-Tetragonal phase transition temperature
T_{T-C}	Tetragonal-Cubic phase transition temperature
v_m	Molar volume
V_m	Volume of formed monolayer
W_{air}	Weight of dried samples
W_{liq}	Weight of samples immersed in liquid
W_{wet}	Weight of wet samples
XRD	X-Ray Diffraction
YSZ	Yttria-Stabilized Zirconia

Symbols

α_{Total}	Total polarization
β	Corrected line broadening
Δl	Length variation
ε_r	Relative Permittivity or Dielectric Constant
γ	Specific interface energy
ρ	Density
ρ_A	Archimedes density
ρ_G	Geometric density
ρ_r	Relative density
ρ_t	Theoretical density

1. Introduction

Advanced ceramics are high-performance materials that, due to their unique electrical, magnetic, and optical properties, play a key role in the microelectronics industry. These materials are integrated into several components such as actuators, capacitors, resistors, and sensors [1]. Traditionally, these technical ceramics are processed at high temperatures (> 1000 °C) and under long sintering times to reach the appropriate properties for the requirements in service. However, these high sintering temperatures (rendering the ceramic industry a high energy intensive sector) raise concerns regarding the carbon footprint and the sustainable development for future generations [2]. Therefore, over the past last decades, the scientific community has spared no efforts to reduce these sintering temperatures and/or time, developing sintering alternatives such as Microwave Sintering (MS), Spark Plasma Sintering (SPS), FLASH Sintering (FS), and more recently, the Cold Sintering Process.

The Cold Sintering Process (CSP) is a disruptive method of processing ceramic materials at incredibly low temperatures, that attempts to take an important step towards the goal of a more sustainable Europe and World. The typical temperature range of CSP extends from room temperature to 300 °C, depending on the material to be sintered. CSP is assisted by a transient solvent medium (water, aqueous solution, aqueous suspension, or molten salts) and uniaxial pressure (hundreds of MPa). The transient liquid content usually ranges from 5 to 20 wt.%. Although recent, it is already reported in the literature the feasibility of CSP for a wide spectrum materials such as microwave dielectrics, ferroelectrics, piezoelectrics, semiconductors and solid-state electrolytes [3].

Several variables influence the processability of the material in a CSP system. Factors extrinsic to the material, such as temperature, pressure, time, heating rate, and solvent, are reasonably documented in the literature. In the case of characteristics intrinsic to the material, such as particle size, it is less addressed in the literature. According to the current state of the art, the addition of

nanoparticles in the CSP may improve the final density of cold sintered ceramics and, therefore, its final properties [4,5].

Potassium sodium niobate, (K,Na)NbO$_3$ (KNN), is here introduced as a promising lead-free piezoelectric material for actuator and transducer applications. However, the well-known poor sinterability of KNN is a problem difficult to overcome as a high sintering temperature (T>1000 °C) may easily cause the undesirable volatilization of its alkaline elements, thus affecting the microstructure development and the final stoichiometry of KNN ceramics, with a negative impact in its electrical performance. The influence of the powder's nanometric size in KNN production has been addressed only for conventional sintering. In this case, the downscaling of the starting particles size constitutes a driving force for densification, leading to extremely dense KNN ceramics [6,7], with enhanced final properties.

To date, concerning the information available on CSP of KNN, it has been portrayed only 4 times, and all of them focusing on factors extrinsic to the material (CSP as a tool to lowering the conventional sintering temperature [8], the effect of the solvent – aqueous NaCl solution [9], and the dwell time during [10] and after CSP [11]). So far, there are no reports on the influence of the powder morphology (namely particle size) on the final properties of KNN processed by cold sintering. Besides that, there are no studies correlating the grain size and the final properties on KNN ceramics obtained by CSP. CSP is currently one of the few techniques that can potentially produce samples that retain the initial (nano)crystalline structure while being an environmentally friendly technique. The present work aims to fill the aforementioned gaps and to report the role of the particle size on CSP of KNN ceramics to elucidate particle size effects in KNN ceramics characteristics (microstructure and electrical properties).

This work is organized in 4 chapters.

Chapter 1 (the present chapter) introduces the topic of the work, the organization of the present document and then establishes the main goals to be pursued with the present study. Some of the conventional sintering techniques, their current limitations, and the existing alternatives are then reviewed. In the second part of

chapter 1, the state of the art of Cold Sintering Process is presented. Finally, some generalities related to processing methods, gaps, and study opportunities regarding KNN ceramic (target material of this study) are also adressed. These topics will serve as a basic theoretical frame to support the understanding of the following chapters.

Chapter 2 describes the experimental procedure to produce the powders and ceramics, followed by the characterization techniques used for this work. For each technique, a brief theoretical description was made in order to familiarize the reader with the techniques.

In chapter 3 it is presented the results. The results are presented in the following sequence: a deep characterization of the powders, followed by the physical and microstructural, and then electrical characterizations of the produced ceramics. In this section, it was attempted to establish some correlations between microstructure, properties, and processing.

Chapter 4 summarizes the general conclusions presented throughout the discussion, and presents some suggestions for future work.

1.1. Objectives

The main objective of this dissertation is to study in-depth the influence of the starting powder morphology on the densification behavior and final properties of KNN ceramics processed by CSP. Conventional sintering will also be carried out and will serve as a comparative term to establish how far the electrical functionality of the CSP ceramic was preserved (or even improved) while highlighting the relevance of performing the sintering of KNN at a very low temperature.

The manipulation of the initial particle size will be accomplished by comminution methods, that is, operations that involve crushing, grinding, and milling. In this work, ball and attrition milling methods were used.

Typical characterizations will be made to KNN powders before CSP, and to as-cold sintered KNN ceramics in order to establish a relationship between the particle size and final properties.

The powders will be characterized in crystallographic terms using the XRD technique, and physically using the SEM (morphology), Laser diffraction (particle size distribution), and adsorption (specific surface area) techniques.

For the sintered ceramics the following characterizations were performed:

- Physical, chemical and crystallographic: XRD analysis, density measurement (Archimedes & Geometric), compressive strength, SEM-EDS (microstructure evolution and chemical composition differences);

- Electrical measurements: dielectric constant and dielectric loss as a function of temperature, berlincourt method for d_{33} piezoelectric coefficient, ferroelectric hysteresis tests (P-E), and PFM analysis.

1.2. Sintering process

Sintering is a processing method used to promote controlled densification of ceramic or metallic powder compacts by heating them up to temperatures that range between approximately 50-80% of the material's melting temperature [12,13]. The driving force behind sintering is the reduction of the body´s free surface energy, leading to a minimal energy state (stable and in equilibrium) [13,14]. The total interfacial/surface energy γA, where γ (J/m^2) is the specific surface energy and **A** (m^2) the total surface area, can be reduced by densification or grain coarsening as described by equation 1.1:

$$\Delta(\gamma A) = \Delta\gamma A + \gamma\Delta A \qquad (1.1)$$

With $\Delta\gamma A$ representing the densification component without grain growth and $\gamma\Delta A$ representing the component of the change in surface area due to grain growth (coarsening) [14].

The ceramic microstructure and final properties depend on several variables. The variables can be related 1) directly to the material, such as chemical composition of the starting powder, particle size and size distribution, particle shape, agglomeration state, or 2) to the process, such as the atmosphere, the temperature, and the sintering time [14]. Depending on the presented variables, it should be adopted the most appropriate sintering techniques. Among the most well-known conventional methods are the solid-state sintering and the liquid-assisted sintering, which will be described in the following section [12,14].

1.3. Conventional sintering

Traditionally, ceramic powders may be sintered by two ways: in the solid-state or in the presence of a liquid phase. The process heating elements allow heat transfer to the samples by means of radiation, conduction, and convection [15].

In the solid-state sintering, the green compact is subjected to sufficiently high temperatures, leading to the formation of necks and, consequently, a reshaping of the grains. The reshaping is achieved through solid-state diffusion mechanisms, where there is a gradual replacement of the solid-gas interface by a

solid-solid interface. In this technique, there is no liquid phase formation [16]. The densification phenomenon is commonly divided into three stages: initial, intermediate, and final. In the initial stage, there is a removal of the curvature differences by the relatively accelerated neck growth. At this stage, a slight first retraction occurs. In the intermediate stage, densification continues to progress, being already characterized by interconnected pores with a cylinder-type shape. Here there is already a significant shrinkage of the pores achieving considerable ceramic's body retraction. The final stage begins when the open porosity starts to give way to the closed porosity, approaching a spherical shape. This is a stage identified by the almost total elimination of porosity [12]. The stages of solid-state sintering are schematically represented in figure 1.1.
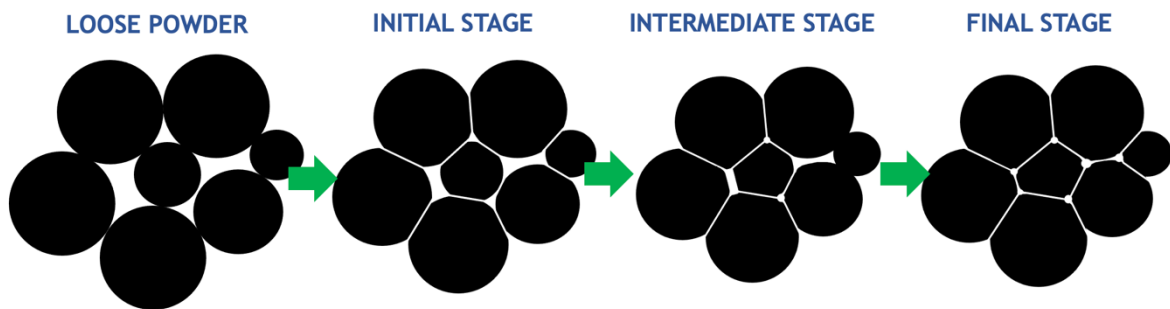
Figure 1.1. Schematic evolution of powder compact morphology during solid-state sintering. Adapted from [17].

The liquid phase sintering (LPS) is assisted by additives and/or impurities that melt at a temperature below the sintering temperature of the material. There is a coexistence of liquid and solid phases. Densification by this technique is dependent on the wettability of the surface, quantity of the liquid, and the solubility of the solid in the liquid [18].

During the LPS, several stages are observed, including compaction, rearrangement, solution-precipitation, and final densification. In compaction, there is an accommodation between grains and additives, still in a solid-state. As the temperature increases, a liquid phase is formed that penetrates between the pores and surrounds the particulate grains. The liquid, through the action of capillary forces on the solid surface, allows the rearrangement of the particles, leading to a rapid retraction. As time progresses, the dissolution of the sharpest

particle edges and subsequent matter precipitation in areas of lower concentration (of solids) begins to become noticeable. Finally, there is a substantial grain growth, accompanied by the expulsion of porosity and subsequent densification [12,18,19]. Figure 1.2. summarizes the main steps resulting from liquid phase sintering.
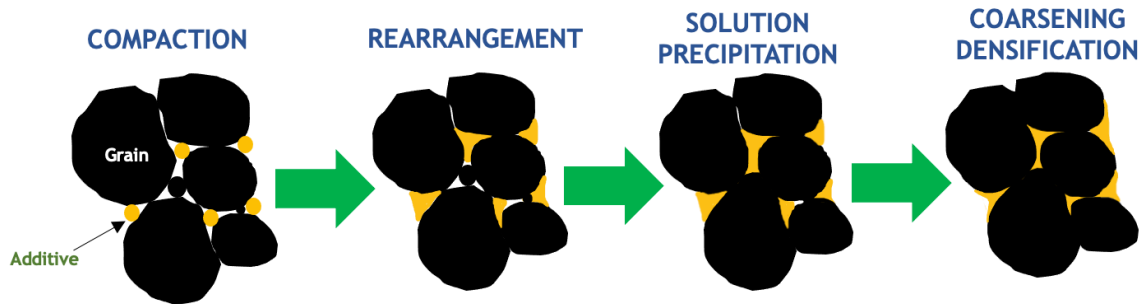
Figure 1.2. Schematic evolution of the powder compact during liquid phase sintering. Adapted from [19].

However, conventional sintering (CS) often presents limited usability, especially in the fabrication of advanced materials. One of its major limitations is related to the co-processing of dissimilar materials (from different categories), due to significant differences in processing temperatures and volatilization of low-temperature phases. Indeed, although the sintering of cermets (e.g. Al_2O_3/Ni, $ZrO_2/Ni/Al_2O_3$, Al_2O_3/Al) is relatively well known, studied, and applied [20], the production of ceramic-polymer and even metallic-polymer composites poses considerable difficulties. This "technological obstacle" limits the combination of properties such as the refractoriness of ceramics or the conductivity of metals with the flexibility of polymers in CS methods [21]. Conventional sintering also limits the production of nanostructured ceramics and nanocomposites due to temperature-induced chemical reactions, decomposition, and undesirable particle coarsening [3].

Over the past two decades, the concerns expressed about high energy expenditures (and costs) and associated carbon dioxide emissions by the industrial ceramic sector are increasingly evident. For instance, in Japan, 8.9% of the overall energy cost is attributed to the ceramics industry [2]. In the United Kingdom´s ceramic industry case, sintering step accounts for 60% of the 10,700 TJ consumed energy. It is said that energy contributes to more than 30% of the manufacturing

cost, depending on the ceramic application and fuel costs [22]. Hence, this industry is responsible for the emission of large amounts of CO_2, being part of the eight industries that emit more CO_2 [23]. The following table shows the CO_2 values emitted in 2012 in the UK. This is a reality that can be transposed to most European countries.

Table 1.1. CO_2 emissions from energy-intensive industries in 2012 [23].

SECTOR	Total annual carbon emissions 2012 (million tonnes CO_2)
Iron and Steel	22.8
Chemicals	18.4
Oil Refining	16.3
Food and Drink	9.5
Pulp and Paper	3.3
Cement	7.5
Glass	2.2
Ceramic	1.3

The high value of CO_2 emission is not very surprising since ceramic materials are mostly processed above 1000 ℃ for several hours [12]. The referred concerns were highlighted with the presentation, in December 2019, of the European Green Deal. The main goal of this pact is to make Europe a continent neutral in terms of greenhouse gas emissions by the end of 2050 [24]. In this sense, CS techniques are very limiting, and alternatively, sustainable sintering techniques are being explored aiming to decrease the dwell temperature and/or sintering time.

1.4. Alternative sintering techniques

Over the last decades, there has been an improvement and development of new methods for sintering materials to produce high-performance ceramic components. These techniques differ from traditional ones in that there is an addition of one or more of the following variables to promote further densification:

pressure, electric/magnetic field and current. They are called pressure-assisted sintering and Field-Assisted Sintering Technique (FAST), respectively. Some of the techniques have been selected and briefly covered in the following sections.

1.4.1. Pressure-assisted sintering

Pressure-assisted sintering techniques uses external pressure to promote the densification of compacts being intensive applied nowadays due to efficiency to produce dense ceramics. These are very suitable for materials that are difficult to sinter in conventional conditions. The products resulting from this process have improved performance, useful for aerospace, biomedical and electronic applications. In the family of pressure-assisted techniques, the most studied, recognized and implemented technologies are hot pressing and hot isostatic pressing [12,25].

In hot pressing (HP), the powder is placed inside a rigid graphite mold that allows induction or resistance heating and subjected to unidirectional pressure along a single axis. Typical pressures range from ~10 to 75 MPa. It is possible to produce, by this method, very dense parts. However, this method is limited by the high cost of production and industrial scaling, being more appropriate for the simple-shape design of expensive and high-performance ceramics like $(Ba,Sr)TiO_3$ and $Pb(Zr,Ti)O_3$ [12,14,25].

Hot isostatic pressure sintering (HIP) uses high temperatures combined with a pressure that is uniformly applied in all directions. The pre-compacted powder is placed in a container (glass or soft metal) and transferred to a pressure vessel. Then heat and pressure (that can reach 30,000 Psi (~200 MPa)) are supplied, with inert gases (Ar or He), for the densification of the material. This technique, like HP, also allows the production of extremely dense materials. As for the advantages over HP, HIP can produce complicated shapes with more uniform density throughout the part. However, it requires tight control of the interface that isolates the material and the environment, as well as avoiding temperature gradients from the surface to the center (can cause dense skins) [12,25,26]. HIP also requires a more complicated equipment structure than HP, as can be seen in figure 1.3.
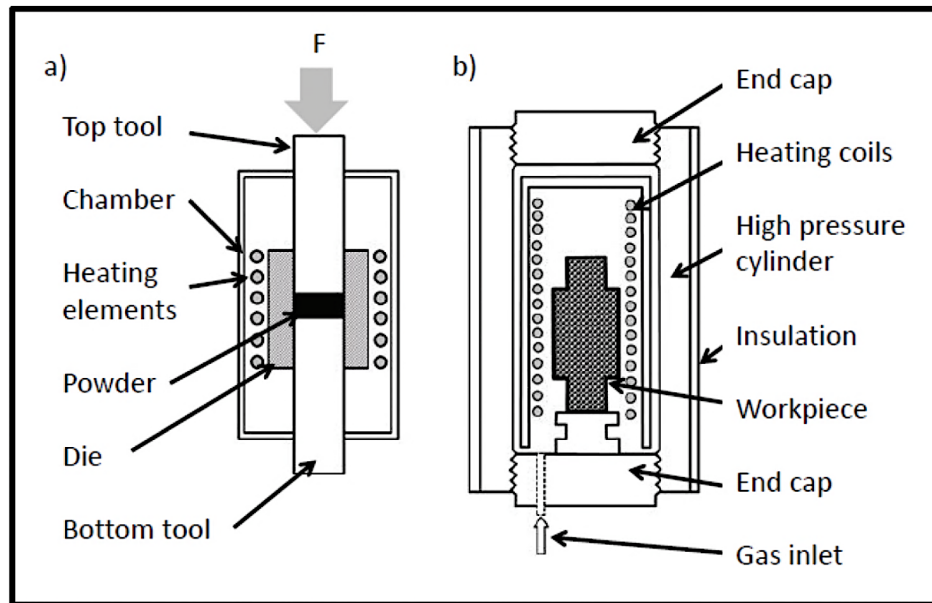
Figure 1.3. A comparison of a) Hot Pressing and b) Hot Isostatic Pressing equipment [27].

1.4.2. Field-Assisted Sintering Techniques (FAST)

Field-assisted sintering techniques (FAST) have become very popular in the research and development community. In fact, by applying electric/magnetic fields, these techniques offer the possibility of sintering a broad spectrum of materials to high relative densities in a short period of time and at lower temperatures with controlled grain growth [28]. Some examples of FAST sintering are described below.

1.4.2.1. Microwave sintering

Microwave sintering (MS) is based on the penetration of electromagnetic microwave radiation by the material, which causes the movement of atoms, ions, and molecules, and generates heat. This phenomenon of the interaction of radiation with the constituents of the material is not transversal for all materials. For example, "opaque" materials such as metals reflect microwaves, therefore, there is no energy transfer. Another example is the material called "transparent" (as is the case of most ceramics at room temperature) that allow the passage of radiation and transmit it without the transfer of energy [29]. Exceptions such as iron oxide, chromium oxide, and silicon carbide absorb microwave radiation at room temperature being called absorbent material. In this case, the natural

resistance of the charge elements (electrons or ions) and dipoles to movement causes a shift from the system in equilibrium to a non-equilibrium system, leading to the dissipation of energy in the form of heating [12,29].

Microwave processing facilitates direct energy transfer to the materials, allowing volumetric heating and not from the surface to the center, as is the case with conventional processes. This type of heating allows simultaneous heating of the heat carriers, walls of an oven or reactor, as well as high heating rates, which can reach up to 1000 °C/min. This allows for a drastic reduction in energy consumption [12,15]. However, it is not always easy to sinter using microwaves, which can cause overheating, unexpected temperature gradients, and cracking due to high heating rates [15].

1.4.2.2. Spark Plasma Sintering

Spark Plasma Sintering (SPS) is based on the consolidation of a powder in a graphite matrix, with the application of pressure and a direct pulsed electric current [30]. The loose powder is placed inside the pressing die and heated through the passage of high-intensity electrical current flow, usually between 1 and 50 kA, under low voltage (<10 V). The pressure is applied, uniaxially, by pistons, which behave like current-carrying electrodes [31]. The experimental setup is similar to Hot Pressing, as shown in the figure 1.4.
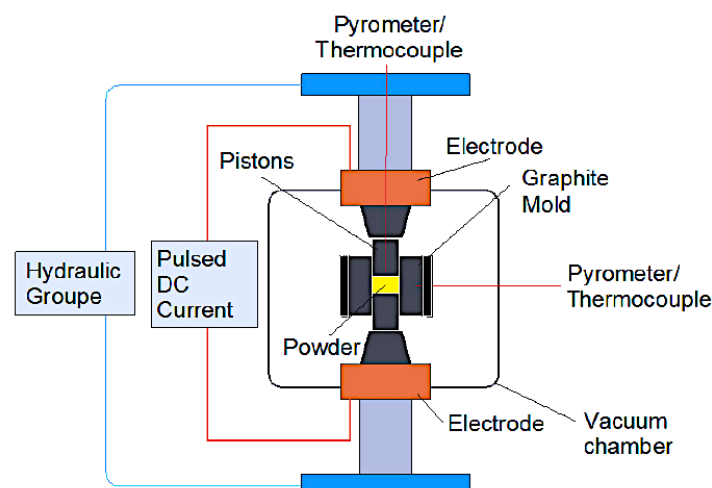
Figure 1.4. Schematic illustration of SPS equipment [32].

Different aspects that characterize this technique and which present themselves as competitive advantages over conventional techniques are 1) rapid heating, reaching hundreds of degrees Celsius per minute, 2) sintering cycles as short as mere tens of minutes, 3) lower temperatures for densification to occur without excessive grain growth, leading to 4) improved mechanical properties of the materials. These attributes are promising for the production of refractory materials such as alumina or zirconia [31]. However, there are also some inconveniences associated with this processing method, which require more control and further research. Some difficulties can be enumerated, such as non-uniform temperature distribution during the heating process, geometric limitations, stress gradients throughout the sample, resistance of graphite die to compression limited to values lower than 150 MPa, and, finally, unfeasible industrial scaling up (expensive equipment) [30,31].

1.4.2.3.   Flash sintering

Flash Sintering (FS) was first reported by Cologna et al. [33] from the University of Colorado. In their work, 3% mol Yttria-stabilized zirconia (3YSZ) was fully densified at 850 °C, with the application of a high voltage electric field (120 V/cm), in a mere 5 seconds. In traditional FS, the electric field is applied directly to the pre-compacted ceramic body during heating in a furnace by means of metal electrodes placed in contact with the parallel face of the sample (figure 1.5-b). Once a certain threshold temperature is reached a sudden non-linear current flux is forced through the sample and densification is achieved in a short time, between a few seconds and a few minutes [34].

The FLASH phenomenon is characterized by a series of simultaneous events, which consists of an abrupt retraction of the ceramic body, accompanied by thermal runaway of the internal Joule heating, a dramatic increase in electrical conductivity, and the emission of bright light.

FLASH sintering is considered a slightly different method than SPS, in that the FS uses higher voltages, leading to high electric fields ranging from 7.5 to 1000 V/cm [35] (it can reach 2250 V/cm as reported by Dows et al. [36] for 8YSZ), and smaller currents, and where in some FLASH setup, pressure is applied only to

promote the contact between the electrode and the ceramic [34]. In figure 1.5. are illustrated some electrode-ceramic body geometries.
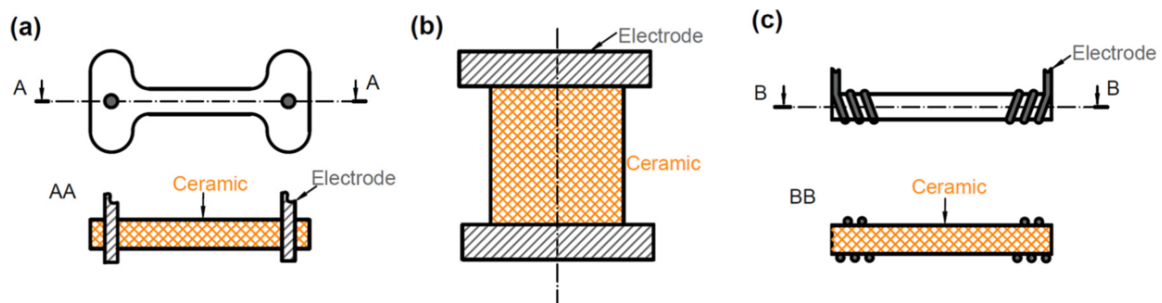
Figure 1.5. Possible geometries for performing FS: a) Bone, b) pellet and c) rope [34].

The FLASH technique is associated with multiple advantages, including cheaper equipment, drastic reduction in processing time and temperature, reduced energy consumption (and costs) with the obvious low environmental impact. However, it can also be mentioned some inconveniences related to this technique. One is that many times, the electric current travels preferential routes, generating unexpected hot spots. These hot spots are aggravated when the materials reach even higher temperatures, generating an avalanche of events that translate into an increase in conductivity and, therefore, greater local current density and power dissipation. This event is contained by carefully setting a current limit from the moment the material is conductive. Another limitation is that in the cases in which conductive pastes are used to improve the conductivity of the contact surface between the ceramic and electrode, it can contaminate the ceramic surface [34].

1.5. Cold Sintering Process

The designation of the cold sintering process (CSP) was established very recently (2016) by a research team led by Professor Clive Randall, from Pennsylvania State University, as a new and innovative liquid-assisted technique for processing ceramic materials at ultra-low temperatures (<300 ºC), using a liquid as a transient solvent and assisted by uniaxial pressure [37]. The way to conduct CSP is extremely simple [38]. Cold sintering starts by introducing a small amount of liquid solution (5-20 wt.%), enough to wet the powder surfaces and

induce an initial dissolution of the sharp edges of the particles [9]. Then, the powder is placed into a mold and adjusted in a press. Usually, the applied uniaxial pressure ranges from 100 to 500 MPa [21], being thus higher than that used in conventional hot pressing. The application of pressure forces the particles to rearrange themselves. The liquid medium facilitates rearrangement as well. As the temperature rises, it eventually causes a phenomenon of dissolution in the surface of the powder, with ions release into the liquid phase. At the threshold temperature (slightly above the boiling point of the solvent), the liquid starts evaporating, and becomes supersaturated, allowing a nucleation phenomenon to take place. The newly formed precipitates are deposited on the surface of the initial powder particles, filling in the voids. By this way, a densified material is produced. It is a process that is highly governed by the principles of LPS and pressure [4,21,39]. A schematic representation of CSP equipment is shown in figure 1.6.

Maria et al. [40] suggested the initial model for CSP, divided into two stages: an initial stage with rearrangement of particles through the application of mechanical forces, followed by a second stage composed of the combination of pressure and temperature action, together with the dissolution and precipitation reactions created by local and global gradients of chemical potential [40].
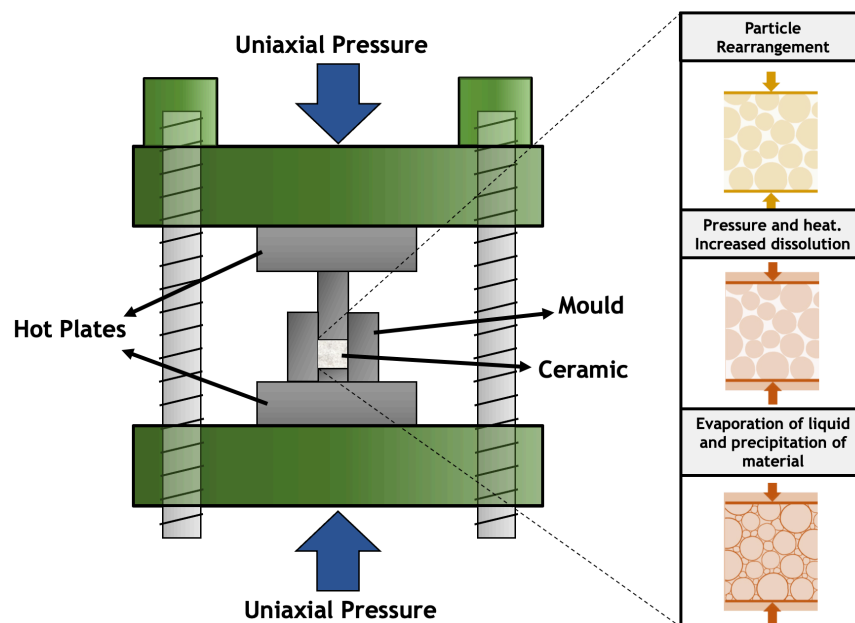
Figure 1.6. Schematic representation of the experimental setup. Adapted from [21,38].

Note that the lowering of the free energy system through processes of dissolution and precipitation is not linear. These reactions can follow two paths: (i) dissolution of ionic species and/or atomic clusters in the liquid, with direct precipitation in areas of low chemical potential or (ii) growth of an intermediate or metastable (amorphous) phase with a higher nucleation rate than that of the stable phases [38]. This point of view is discussed in the following section.

1.5.1. Materials behavior with different solvents

CSP method has been validated for various materials and transient liquids. The selection of the liquid medium is highly dependent on each type of material to be sintered and can act not only as dissolution media, but also as additive or ion source. One of the first systems where is demonstrated the potential of CSP technique is molybdate, which exhibits high solubility in water. Lithium molybdate, Li_2MoO_4, has the potential for microwave dielectric application. J. Guo et al. [41] prepared samples of Li_2MoO_4, using water as a transient phase, low temperature (120 ℃), relatively high pressure (350 MPa) and in a short time (15 min). It is reported values of 95.7% of relative density, ε_r of 5.61, and quality factor Q×F of 30 500. These values are close to those samples produced by the traditional method at 540 ℃, which have ε_r of 5.5 and a quality factor Q×F of 46 000 [41]. NaCl, V_2O_5, KH_2PO_4, and $NaNO_2$ are other examples of highly water-soluble materials that can be relatively easily cold sintering processed (CSPed) [38,41].
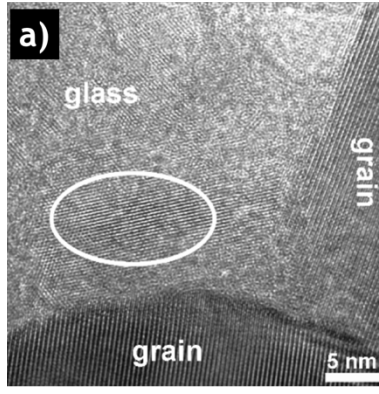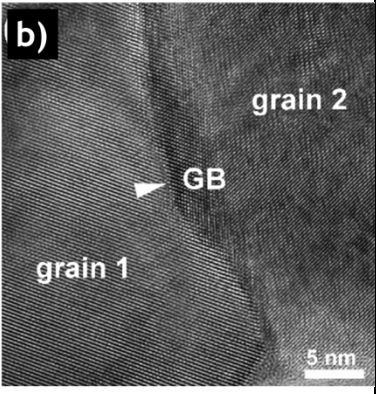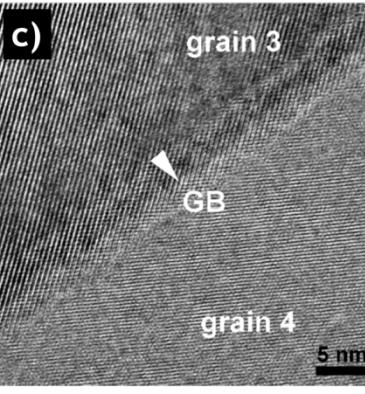
Zinc oxide is another example of a material that has been CSPed, due to its semiconductor characteristics. It is widely used in the electronics industry as varistors. Traditionally, ZnO requires processing temperatures above 1100 ℃, which cause excessive grain growth and deterioration of electrical properties [21]. ZnO is known to be difficult to dissolve in water, so acetic acid is reported as the potential solvent to be used to overcome this obstacle [42].

All materials previously mentioned present a congruent dissolution, i.e., maintains the stoichiometric proportions in the solid and liquid medium after dissolution [37,41]. On the other hand, a wide spectrum of materials with more complex systems, such as bismuth oxide ceramics [39] or ferroelectric titanate-based perovskites, present preferential dissolution of certain elements, which

leads to gradients of composition throughout the piece. This phenomenon limits processing by CSP. Here, the materials are said to be characterized by incongruent dissolution. One of the most prominent and studied examples since the cold sintering process emerged is the barium titanate ($BaTiO_3$) system. This ceramic is important in the multi-layer ceramic capacitor industry, with a conventional processing temperature of ~1400 °C [37]. It is reported in the literature [43] that this ferroelectric is not thermodynamically stable in the aqueous medium, with a pH less than 12, suffering from hydrolysis reactions. The leaching of Ba^{2+} ions from the surface causes concentration disequilibrium, forming a layer rich in amorphous Ti.

Guo et al. [37] explored the CSP on nanoparticles (~ 50 nm) of $BaTiO_3$. To inhibit the dissolution of Ba^{2+} ions from the surface, the authors used a $Ba(OH)_2/TiO_2$ suspension as a Ba^{2+} ion source. The mixture was uniaxially pressed under 430 MPa, firstly at room temperature (25 °C) for 10 min., and then 180 °C for 1 min. to 3h. The results show $BaTiO_3$ ceramic with high relative density (> 93% after only 30 min.). The presence of an amorphous phase revealed in the TEM micrography is indisputable. The amorphous phase acts as a glue that keeps the nanoparticles together resulting into, as said by the authors, a dense crystal/glass "composite". With the application of annealing at 700 °C and 900 °C, there was concomitantly a decrease of amorphous regions (through recrystallization) and improvements in the electrical properties [37](table 1.2.). Annealing is a heat treatment that can remove defects, stabilize the structure, and produce a homogeneous material at temperatures below the conventional processing temperature.

Table 1.2. Effect of CSP and post annealing on microstructure and electrical properties of BaTiO$_3$ [37].

CSP at 180 °C	CSP+ 700 °C	CSP+ 900 °C
a) glass · grain · grain · 5 nm	b) grain 2 · GB · grain 1 · 5 nm	c) grain 3 · GB · grain 4 · 5 nm
Dielectric constant at room temperature (1 kHz)		
70	480	1800
Dielectric Loss at room temperature (1 kHz)		
0.04	0.03	0.03

It is possible to produce BaTiO$_3$, Pb(Zr,Ti)O$_3$, and SrTiO$_3$ titanates at low temperatures by CSP. However, the characteristics such as permittivity and remnant polarization are not comparable to that of materials sintered by conventional methods. These aspects are improved by frequently using subsequent heat treatments at higher temperatures but still below traditional temperatures [21,44].

1.5.2. Effect of particle size and size distribution of the powders

It is well known within materials science that the smaller the average particle size, the faster is the kinetic for the densification [19]. The reason is that smaller particles, like nanoparticles, have a large specific surface area that increases the mechanical contacts, thus increasing the reactivity and dissolution-precipitation process in a liquid medium. Funihashi et al. [42] cold sintered ZnO samples using nanopowders (~240 nm) and acetic acid solution at different concentrations. The authors reported relative densities as high as 98% under an

initial pressure of 387 MPa, cold sintered at 238 ºC, 77 MPa, 1M acetic acid in the water, for 1h.

A very recent study was conducted by Nur and co-workers [5] on the influence of powder characteristics on CSP of nano-sized ZnO, using a FAST/SPS device with steel tool and water as solvent. The authors cold sintered ZnO with different particle size ranges (20-30 nm and 40-100 nm), at 250 ºC, using 1.6−3.2 wt% of water and different pressures (50 & 300 MPa). Particles with a very narrow size distribution (20-30 nm) led to lower densification values, which was attributed to a possible reduced water infiltration and wetting or a stronger cohesive strength of agglomerates. These phenomena lead to higher resistance to externally applied pressure compared to 40-100 nm sized particles.

H. Guo et al. [4] demonstrated the possibility of utilizing nanoparticles as sintering aid to produce $BaTiO_3$ ceramics. The authors resorted to a 1:1 weight ratio of sub-micro/nanoparticles (400/50 nm), adding 25 wt.% of $Ba(OH)_2/TiO_2$ aqueous suspension. The samples were cold sintered under 430 MPa, for 10 min. at room temperature (25 ºC) and then for 1 min to 3h at 180 ºC. In this work it is reported a relative density (ρ_r) as high as ~95%, after only 30 min, and ~98% after annealing at 900 ºC. Interestingly, from Guo et al. work [4], the density and especially dielectric constants found are slightly superior to those verified in their other work [37], where were investigated only the presence of nanoparticles (~ 50 nm, visible in the figure 1.7.a)). This correlation is consistent with other studies about the particle size effects on the final properties of two-step and conventional sintered $BaTiO_3$ [45,46]. It is reported that for particle size below 0.8-1μm, approaching the nanometer scale, the grain boundaries have a more active behavior as ferroelectric domain wall. This results in a dilution of the effect of the ferroelectric (nano)domains [46], combined with a decrease of the tetragonality [47].

The improvement in the final properties of the ceramics prepared starting from the mixture of nanoparticles and sub-micrometric particles, as compared to the one obtained using only nanoparticles, can be attributed to the facilitated packing of the particles in the initial stage of the CSP, where the nanoparticles can fill the spaces between coarser particles (figure 1.7. b). Table 1.3. gathers

some information regarding the influence of CSP on different $BaTiO_3$ and ZnO nanoparticle systems.
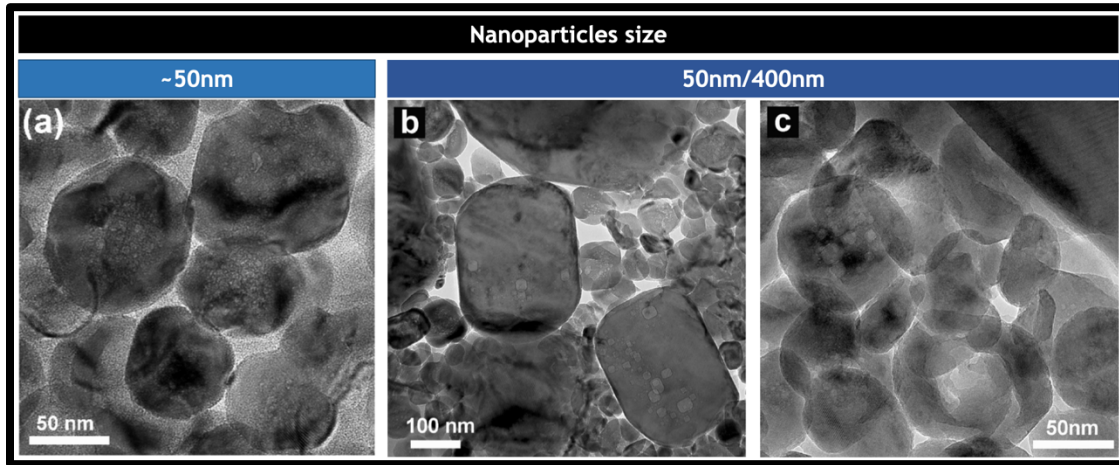
Figure 1.7. TEM images of cold-sintered (180 °C) $BaTiO_3$ nanoparticles [4,37].

Table 1.3. Summary of cold Sintering on $BaTiO_3$ and ZnO nanoparticles. These values were achieved without annealing.

Material	Solvent	Particle size (nm)	CSP	Grain size (nm)	ρ_r (%)	Dielectrical properties 1MHz (T_{room})	Ref.
ZnO	H_2O (1.6 wt%)	20-30	T=250 °C P=300 MPa t=5 min.	—	77.08	—	[5]
		40-100			92.37		
	H_2O (3.2 wt%)	40-100	T=250 °C P=300 MPa t=10 min.	108	96.36		
			T=250 °C P=300 MPa t=60 min.	~138	99.17		
$BaTiO_3$	$Ba(OH)_2/TiO_2$ (25 wt%)	50/400	T=180 °C P=430 MPa t=30 min.	—	95	$\varepsilon_r \approx 160$ $\tan \delta \approx 0.01$	[4]
	$Ba(OH)_2/TiO_2$ (25-26 wt%)	50		—	93	$\varepsilon_r = 65$ $\tan \delta = 0.01$	[37]
	NaOH/KOH (4 wt%)	20	T=300 °C P=520 MPa t=12 h	150	92	$\varepsilon_r = 1830$ $\tan \delta = 0.01$	[47]
	NaOH/KOH (6wt%)			75	96	$\varepsilon_r = 690$ $\tan \delta = 0.01$	

Notwithstanding, there is a need for further studies on the particle size effect for other CSPed systems such as KNN-based ferroelectrics. It is evidenced in the literature that conventional sintering using nanoparticles as a starting point benefit the physical and piezoelectrical characteristics of KNN ceramics. The results are summarized in section 1.6.1. Details can be consulted in the respective references [6,7].

1.5.3. Process variables: solvent, pressure, temperature and time

Recently Tsuji et al. [47] adopted the nanometric size of the powders (20 nm), as well as increased pressure and time applied during CSP of $BaTiO_3$ ceramics (520 MPa for 12 h vs 430 MPa for 3h from Guo and colleagues [37]), and alteration of the transient environment. H. Guo et al. used a suspension of $Ba(OH)_2/TiO_2$ [37], while Tsuji et al. [47] resort to a flux of NaOH/KOH (4-6 wt.% in a 50:50 M ratio). The hydroxide flux has the function of acting as a sintering additive, avoiding subsequent treatment at higher temperatures. It is said that it can heavily contribute to densification through pressure-solution creep. The authors were able to produce samples with 92-96% of the theoretical density with values that can reach up to 1830 of relative permittivity and dielectric loss of 0.04 at room temperature and, at 10 MHz. These are comparable to the values presented in [37], which resorted to a heat treatment after CSP.

The case reported by Tsuji and colleagues is important in understanding the role of the different extrinsic factors that come into play in the CSP. It is plausible to say that it is proven that higher pressure and temperature of CSP, combined with longer plateau times and more reactive solvent in cold sintering, lead to ceramic with more suitable properties [37,47]. Be aware of the fact that there is little ambiguity in this conclusion since multiple variables are changed from study to study. Therefore, the conclusion drawn is general, and there may always be exceptions.

Regarding heat treatment after CSP, a study conducted by L. Cong et al. [11] evaluates the influence of the dwell time on the optical properties of a KNN-0.1LB ceramic. The authors conclude that for residence times longer than 24 h, there is a degradation of properties, with abnormal grain growth and undesirable

volatilization of the most volatile elements. The details are summarized in point 1.5.2.

It is also important to note that, generally, when the annealing temperatures approach the CS temperature (without undesirable volatilization compounds of the ceramic material) the final physical and mechanical properties are enhanced. This is well demonstrated for ZrO_2-based ceramics CSPed at 180 °C and 350 MPa, and further annealed at 500—1100 °C for 3h. It should be pointed out that the conventional sintering temperature of this technical ceramic reaches values close to ~1400 °C or higher. The following shows the graphical evolution of both density and Vickers hardness as a function of temperature [48].
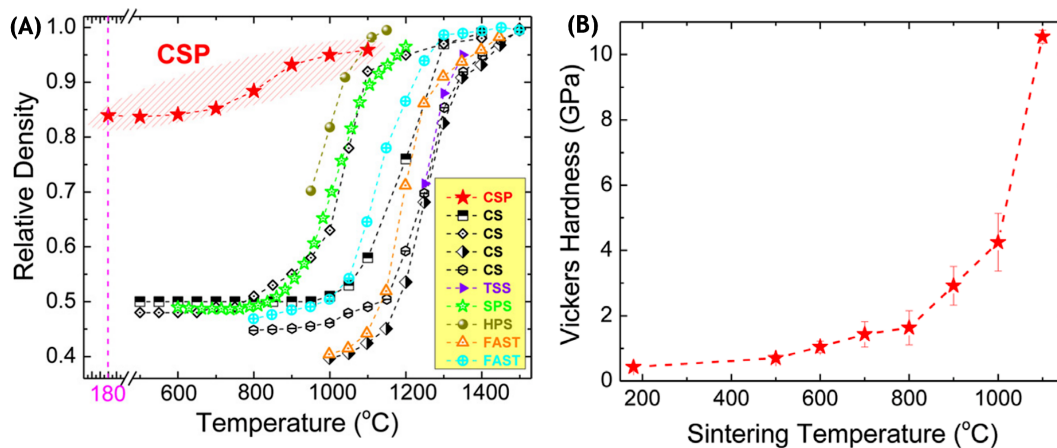
Figure 1.8. Data compiled by Guo et al. on (A) relative density as function of temperature. TSS—Two-Step Sintering. (B) Vickers Hardness of cold-sintered 3Y-TZP (3%mol-Tetragonal stabilized zirconia) [48].

1.5.4. Advantages and applications

So far, from the bibliography reviewed, CSP is a method capable of processing ceramics at low temperature. The low temperature allows reducing the associated energy costs. However, it is important to know how these expenses are placed when compared with more traditional methods. Table 1.4. shows the energy consumption of the different techniques to produce $BaTiO_3$. CSP at 300 °C of $BaTiO_3$ allows a drastic reduction in energy consumption by two orders of magnitude when compared to the conventional method (1400 °C), leading to the reduction of CO_2 emissions into the atmosphere [21].

Table 1.4. Energy consumption for diferent techniques to produce Barium Titanate. Reproduced from [21].

Sintering method of $BaTiO_3$	Energy consumption kJ/g
Solid-state	2800
Liquid phase	2000
Field assisted	1050
Microwave	540
Fast firing	130
Cold sintering	30

Low-temperature processing opens up opportunities for the manufacture of new materials with unique characteristics, such as ceramic-polymer, ceramic composites with nanoparticle integration [3] and nanostructured ceramics. It has already been shown that CSP is effective in the production of ceramic-polymer composites such as $BaTiO_3$-PTFE with improved dielectric properties [49], ZnO designed with resistive grain boundary through the addition of polyetherimide (PEI) [50] or polytetrafluoroethylene (PTFE) [51] for varistors, etc. On several occasions, the presence of small volume amount of nanoparticles improved the mechanical and electrical properties [37]. Table 1.5 summarizes some details of processing ceramics with nanofillers (directly retrieved from [3]).

Table 1.5. CSP of ceramics-based composites with nanofillers. Reproduced from [3].

Ceramic	Nanofiller	Liquid	Sintering condition	Relative density (%)	Property design
$LiFePO_4$	Carbon fiber	LiOH solution	180 °C, 240 MPa for 10 min.	70-89	Enhanced mixed electrical/ ionic conduction
ZnO	MXene $Ti_3C_2T_x$ 2D powders	1.5 M acetic acid	300 °C, 250 MPa for 1h.	92-99	Enhanced mechanical and electronic properties
V_2O_5	Carbon nanotubes/ fibers	Deionized water	120 °C, 350 MPa for 20 min.	84-95	Enhanced conductivity

In fact, CSP can consolidate materials to near full density, with possibility to produce ceramic matrix composites with incorporated polymers, improved functional properties, and integration in 3D printing. Examples of applications include batteries, microwave dielectric composites, multilayer capacitors, semiconductors and proton conductors [52].

1.6. Potassium-sodium niobate ceramic

Piezoelectric materials are widely disseminated in the electrical and electronic industry. These are materials capable of producing an electrical potential in response to mechanical stress or producing a mechanical response in function of an electric field [53]. To date, lead zirconate titanate, $PbZr_xTi_{1-x}O_3$ (PZT), and related compositions have dominated the market of actuators and transducers, since they have the best piezoelectric characteristics [54]. However, this material has also brought immense attention in recent decades due to the large amounts of lead present in its composition (it can exceed 60 wt.%) that are harmful to human health and the environment [55]. The European directive (2003) requires that toxic materials such as PZT be replaced by safe or safer materials as soon as the advancement of science allows it [56].

The ceramic based on potassium sodium niobate ((K,Na)NbO$_3$), abbreviated to KNN, is one of the most promising candidates to replace PZT piezoelectrics, due to its composition free of lead and satisfactory electrical properties (d$_{33}$ coefficient and relative dielectric permittivity (ε_r) of 80 pC/N and ~ 290, respectively) [55].

KNN is a solid solution of KNbO$_3$ and NaNbO$_3$, as shown in the phase diagram in figure 1.9. Currently, the most studied composition is K$_{0.5}$Na$_{0.5}$NbO$_3$ (marked in orange in the phase diagram) because it gathers the best dielectric and piezoelectric properties [55,57,58]. At room temperature, KNN has an orthorhombic structure. Around 200 ℃, there is a transformation from orthorhombic to tetragonal phase. Slightly above 400 ℃, the transformation from the tetragonal to the cubic phase occurs. In this temperature range, KNN loses its ferroelectric properties and becomes a paraelectric material. This is called the Curie point of the material. As the temperature increases, solidus and liquidus temperatures are reached, 1140 ℃ and 1280 ℃, respectively [58].
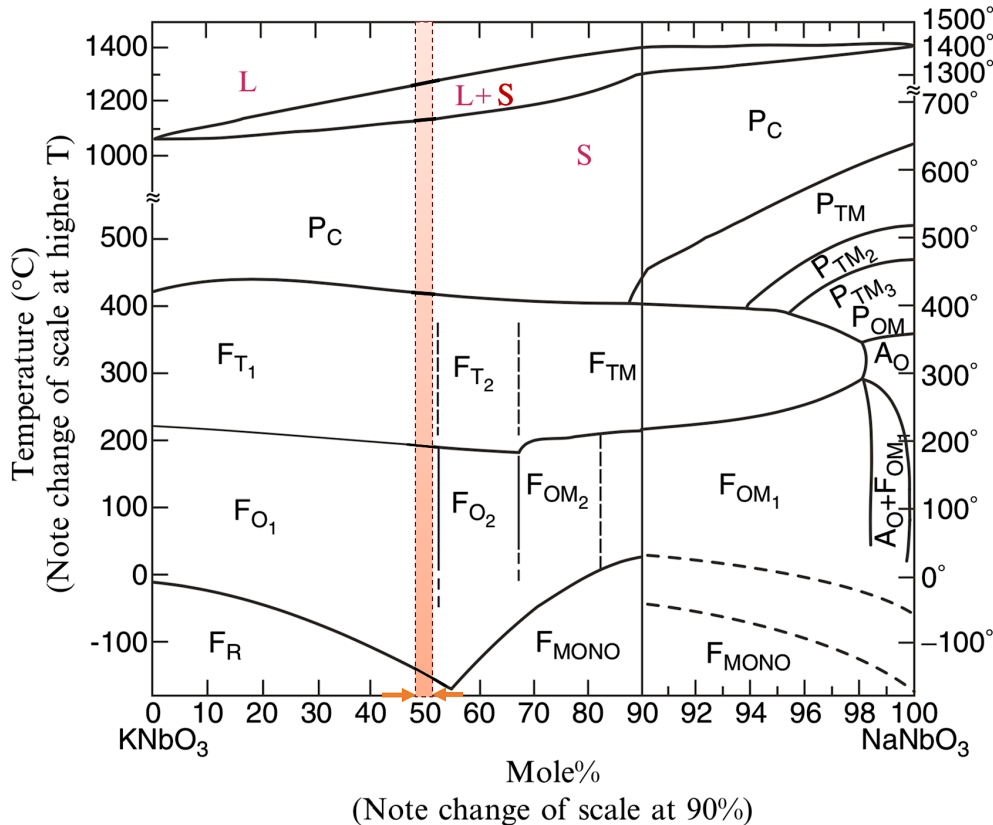
Figure 1.9. Binary phase diagram KNbO3−NaNbO3 [58].

From figure 1.10. it can be observed the typical dielectric curve of KNN ceramics There is the expected evolution of the unit cell as well as the dielectric properties in function of temperature. Each peak in the dielectric constant curve corresponds to a phase transition. In this perovskite system, ABO_3, the A-site (red balls) represent the alkaline elements Na and K, the B-site (green ball) represents the atom of Nb, and, finally, the blue balls represent the oxygen atoms [55].
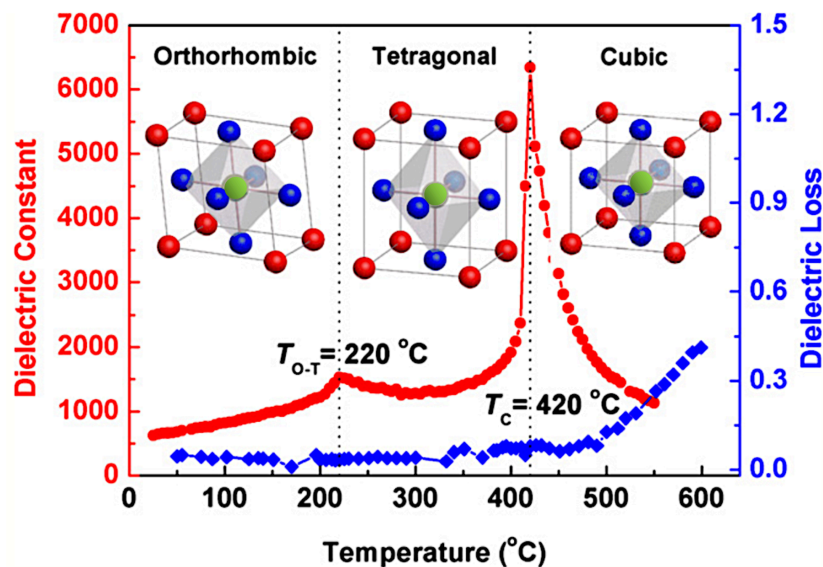
Figure 1.10. Dielectric constant, loss, and unit cell geometry as a function of temperature [55].

1.6.1. Processing of KNN ceramics

Traditionally, KNN powder is obtained from the calcination of a mixture of K_2CO_3, Na_2CO_3, and Nb_2O_5 powders, in the appropriate proportions, at temperatures between 900 and 950 °C, close to the melting point of the Na_2CO_3 and K_2CO_3 alkalis (T_m = 851 °C and T_m = 891 °C, respectively) [57,58]. This can cause a deficit of A-site cations, which are volatile at high temperatures. Bomlai et al. [59] showed that it is possible to calcinate KNN at 600 °C for 2 hours. However, the composition homogeneity was only reached at 900 °C. The addition of an excess of 5 mol% of alkalis allowed the calcination temperature to be lowered to 800 °C. The addition of excess alkalis resulted in a change in morphology, from almost spherical shapes to cubes, as well as an increase in the average grain size (figure 1.11). The increase in the average grain size may be due

to the formation of a liquid phase that recrystallized. The authors also prove that the longer the calcination time and higher temperature is, the larger the average particle size [59].
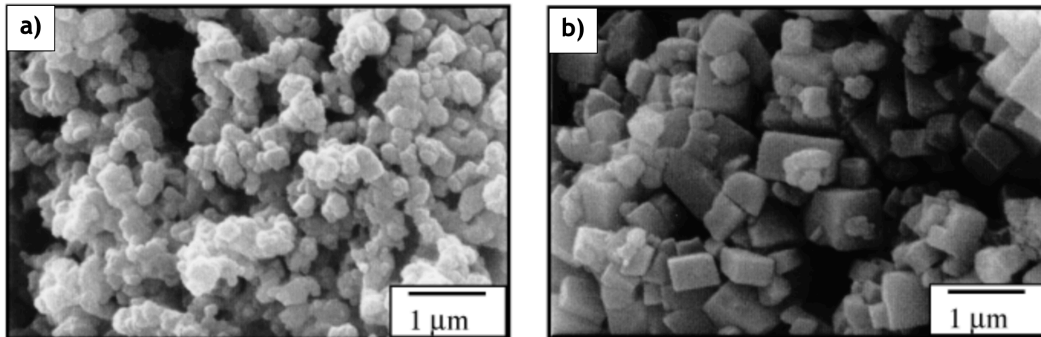
Figure 1.11. Scanning electron microscopy of the calcined KNN powders: a) without excess at 900 °C and b) 5%mol alkali excess at 800 °C [59].

Conventional sintering of KNN, like the calcination step, also leads to the volatilization of alkaline compounds, and stoichiometric disequilibrium since it is carried out at extremely high temperatures, generally ranging between 1100 to 1120 °C, to guarantee densifications above 90% [55,57,58]. One way to improve the sinterability of KNN compounds is also to add an excess of alkaline K/Na, as shown by Y. Lee et al [60]. The proportion 0.62/0.31 mol% of K/Na resulted in the production of a stoichiometric compound at the grain boundary (not specified by the authors) that limited the grain growth and favored the densification mechanism [60].

Another way to improve sinterability is to reduce the size of the initial powder since, in the smaller particles, there is a substantial increase in contact points with an increase in the compaction and kinetic for densification of the ceramic. This fact is demonstrated by two groups of authors. R. Zuo et al. [6] produced KNN powders with average sizes between ~ 70 nm and 230 nm, using friction milling (6-48 h) with cerium-stabilized zirconia balls. The sintering was carried out at 1100 °C for 4 hours. It is shown that for samples where the initial particle size was smaller (longer milling times), the relative density increases to 98.4%. C. Jiten et al. [7], like Zuo and colleagues, also resorted to the milling of powders by friction (10-20 h) and reached the same conclusion for the lead-free

$(K_{0.5}Na_{0.5})(Nb_{0.9}Ta_{0.1})O_3$, KNNT. The sintering took place at 1050 °C for 1h. The summary of physical and electrical properties is shown in the table 1.6.

Table 1.6. Effect of initial particle size in the final properties of KNN-based ceramics (KNN - $Na_{0.5}K_{0.5}NbO_3$; KNNT - $(K_{0.5}Na_{0.5}(Nb_{0.9}Ta_{0.1})O_3)$. ρ_r -Relative density; Tc-Curie temperature; Tanδ – dielectric loss; kp- Coupling factor; d_{33}-piezoelectric coefficient. (*) 1kHz at 25 °C.

Material	Initial particle size (nm)	ρ_r (%)	T_c	ε_r(*)	Tan δ (*)	kp (%)	d_{33} (pC/N)
KNN [6]	230	96	418	558	0.0347	31	92
	140	97.6		564	0.0352	34	99
	80	98		580	0.0392	40	107
	70	98.4		605	0.0436	38	102
KNNT [7]	35	94.2	—	~750	0.6	40	91
	11	94.8		~1100	0.2	43	108
	6	95.4		~3250	0.1	47	123

Both Zuo et al. and Jiten et al. show that particle size reduction enables the production of extremely dense KNNs, with electromechanical properties suitable for lead-free piezoelectric applications [6,7]. It is important to note that Zuo et al. [6] also studied the influence of different metallic oxides on the final properties of KNN. They showed that by doping with 1 mol% of ZnO, an improved sintering behavior and good electromechanical properties were verified (ρ_r = 97%, d_{33}=117 pC/N, and kp=44%).

1.6.2. Studies on Cold Sintering of KNN

It is natural that the study and implementation of innovative sintering techniques are applied to equally "new" and promising materials. Here, CSP emerges as a potential alternative for processing KNN at low temperatures, avoiding the problems verified at high temperature. However, the CSP of KNN ceramics is still very little discussed in the literature. To date, October 2021, only four papers on the subject have been published in the open literature (ex: Web of science).

The first study was carried out by Ma et al. [8], where is compared the effect of cold sintering followed by a high-temperature sintering (Cold sintering assisted sintering — CSAS) with only conventional sintering, in terms of the microstructure and electrical properties of the final ceramic. The solid-state produced powder, whose starting particle size is not specified, was mixed with deionized water in proportions between 5 wt.% and 15 wt.% and submitted to a pressure of 350 MPa at 120 °C, for 30 min. The optimal water content was 10 wt%. The as-prepared ceramics pellets were dried and subjected to sintering for 4 hours at different temperatures (1055-1145 °C) — referred as "CSAS samples".

For comparison, conventional sintering (CS) was carried out. Conventional sintered samples presented relative densities (ρ_r), in green and after sintering (1115 °C, 4h), of 53% and 93-94%, respectively. The observed d_{33} coefficient was around 115-120 pC/N. On the other hand, the ρ_r of the pellets produced right after the CSP exceeds 65% and rises to 96-97% when applying the sintering at 1115 °C. The verified d_{33} coefficient was ~130 pC/N. The improvement in electrical properties is not limited to having less porous and dense KNNs but can also be attributed to the fact that a second phase, $K_4Nb_6O_{17}$, appears. This last compound has a melting point higher than that of KNN ((T_m = 1177 °C and T_m ~1110 °C, respectively), which limits the evaporation of alkaline elements such as potassium [8]. Overall, CSAS samples presented less and smaller pores and, at the same time, larger grains and more uniform distributed grain size as compared to CS ceramics processed at the same temperature (see SEM images in the respective reference) [8].

The second study on the CSP of KNN was conducted by Chi et al. [9]. The authors studied the influence of NaCl on the electrical properties and microstructural development of CSPed KNN ceramics obtained from solid-state produced powder. The authors chose NaCl (20 wt.% solution with a concentration of 0.15g/mL) as a transient solvent since it is reported in the literature that the electrical properties of KNN are improved when there is an excess of Na content over K (stated by Chi et al. [9] from the article [61]). Herein the KNN-3wt.% NaCl was pressed under 420 MPa for 15 minutes at room temperature and then 120 °C for 60 minutes for CSP. The sintering of 3 h is done in a temperature range

between 900 °C and 1100 °C. It is shown that the NaCl solution combined with CSP can extend the sintering temperature range and halt the abnormal grain growth without impairing the electrical properties. Note that besides being a low-temperature melting material, the presence of NaCl, and its dissociation into Na⁺ and Cl⁺, can replace the more volatile alkali element Na at higher temperatures [9]. The volatilization of alkali elements begins to be more expressive at 1080-1100 °C, where density and piezoelectric performance is lowered.

It is demonstrated that CSP does not significantly change the initial particle size and morphology (~0.5 μm and ~0.7 μm, before and after CSP, respectively, and both cubic-shaped) of the powder. On the other hand, higher sintering temperatures lead to larger grains, going from an average of ~0.7 μm of CSPed samples to ~3 μm sintered at 1100 °C (figure 1.12.) [9].
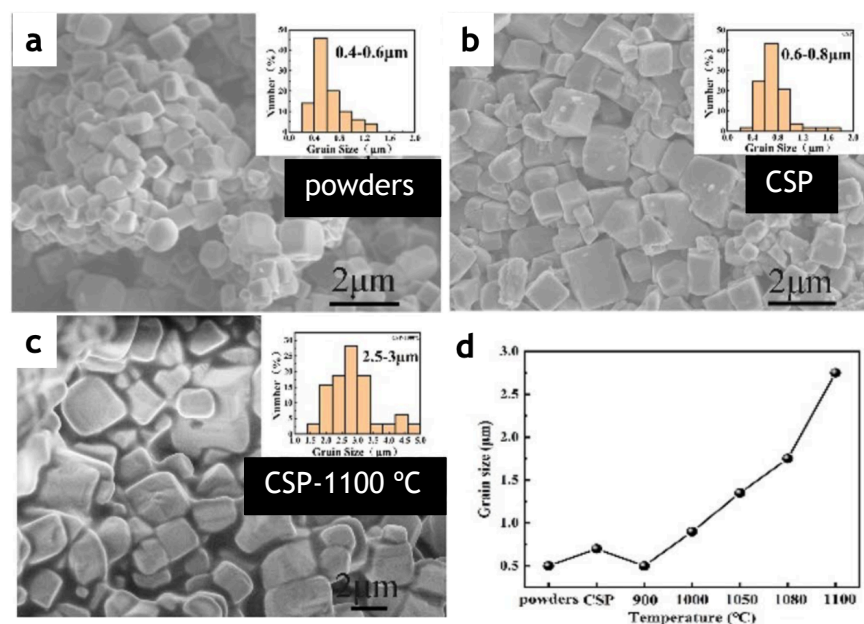
Figure 1.12. Scanning Electron Microscope image of KNN a) powders, b) CSP at 120 °C and c) annealed at 1100 °C. d) Grain size as function of temperature [9].

Similar to BaTiO$_3$, KNN also exhibits an incongruent dissolution in an aqueous medium. The behavior in an aqueous environment shows that, in general, the rate of dissolution of potassium ions is higher than that of sodium and that, in turn, it is higher than that of niobium ion [9,62].

Another study is about transparent KNN for optical applications. Here, L. Cong et al. [11] investigate the CSP and the effect of the plateau time of the subsequent thermal treatment on the transmittance, microstructure, and electrical properties of the $0.9K_{0.5}Na_{0.5}NbO_3$-$0.1LiBiO_3$ (KNN-0.1LB) ceramic, comparing it with conventional sintering. In this work, the transient medium was KOH/NaOH solution (10 mol/L) in 10 wt.% of the solid-state produced powder. The CSP was done at 350 MPa at 350 °C, for 30 min. The sintering after CSP, as well as the CS, was done at 1050 °C from 0 h to 36 h. The ρ_r of CSASed ceramics exceeds 95% for all threshold times. It was reported that over 24-hour dwell time, optical transparency reaches 74% at 900 nm. On the other hand, the authors denoted a decrease in the relative density and Curie temperature (T_c) as the sintering time increases beyond 24h. These facts are due to abnormal grain growth with volatilization of A-cations, which leads to the weakening of ferroelectric effect. Nevertheless, the T_c of the CSASed samples continues to be higher than the values verified in the CS, indicating that the CSP before sintering can optimize the properties of the final sinter [11].

More recently, Deng et al. [10] cold sintered KNN at 350 °C for 4h, under a uniaxial pressure of 400 MPa, and 10 wt % of equimolar ratio of KOH:NaOH as flux. The average grain size after CSP was between 100 and 200 nm, similar to the particle size of the starting powder. By applying a post-annealing treatment at 800 °C for 1h, the authors were able to produce a KNN with enhanced electrical properties (d_{33} of 148 pC/N and ε_r of 829 at 10 kHz).

Table 1.7. A summary of data collected from the literature on cold sintering of KNN.

Material	Processing Conditions	Relative Density	Initial particle size (nm)	Grain size (nm)	Properties a) d_{33} (pC/N) b) ε_r at T_{room} c) Remnant Pol. ($\mu C/cm^2$) d) Coercive field (kV/cm)	Contribution	Ref.
$K_{0.5}Na_{0.5}NbO_3$	350 MPa 120 ℃/30 min. Water (10wt%) + 1115 ℃/4h	96-97	—	—	a) ~130 b) 500-1,000 c) 17.3 d) 8.3	CSP as assisted method to conventional sintering by increasing the green density and inhibiting the volatilization of A-site elements (specially potassium)	J. Ma et al **(2019)** [8]
$K_{0.5}Na_{0.5}NbO_3$	420 MPa 120 ℃/60 min NaCl (20 wt% (0.15 g/mL)) + 900 ℃/3h	~88	500	500	a) 115 b) ~134 c) 19.77 d) 2.5	CSP using NaCl solution before sintering step can lower the sintering temperature. NaCl act as melting material and supress the volatilization of A-site elements	M. Chi et al **(2019)** [9]

$0.9K_{0.5}Na_{0.5}NbO_3$—$0.1LiBiO_3$	350 MPa 120 °C/30 min. KOH/NaOH 10 mol/L (10 wt%)+ 1050 °C/24h	98-99	—	—	a) — b) > 1,750 c) — d) —	K-rich phase induced by dissolution-precipitation during CSP inhibits the volatilization of A-site elements and reduce the grain growth	L. Cong et al (2020) [11]
$K_{0.5}Na_{0.5}NbO_3$	400 MPa 350 °C/ 4h KOH/NaOH + 800 °C/1h	96	~150	725	a) 149 b) 829 c) — d) —	Electrical properties enhancement by post-annealing the CSPed KNN	B. Deng et al (2021) [10]

1.6.3. A summary of what is known so far and literature gaps

From the literature reviewed so far, it is noticeable the role of the various factors that influence the processability and final properties of $K_xNa_{1-x}NbO_3$ ceramics. The stoichiometric composition in the vicinity of x = 0.5 is considered to be the one with the best piezoelectric and ferroelectric characteristics [55]. The interdependence between time and processing temperature of powders and ceramics is sufficiently portrayed in the bibliography [57,58] and properly summarized in the previous points. It should be reiterated that, generally, higher sintering temperatures and longer times lead to denser ceramics, on the other hand, such conditions can cause a decrease in the functional properties of the materials, especially in the case of KNN ceramics. Often, when the volatilization of the elements K and Na occurs, this is compensated by adding in excess of volatile elements [60].

Related to the CSP of KNN, some variables have been studied, ranging from the effect of the different sintering temperature [8] or time during and after the CSP [10,11] to the use of the NaCl solution as a potential medium [9]. However, in these studies, the authors always resorted to high temperatures after the CSP, due to the still unsatisfactory densifications achieved by CSP. These studies were conducted for micrometric/submicrometric starting particles. Starting with a mixture of micro/nanoparticles may constitute a potential route to cold sintering without the necessity of CSP post heat treatment.

Conventional sintering leads to grain growth that eliminate the nanocrystalline nature of particles and limits the achievement and knowledge of sintered samples with nano-sized grains. On the other hand, CSP is currently one of the most attractive sustainable sintering technologies potentially capable to produce ceramic samples that maintain nanocrystallinity, allowing for study opportunities around this theme. The effectiveness of the combination of micro/nanoparticles on the final properties of a CSPed material is briefly demonstrated in the literature [4].

However, there is still no study on the influence of particle size, from the micrometer towards the nanometer scale, on the sinterability and final characteristics of KNN ceramics processed by CSP.

2. Materials and methods

This chapter describes, in detail, the experimental procedure carried out for this dissertation. The flow-chart below summarizes the tasks performed, attempting to provide   clear view of the work sequence.
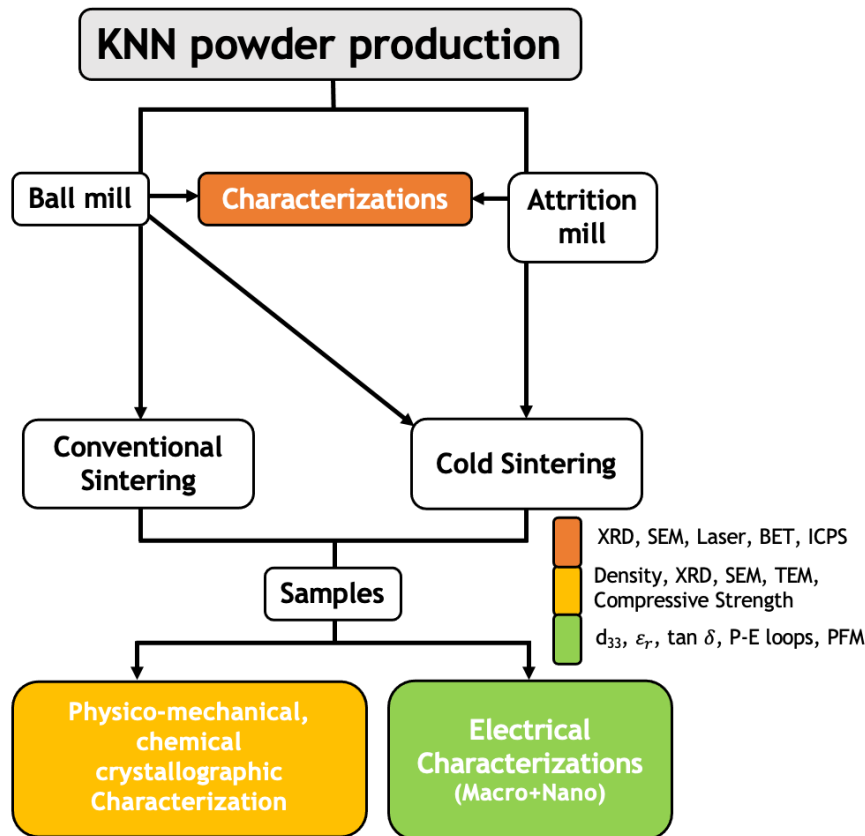
Figure 2.1. (Simplified) Flow-chart of the experimental procedure.

2.1. Powder production

The solid-state reaction is one of the most widely used synthesis method to prepare metal oxides. The production of $K_{0.5}Na_{0.5}NbO_3$ powder by the solid-state route involved alkaline carbonates (K_2CO_3 and Na_2CO_3) and niobium oxide (Nb_2O_5) as precursors. Firstly, K_2CO_3 (Panreac, 99%) and Na_2CO_3 (Alfa Aesar, 99.5%) were dried at 200 °C for 24 h to remove the potential adsorbed moisture. Then, the

dried powders and Nb_2O_5 powder (Sigma Aldrich, 99.9%) were weighed according to the stoichiometric ratio presented below − equation 2.1.

$$K_2CO_3 + Na_2CO_3 + 2Nb_2O_5 \longrightarrow 4\ K_{0.5}Na_{0.5}NbO_3 + 2\ CO_2 \qquad (2.1)$$
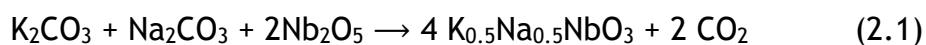
Considering that potential volatilization could occur during the calcination step, 2 wt.% excess of alkaline reagents was added. The carbonates and oxide were placed in a Teflon milling jar with zirconia balls (5, 10 and 15 mm) and ethanol as a liquid medium. The milling was carried out in a planetary mill *Fritsch Pulverisette 6* for 6h (200 rpm).

In planetary ball milling, there is a high-energy impact of grinding balls associated with friction to reduce the size of the powder. The grinding bowl, with the material to be ground and grinding balls, rotates around its axis on the main disk that rotates rapidly in the opposite direction (see figure 2.2.).
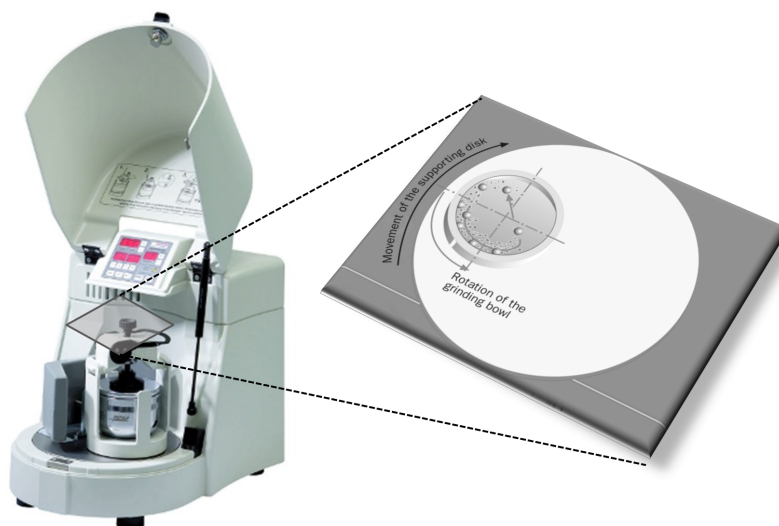
Figure 2.2. Fritsch Pulverisette 6 Planetary ball milling.

The mixture was dried at 80 ℃ for 6 h, and then 120 ℃ for 18 h. The dried powders were ground using a pestle and mortar, placed in an alumina crucible, and then calcined at 900 ℃ for 2 h, using a heating of 10 ℃/min, in a conventional furnace (*Thermolab* company). Later, the calcined powder was again ball milled for 12 h, using the same conditions of the first milling, ground in mortar and dried. These powders are designated as BM12h (Ball Milled for 12h).

One way to obtain ultra-fine powders, thinner than those obtained by ball milling, can be through attrition milling as previously reported [6]. Here, the

grinding is carried out through the friction between the balls and the material to be ground. Agitation inside the jar is achieved by rotating multiple horizontal arms around a vertical shaft. In this work, the calcined powder was ground, in a planetary mill, for 12h (ethanol, 200 rpm). After the conventional ball milling, the powder was dried and placed in another Teflon jar with zirconia balls (2 mm), and attrition milled for 8h and 16h, using ethanol as a liquid medium. The used speed was 700 rpm. These powders will be named as AM8h and AM16h, respectively. Below, it is illustrated the apparatus of an attrition milling.
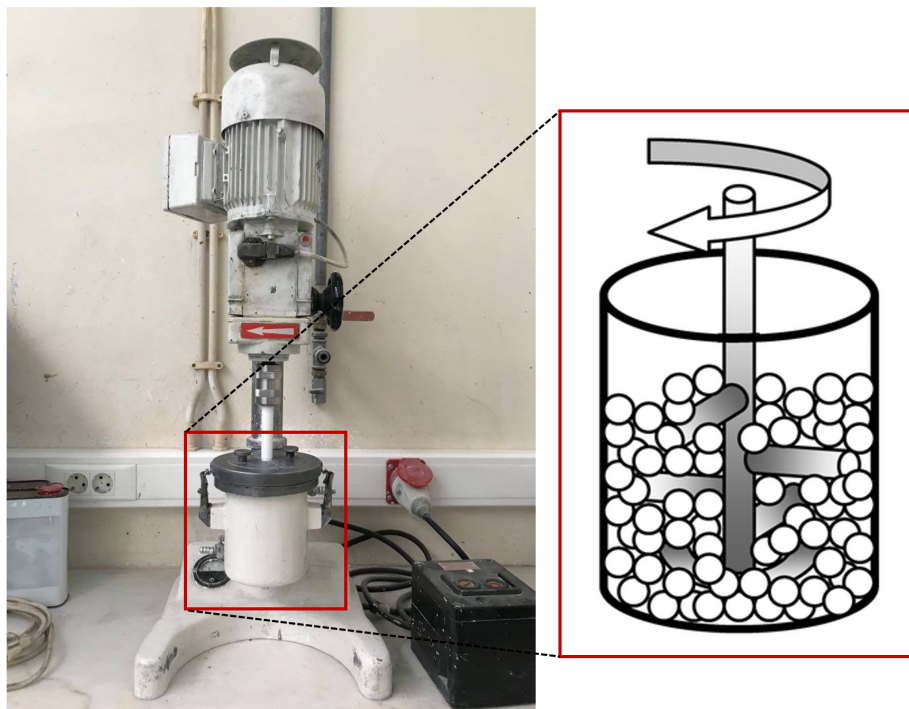
Figure 2.3. Attrition milling apparatus.

2.2. Sintering process

2.2.1. Conventional Sintering

A small amount of fully dried powder was weighed and uniaxially pressed under 125 MPa for 1 min. in a steel mold (ϕ=1cm). The as-pressed pellet was placed in a rubber sleeve, isolated in a vacuum and cold isostatic pressed at 250 MPa for 15 min (Autoclave Engineers *IP32330*). The cold isostatic pressing ensures that the part is evenly compacted before going to sintering. The green compact

was placed at the top of a platinum foil. The sintering was carried out at 1120 ℃ for 3 h, with a heating of 10 ℃/min. in a horizontal tubular furnace.

2.2.2.   Cold sintering process

Some exploratory experiments were carried out at the temperature range of 120 to 250 ℃, using water (5-10 wt.%) as the liquid solvent and a pressure of 250-500 MPa. The conditions that allowed the highest densification were found with 5 wt% of water, a temperature of 150 ℃ for 1h and a pressure of 500 MPa. Nevertheless, such conditions resulted only in samples with a low density (<80%) and a poor mechanical resistance. This means that the samples often proved to be mechanically inadequate to be handled by hand (i.e. they easily broke into pieces), and therefore were inappropriate for the end-purpose of electrical applications. In this sense, a different path was followed in the present work. A mixture of potassium and sodium hydroxides (NaOH:KOH) in a 50:50 M ratio was selected as a "solvent" for the present cold sintering work. It is already reported in the literature the use of this hydroxide mixture for some systems that includes $BaTiO_3$, KNN and ZnO [10,11,47,63]. Hydroxide flux in a eutectic 51:49 mol% composition has a low melting point of 170 ℃ and is referred to in the literature as "NaK" mixture [63], which will be the designation adopted from now on. The low melting temperature and the presence of Na and K elements in its composition, belonging to the same family of elements as KNN, was envisaged as a potential good solvent for this system.

An amount of 0.5 g of powder was weighed and placed in the mortar. Then, 5 wt.% of mixed hydroxides was added to the powder and mixed using mortar and pestle to homogenize the distribution of the powder. The mixture was immediately placed in the steel mold (ϕ=1cm), pressed at 500 MPa, and heated to 250 ℃, with a heating rate of 20 ℃/min. The dwell temperature was maintained for 2h. The experimental setup is shown in the following figure. The steel mold is covered by a metallic layer (band heater), which provides heat for the mold. The temperature control is done with a thermocouple inserted between the mold and the band heater which is connected to a temperature programmer (Eurotherm-P108).
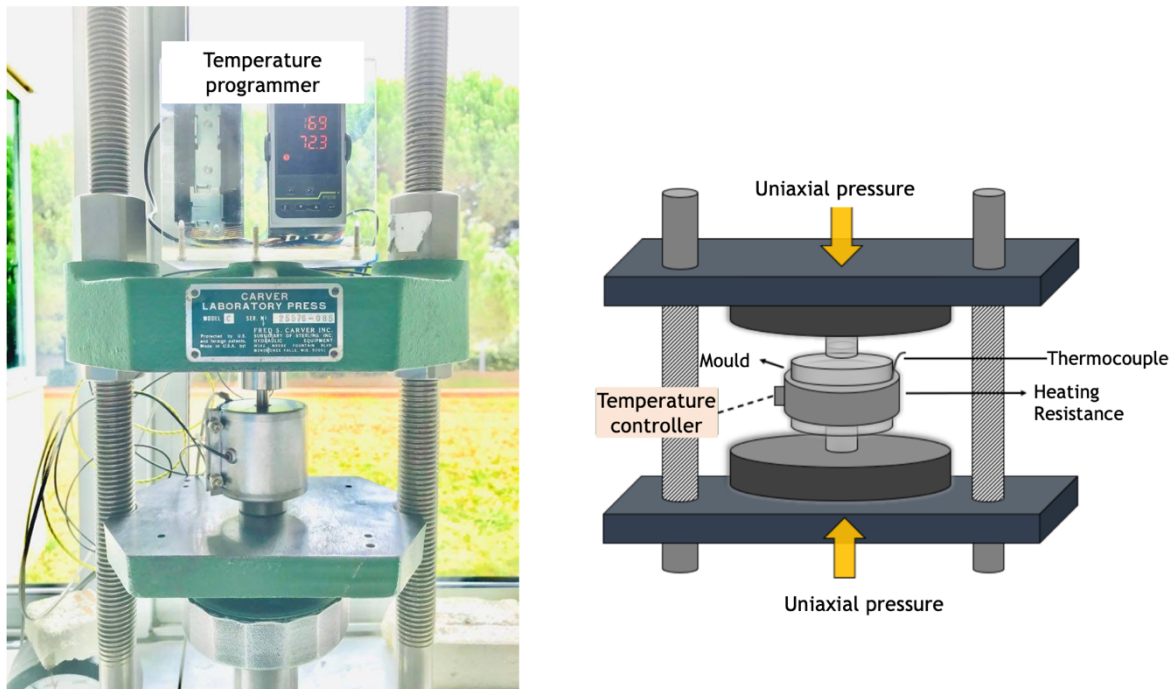
Figure 2.4. Experimental setup for cold sintering process.

2.3. Characterization techniques

2.3.1. Crystallographic and chemical analysis

2.3.1.1. X-Ray Diffraction (XRD)

The study of crystalline phases of the powders and sintered samples was done using the X-Ray diffraction method. The measurements were obtained using the *PanAlytical X´Pert Pro 3* equipment, Cu K-α radiation (λ= 1.5406 Å), scan step time of 58 s, and 0.013° step in the range between 20 and 60°. Phase identification was done by comparison between the obtained diffractogram and the JCPDS standard file 01-085-7128 ($K_{0.5}Na_{0.5}NbO_3$).

X-ray is a form of electromagnetic radiation, highly energetic, with a wavelength in the order of interatomic spacing. When the X-rays reach the solid, a portion is scattered by the electrons associated with each atom or ion that crosses the path of the beam. The condition for diffraction (constructive interference) follows Bragg's law [53].

$$n\lambda = 2d_{hkl} \sin\theta \qquad (2.2)$$

Wherein n denotes the order of reflection, λ the wavelength of the incident radiation, d_{hkl} the interplanar distance of the atoms, and θ the incident angle.

When the law is not complied with, the interference will naturally be non-constructive, that cause low intensity diffracted beams.

The average crystallite size, D, of the produced powders was estimated from the full width at half maximum (FWHM) method of the diffraction peaks, using the Scherrer equation (2.3) [64]:

$$D = \frac{0.81\lambda}{\beta cos\theta} \qquad (2.3)$$

Where λ is the X-ray wavelength (1.5406 $\mathring{A}$), β the corrected line broadening ($\beta = \beta_{exp} - \beta_{inst}$, that is, the difference value between the integral experimental line broadening (in rad) and the integral instrumental line broadening (in rad)), and θ the incident angle.

2.3.1.2. Inductively Coupled Plasma Spectroscopy

The inductively coupled plasma mass spectroscopy (ICP-MS) is an analytical technique used to detect chemical elements present in a sample. Typically, samples are diluted or digested before being placed in the assay system. Once liquid, the sample is nebulized and then ionized by argon plasma. The mass analyzer separates the ions according to the mass-to-charge ratio, obtaining information about the mass and isotopy of the elements [65].

The powder analysis was conducted in the "*Laboratório Central de Análises*", at the University of Aveiro. The procedure adopted was an acid digestion with a solution of HNO_3 and HCl, and a treatment with microwave radiation up to ~190 ºC.

2.3.2. Morphological, microstructural and physical analysis

2.3.2.1. Laser diffraction

For the analysis of particle size and particle size distribution, the laser diffraction (Coulter LS-230) was employed. A small amount of powder was suspended in a deionized water and subjected to an ultrasound bath for 5 min. Then, a small portion was poured into the particle size distribution analysis equipment. The laser method takes advantage of the fact that particles of different sizes have different intensities of scattered light and deduces the distribution of particle size.

2.3.2.2.   Gas adsorption (BET adsorption isotherm)

Specific Surface Area (SSA) was determined by gas adsorption using the BET adsorption isotherm. BET isotherm equation, abbreviated from the author´s initials Brunauer, Emmett and Teller, describes a physical adsorption of a gas on the surface of a porous material. The amount of adsorbed gas depends on the relative vapor pressure and can be quantified by various adsorption isotherms models [66]. The BET model, often used to calculate the surface area, is expressed by the following equation:

$$\frac{P/P_0}{V(1-P/P_0)} = \frac{1}{V_m C_{BET}} + \frac{(C_{BET}-1)P/P_0}{V_m C_{BET}} \qquad (2.4)$$

Where P/P_0 is the relative pressure, V_m the volume of the formed monolayer, C_{BET} a BET constant, and V the volume of adsorbed molecules. The surface area is determined using the following equation (2.5) [67].

$$SSA = \frac{V_m N_A a_m}{v_m m_s} \qquad (2.5)$$

Where N_A is the Avogadro´s number (6.022×10^{23} mol^{-1}), a_m the cross-section area of one adsorbed molecule, v_m the molar volume of one adsorbed molecule (22.4 L of volume occupied by 1 mol of adsorbate gas at standard condition), and m_s the mass of substrate/ adsorbent [67].

The sample is placed in a sample tube and degassed with the aid of an inert purging gas flow, N_2, at 120 ℃, overnight, in the Micromeritics: FlowPrep 060 equipment. The degassed sample is then subjected to the adsorption process at low temperatures, at 77 K, with nitrogen. At this temperature, the surface will adsorb at least one monolayer of the inert species [67]. The used equipment was Micromeritics: Gemini V-2380.

Through SSA and theoretical density (ρ_t=4.51 g/cm^3) of KNN, it was possible to calculate the equivalent particle diameter, D_{BET}, as shown in the equation 2.6.

$$D_{BET} = \frac{SF}{SSA \times \rho_t}$$ (2.6)

Where SF stands for shape factor (7.4 for cubes) [68].

2.3.2.3. Scanning Electron Microscopy (SEM)

The SEM technique uses an electron beam that hit on the sample surface and based on the backscattered (or reflected) electrons, the device collects the electronic signals and converts them into an image. Magnifications between 10 and 50,000 times are possible, with great depths of field. The surface must be electrically conductive to avoid the charging effect and allowing the electrons to move without accumulation [67].

For SEM analysis purposes, a small amount of powder was previously ground with a pestle in a mortar to break the agglomerates. The powder was dispersed on top of the conductive carbon tape and covered with carbon film in a Emitech K950X equipment. In this equipment, two graphite rods are brought into contact with each other, in a vacuum system. A potential difference is applied in such a way that the vaporization of the graphite is induced, and the carbon is deposited onto the surface of the target material. In the case of sintered samples, the analysis was conducted on fractured surfaces.

In addition to obtaining SEM micrographs, point elemental EDS analysis were performed on ceramics produced with AM8h and AM16h powders. The collection of EDS data was carried out on the SEM — Hitachi SU-70 (15 kV) coupled with EDS — Bruker QUANTAX 400 equipment.

2.3.2.4. Transmission Electron Microscopy (TEM)

The TEM image is formed by passing an accelerated electron beam through the specimen. The region to be observed must be as thin as possible (below hundreds of nm) to allow the electrons to pass through the material. Contrasts in the image are produced by beam scattering or diffraction and absorption caused by different behaviors of the elements of the microstructure or defect [53]. In this work, TEM was performed for the produced powders. For the TEM analyses,

solutions with small amounts of powder dispersed in ethanol were prepared. Each suspension was taken to the ultrasonic bath for 5 min. Sampling was done with a copper grid and taken for analysis in the JEOL 2200 FS TEM equipment.

2.3.3. Dilatometric measurements

Dilatometry is a thermoanalytical technique that measures the expansion and/or shrinkage of solid materials under a given thermal cycle. It is a very useful technique because it can give information about glass transition temperatures, shrinkage steps, phase transitions, and even determine sintering temperatures. In the present work, dilatometry was used to follow the shrinkage stages and assess the temperatures for full densification of the different powders in a conventional process.

The powders were uniaxially pressed at 125 MPa for 1 min. and cold isostatically pressed at 250 °C for 15 min. Parallelepiped samples with a length l of ~15 mm were obtained. The thermal cycle used was 10 °C/min up to 1130 °C, performed in the BAHR-Dil 801L equipment. The values were recorded as the length variation at temperature T ($\Delta l = l_T - l_0$) in relation to the initial length, l_0.

2.3.4. Density determination

For the conventional sintered samples, the Archimedes method was performed. The determination of density by hydrostatic weighing (ρ_A, see eq. 2.7) is one of the most well-known methods in materials science. First, the dried samples for 24h were weighed (W_{air}). Then, the disks were placed in a boiling water for 30 min, followed by resting in cold water for 4 hours. The samples were taken out, cleaned with a wet paper and weighed wet (W_{wet}), then immersed in water, (W_{liq}), using an Archimedes apparatus (ρ_{H_2O}=1.00 g/cm^3).

$$\rho_A = \frac{W_{air}}{W_{wet} - W_{liq}} \times \rho_{H_2O} \qquad (2.7)$$

The density of the cold sintered samples was determined by the traditional geometric density (ρ_G) calculation, as follows in equation (2.8).

$$\rho_G = \frac{4m}{\pi d^2 L} \qquad (2.8)$$

Where m expresses the mass (g), d the diameter (cm), and L the sample´s thickness (cm). Here, geometric density was selected rather than the Archimedes

method to avoid any potential reaction of very porous samples with the aqueous medium (e.g. sample disintegration). In this work, the density of the samples will always be expressed in relation to the theoretical value (ρ_t=4.51 g/cm^3).

2.3.5. Compressive Strength

Characterization of the mechanical properties of KNN ceramics after CSP has not been reported in the literature yet. In this work, a mechanical characterization method based on the mechanical compressive strength was adopted. Disk-shaped specimens were polished on the sides until they reached a rectangular shape (figure 2.5), with a length-to-width (l/w) ratio of approximately 1.5 and a constant thickness (1.2-1.3 mm). The compressive test was performed at room temperature in SHIMADZU: AG-A R3 equipment, using a constant loading speed of 0.5 mm/min and a load cell of 20 kN. The maximum applied force (observed as a single-peak in the force-displacement graph) was recorded and used to calculate the compressive strength.
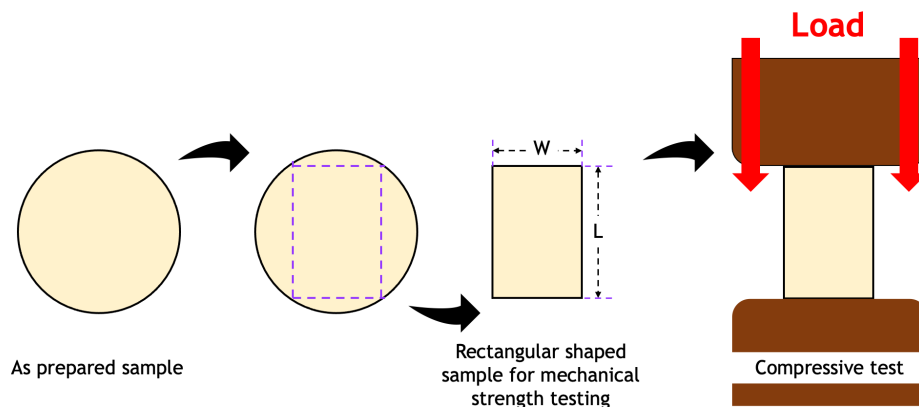
Figure 2.5. Disc-shaped samples converted into a test piece, and then compressive loaded.

2.3.6. Electrical characterizations

2.3.6.1. Dielectric measurements

Dielectric measurements are important in the characterization of a ceramic material. The relative permittivity (or dielectric constant), ε_r, can be defined as the ability of material in a given volume to store electrical energy, in the form of polarization, under the effect of an electric field. This constant is the result from the ratio between the permittivity of the medium and the permittivity of the

vacuum, ε_0 (8.85×10^{-12} F/m) [53]. In a practical situation, the current flowing through a circuit is alternated (AC). Ideally, a dielectric should have zero energy dissipation, that is, no energy losses due to the Joule effect. However, as the resistance values are not infinite, some current will always pass through the dielectric, resulting in dielectric losses. These losses can be numerically represented by loss tangent (tanδ). For dielectric measurements, silver suspension (Agar Scientific AGG302) was painted on the planar surfaces of the disks, dried at 50 ℃ for 5 min, and subsequently fired at 500 ℃ for 30 min to be used as electrodes.

Dielectric constant and losses were measured using a Hewlett Packard (HP) Precision LCR meter (4284A). The values were recorded between room temperature and 500 ℃, at frequencies between ranging from 100 Hz and 1 MHz.

2.3.6.2. Piezoelectric measurement — Berlincourt method

Piezoelectric materials, by nature, are characterized by having randomly aligned domain orientations. The randomly orientated domains result in a macroscopic net polarization of zero that directly impacts the piezoelectric response. In this context, it is important to be able to align all or almost all the domains in the same direction (poling) in order to be possible to observe a piezoelectric response [69]. In this work, the polarization of the samples was performed by corona discharge, using an electric field of ~5 kV/mm at 80 ℃ for 30 min, maintaining the voltage during cooling to room temperature. Corona Poling is a non-contact method that employs a high electric field extending from a sharp tip electrode and a grounded plate on which the sample is placed and heated [70].

The piezoelectric coefficient, d_{33}, quantifies the polarization resulting from the application of a mechanical stress; d_{33} was measured using the Berlincourt method. The sample is placed in the middle of two probes and clamped by lowering the upper probe. Then, the value of d_{33} is displayed on the screen. The used equipment was a Sinocera YE2730A Berlincourt meter, with a clamping force of 250×10^{-3} N. In figure 2.6. it is schematized this step of the procedure.
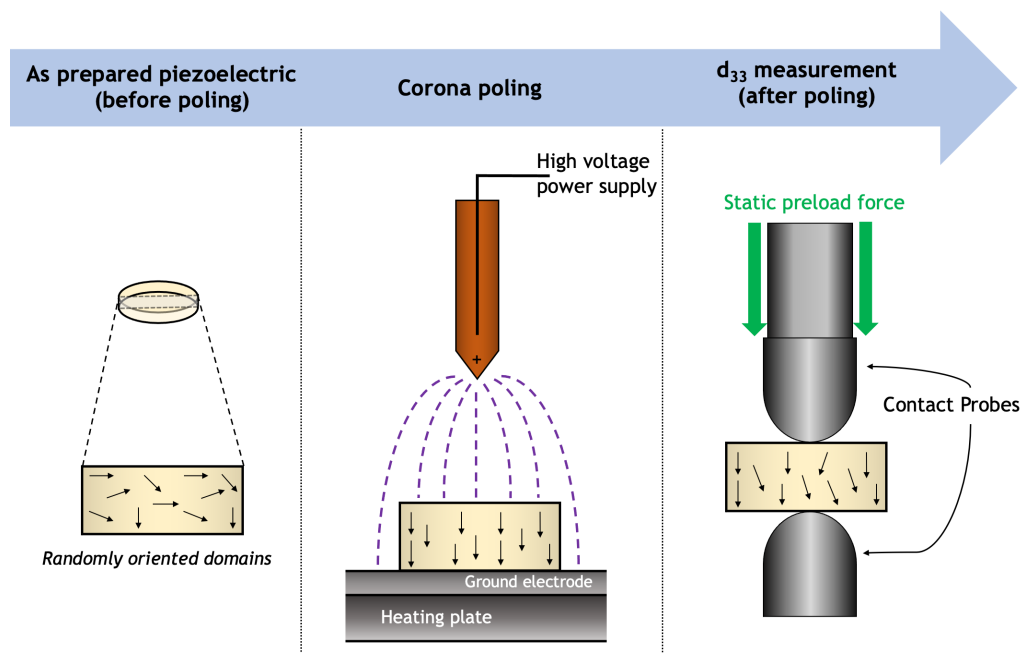
Figure 2.6. Sample preparation for measuring the piezoelectric coefficient, d_{33}.

2.3.6.3. Ferroelectric measurements (P-E loops)

Ferroelectric materials present spontaneous polarization that can be reversed to the opposite polarization direction by an electric field. When a strong electric field is applied, there is a full alignment of ferroelectric domains — saturation polarization, P_s. When the field is removed, most of the electric dipoles stay in alignment, exhibiting a remnant polarization, P_r. The remaining polarization is eliminated through the application of a coercive field, E_c. The ferroelectric behavior can be studied by plotting Polarization-Electrical Field (P-E) hysteresis curves [71]. An example of a hysteresis loop is shown below (figure 2.7).
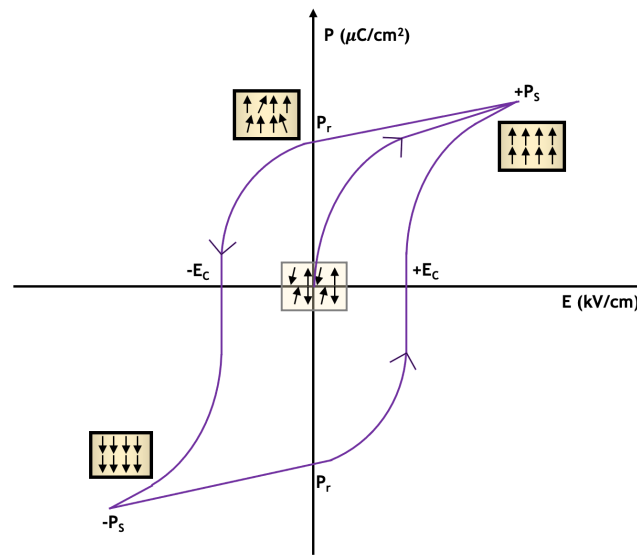
Figure 2.7. Example of hysteresis loop of ferroelectric materials. Adapted from [71].

The samples were sanded to a thickness <1mm and coated with electrodes. Two types of electrodes were tested, silver and gold. The ferroelectric measurements were carried out at the room temperature with the sample inside of a silicone bath. P-E loops were recorded using the AIXACCT-TF analyzer 2000 equipment, and a Trek 609E-6 equipment as a high voltage amplifier.

2.3.6.4. Piezoelectric force microscopy (PFM)

Piezoelectric behavior at the nanoscopic level was assessed using atomic force microscopy (AFM) in the piezoresponse mode. In AFM, a very sharp probe interacts directly with the surface, scanning the attractive and repulsive forces between the probe and sample surface to image high-resolution topography of the sample at a nanometre scale. Piezoelectric force microscopy (PFM) uses standard AFM configuration in contact mode with additional alternating voltage (V) applied to the tip. The voltage induces shape deformations of the sample and causes periodic vibrations through its surface, transmitted to the tip. These results are read out resorting to a lock-in amplifier system [72,73].

The AFM and PFM measurements were done using manufacture AFM microscope (NTMDT NTEGRA Prima). For the piezoresponse mode, the external lock-in system (SR830 Standfort Research) and function generator (FG120

Yokogawa) were used. The piezoresponse signal was measured at frequency of 50 kHz and amplitude of 10 V. The AFM/PFM measurements were acquired by utilizing the Multi75-G AFM probe (Budgetsensors) possessing resonance frequency at 75 kHz and stifness of 3 N/m.

3. Results and discussion

In this chapter, the results obtained during the present study are presented and discussed. The sequence of results will firstly address the characterization of KNN powders, followed by the crystallographic, microstructural, mechanical and electrical characterizations of both the cold and conventional sintered samples.

3.1. Powders Characterization

Before starting the discussion, it is important to remember the label attributed to each powder (see table 3.1.).

Table 3.1. Produced powders and respective designations.

Abbreviation	Milling Process
BM12h	Ball-milling (12hours)
AM8h	Ball-milling (12hours) + Attrition milling (8hours)
AM16h	Ball-milling (12hours) + Attrition milling (16hours)

Figure 3.1. shows the XRD patterns of the different powders. By comparing them with the JCPDS database card (01-085-7128), it can be seen that the main peaks of all powders coincide with those of KNN perovskite, in its orthorhombic phase, at room temperature. BM12h powder is characterized by extremely sharp diffraction peaks which indicate a well-crystallized powder. Subsequent 8h attrition milling renders the powder less crystaline, that is, the initial narrow, sharp and well-splitted main peaks are convoluted to broader and more diffuse peaks. This behavior can be related to a higher quantity of randomly oriented smaller crystallites in a given diffraction space, which results in less intense constructive interferences. With a further increase in the attrition milling time (AM16h), a less significant change was observed in the peaks width when

compared to that of AM8h (crystallite size D: AM16h~20 nm < AM8h~30 nm < BM12~85 nm).
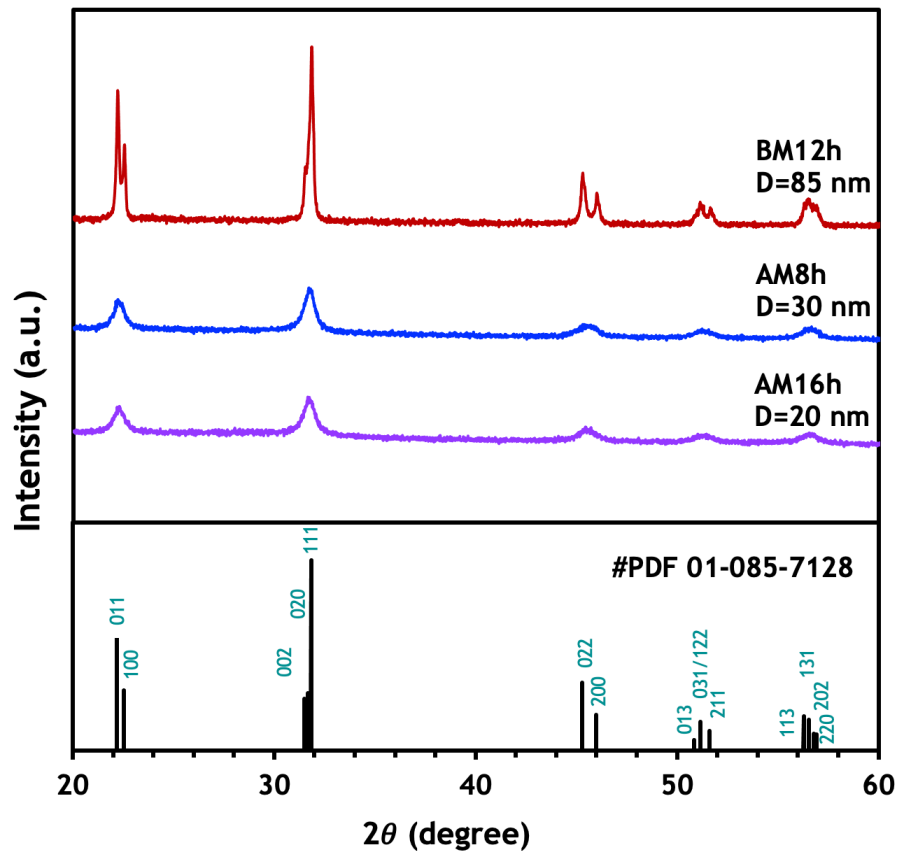
Figure 3.1. X-Ray diffraction pattern of the produced KNN powders and respective crystallite size (D).

The powders were characterized by ICP-MS and the obtained results were converted to K/Na and (K+Na)/Nb molar ratios and presented in table 3.2. The K/Na ratio for BM12h powder is 0.97, which can be considered very close to 1. The obtained value may reflect both the 2wt.% excess addition of Na and K elements, during the synthesis step (before the first milling), and also any possible powder loss between milling and drying. This stoichiometry was changed to 0.93 and 0.96 with later attrition milling for 8h and 16h, respectively.

The "initial drop" of the K/Na ratio, associated with the addition of an 8h attrition milling step, could be explained by a higher leaching rate of potassium as compared to sodium. In this case, the result would be consistent with that reported by Ozmen et al. [62] for the chemical stability of KNN in aqueous media. However, the K/Na ratio obtained from the 16h attrition milling indicates that

such ionic leaching process may change with the milling time, as the K/Na rises to 0.96. Additionally, no data about the chemical reactivity between ethanol and KNN are found in the literature, making it difficult to interpret further these results. (K+Na)/Nb ratio is higher than 1, indicating that the initially added excess alkali supplemented any potential volatilization of the A-site ions. Nevertheless, these values may be looked at as indicative of a stoichiometry condition close to that corresponding to $K_{0.5}Na_{0.5}NbO_3$.

Table 3.2. Potassium, sodium and niobium stoichiometry data of the produced powders based on ICP-MS results.

Powders	Ratio K/Na	Ratio (K+Na)/Nb
BM12h	0.97	1.06
AM8h	0.93	1.05
AM16h	0.96	1.07

Figure 3.2.(a, d, g) presents some scanning electron micrographs of BM12h powder particles. As observed the particles present a predominantly cubic shape, generally known as a KNN fingerprint. Particle size of BM12h powders is not uniform as large cubes with a micrometric edge size coexist with smaller and irregular shaped particles.

In the case of AM8h and AM16h powders (figures 3.2.b and 3.2.c, respectively), both presented much smaller particles, many of which in the nanometric scale, with less defined edges and more rounded shapes. Additionally, STEM (figures 3.2.e and 3.2.f) and TEM images (figures 3.2.h and 3.2.i) also reveal that there is still the presence of some particles in the submicron range, which may be a trace of coarser particles that were not ground during attrition milling. Besides that, this set of results confirms that high energy friction milling is an effective comminution method, capable of fragmenting large cubes into smaller and less regular units. Furthermore, it is worthy mentioning that the obtained AM particles appear to be agglomerated into submicron units (figure 3.2.b and 3.2.c).
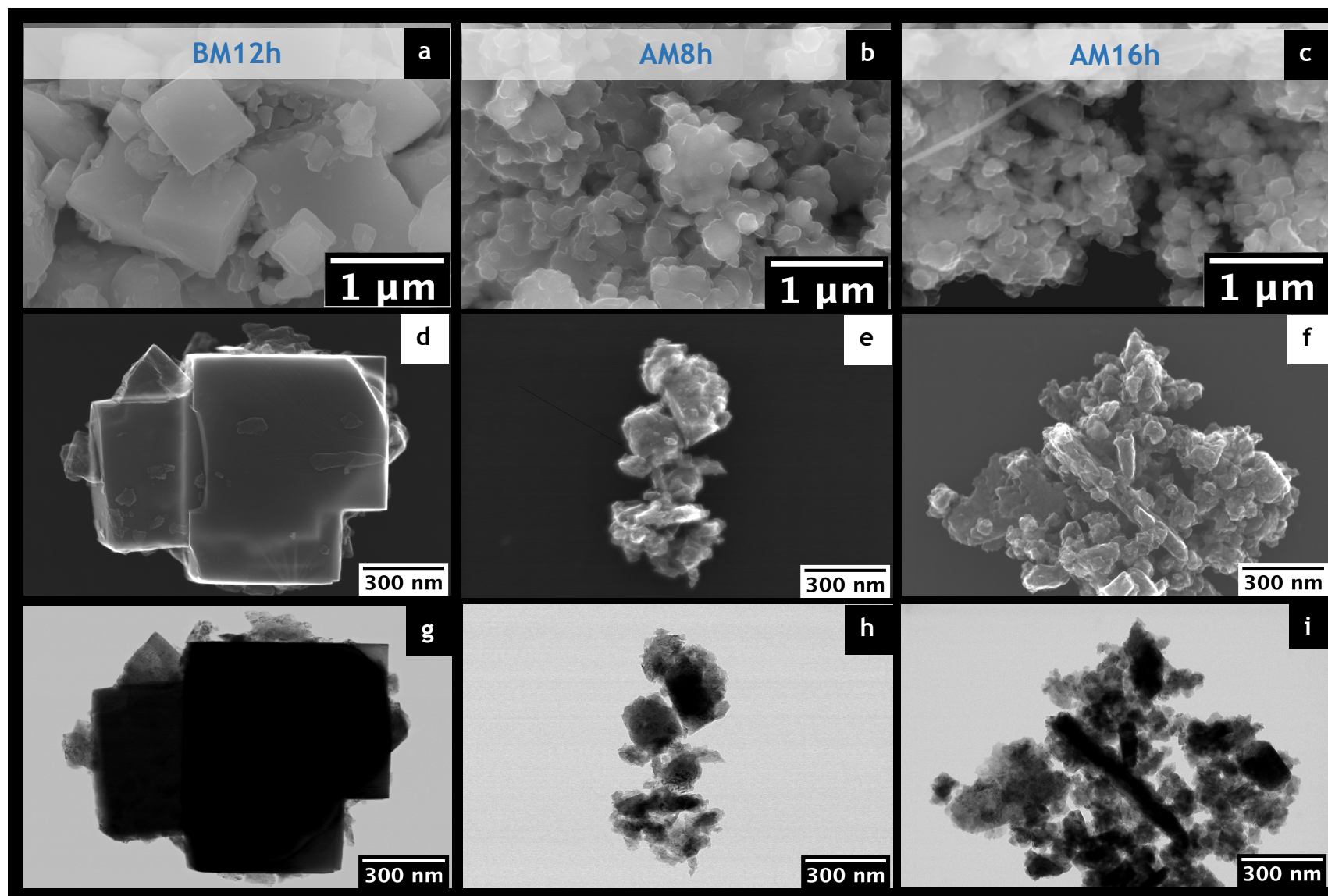
Figure 3.2. Scanning Electron Micrographs (SEM, 15 kV) of the BM12h, AM8h, and AM16h powders (a-c, respectively); Scanning Transmission Electron micrographs (STEM, 200 kV) of BM12h, AM8h, and AM16h powders (d-f, respectively); and Transmission electron micrographs (TEM, 200 kV) of BM12h, AM8h, and AM16h powders (g-i, respectively)

Figure 3.3 shows the particle size distribution results obtained by laser diffraction. The BM12h powder has a bimodal distribution with peaks centered on ~0.2 and 2 μm, which are consistent with the existence of two populations of different sized particles that were observed in SEM images. The presence of a bimodal size distribution in the BM12h powder may be related with the addition of 2 wt.% excess alkali, in line with the results reported by Acker et al. [74]. The authors studied the influence of the stoichiometry of alkaline elements and niobium in the sintering of KNN. They showed that for the calcination at 775 ℃ for 5h, the addition of 2% mol of alkali led to a bimodal particle size distribution with peaks around 0.3 and 3.2 μm in milled powders after calcination. According to the authors, during the calcination step, the alkali excess enabled higher reactivity between the constituents of the powder, at 775 ℃, more homogeneous solid solution, and also led to a grain coarsening. Here, ball milling was not sufficient to break down all the coarser particles, thus leading to bimodal size distribution [74].

Regarding the AM8h and AM16h powders (figure 3.3), it is shown a trimodal distribution, with peaks centered on ~0.1, 0.6 and ~2.5 μm. The peak centered at ~0.1 μm is attributed to the smaller particles with less defined edges that were abundantly detected in the micrographs (SEM and TEM) presented in figure 3.2 (b, e, h) and 3.2. (c, f, i). The remaining peaks centered on larger sizes are here suggested to account for the existence of agglomerates composed of smaller units that were also noticed in Figure 3.2.
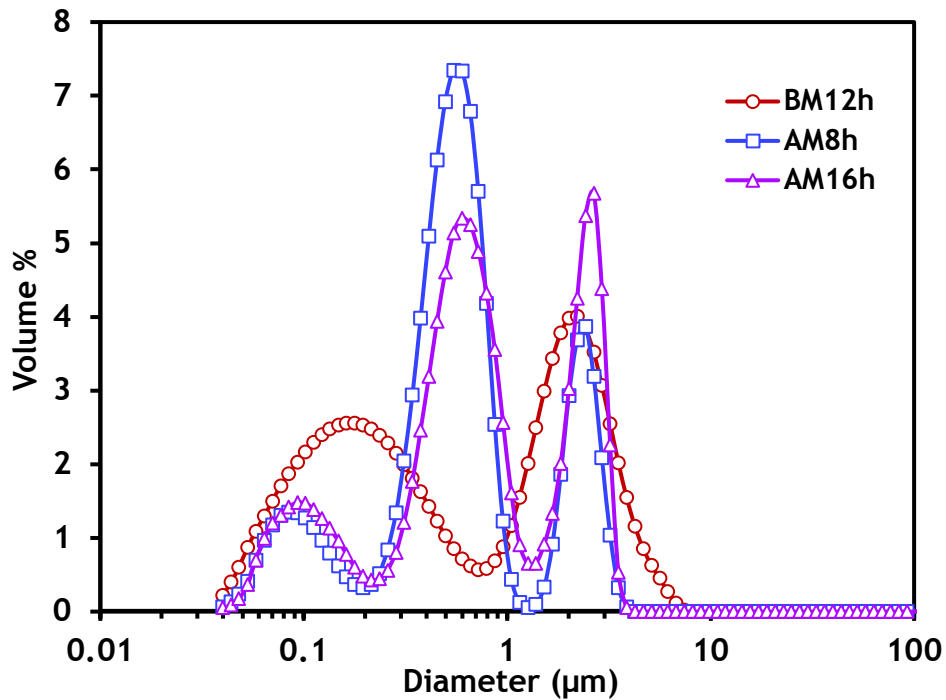
Figure 3.3. Particle size distribution of the produced powders.

It should be noted that during laser diffraction measurements, there is a possibility of agglomeration of fine powders in the used aqueous environment, which may affect the measured particle size distribution as suggested in a previous work [75]. Also, the nature of the agglomerates may influence the measurements by laser diffraction. The smaller the primary particles are, the harder the nature of the agglomerates tends to be, that is, the agglomerates will not easily be destroyed by ultrasonic stirring [5,76]. Therefore, the curves obtained by laser diffraction measurements of AM powders not only reflect the size of the fine particles, and possibly some remaining coarser particles that were not crushed during milling but also the size of existing agglomerates.

Table 3.3. summarizes the morphological attributes of KNN particles (specific surface area, SSA, and equivalent particle diameter, D_{BET}) based on the results from laser diffraction and gas adsorption (BET adsorption isotherm). From laser results, there is a decrease in the mean size when going from BM12h to AM8h, and an increase when going AM8h to AM16h powder, which seems a little bit contradictory. On the other hand, in the specific surface area, the results reveal a clear increase for longer millings. The specific areas of attrition milled powders are ~5.2 and 5.7 times larger (AM8h and AM16h, respectively) than that of BM12h

powder. The D_{BET} values obtained from equation 3.1. are presented in table 3.3. They indicate particles with submicrometric (441 nm) and nanometric (86 and 78 nm for AM8h and AM16h, respectively) mean sizes, which are in line with the results observed in TEM micrographs.

Table 3.3. Powder morphological attributes: mean size from laser diffraction; specific surface area, SSA, and equivalent particle diameter, D_{BET}, derived from gas adsorption results (BET isotherm).

Powder	Particle morphological attributes		
	Mean size (μm)	SSA (m^2/g)	D_{BET} (nm)
BM12h	1.283	3.7	441
AM8h	0.903	19.1	86
AM16h	1.141	21.2	78

The temperature dependence of the shrinkage curves of the three compositions during heating are shown in figure 3.4. For BM12h, the fine constituents of the powder start densifying at a low temperature as suggested by the first abrupt shrinkage, occurring between 600-800 ℃ [74]. With a further increase in temperature above 1000 ℃, there is a significant increase in the shrinkage rate. Shrinkage continues to occur up to the test maximum temperature (~1137 ℃) without reaching a plateau, indicating that densification is still in progress. The onset temperature of densification for the AM8h sample is ~760 ℃, which is higher than that of BM12h composition. However, AM8h ends its densification below 1088 ℃, with a shrinkage of 11.3 %. Regarding AM16h, its maximum shrinkage (11.5%) is achieved at even lower temperatures (~935 ℃), showing that the successive milling of the powders, which promoted an effective reduction of particle size, did contribute to the reduction of the temperature where the final stages of densification take place.
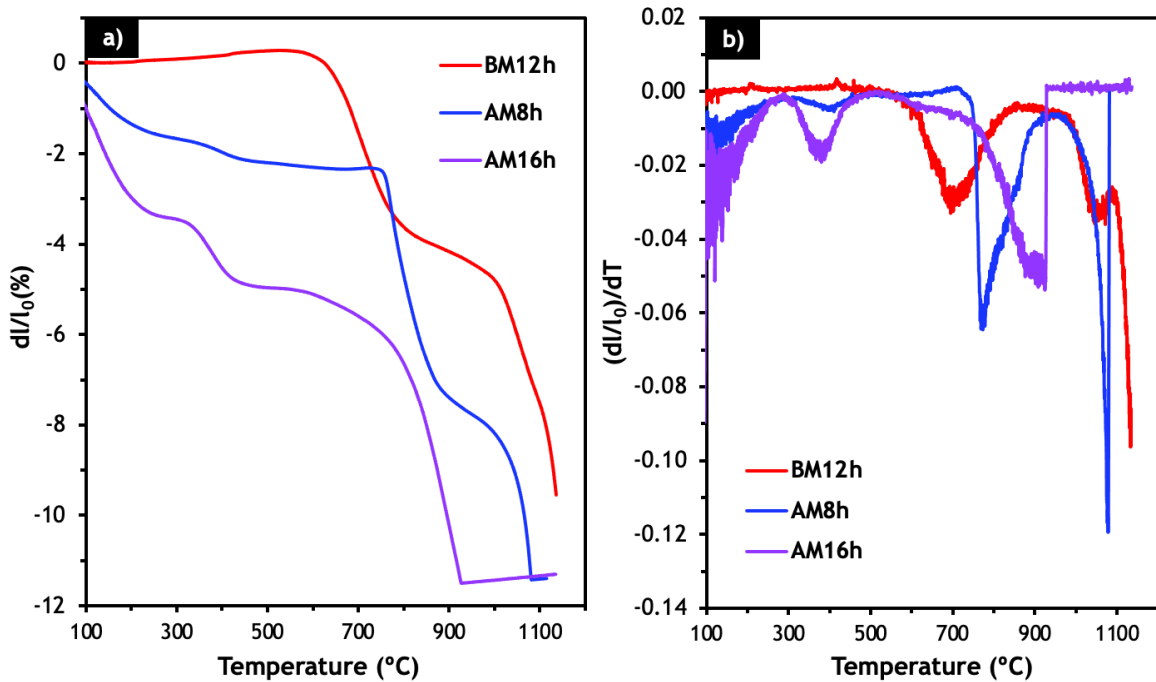
Figure 3.4. Dilatometric curves ((a) shrinkage and (b) shrinkage rate) obtained when conventionally heating the KNN compacts produced with the different powders (BM12h, AM8h and AM16h).

An important outcome that should be highlighted here, is that all these powders, exhibiting distinct morphologies, also behave differently during a conventional sintering cycle. The AM16h powder is the one that densifies at a lower temperature range, being this observation in good agreement with what is reported in the literature, i.e. smaller sized particles having larger surface energy do benefit from a larger driving force for sintering [6,7].

3.2. Characterization of the conventional and cold sintered ceramics

In this section, the sintered samples under analysis will be labeled as presented in table 3.4.

Table 3.4. Labelling of the conventional (CS) and cold (CSP) sintered ceramics.

Ceramic label	Powder	Thermal cycle (temperature and time)	Pressure	Solvent
CS1120	BM12h	CS 1120 °C (3h)	–	–
CSP_H_2O	BM12h	CSP 150 °C (1h)	500 MPa	H_2O (5 wt%)
CSP_BM12h	BM12h	CSP 250 °C (2h)		NaOH:KOH (5 wt%)
CSP_AM8h	AM8h			
CSP_AM16h	AM16h			

3.2.1. Structure, microstructure and compressive strength

Figure 3.5. shows the XRD patterns of the produced ceramics (conventionaly sintered (CSed) and cold sintered (CSPed)). It can be seen that both the CSed and the CSPed samples have the main peaks coincident with those corresponding to pure KNN of orthorhombic structure, according to the JCPDS file (01-085-7128). The conventional ceramic CS1120 exhibits extremely sharp and well-defined peaks. In the case of CSP_H_2O samples (Cold Sintering Process using BM12h powder and water as solvent), although the used powder had well-defined XRD peaks, there was a convolution and broadening of the various peaks, as exemplified by the peaks corresponding to the crystallographic planes (011) and (100). Similar observations apply to CSP samples using the hydroxides mixture as the flux. In this case, the sodium and potassium (NaK) hydroxides seem to have introduced an "amorphous" characteristic to the cold sintered ceramic.

Despite having used a flux of hydroxides for CSP ceramics and the possibility that this flux may have precipitated or recrystallized, the presence of second phases is not obvious. This observation may be related to the low flux/parent

powder proportion (only about ~5 wt%.) and/or the inherent low crystallinity of the (NaK) hydroxide flux [47]. This observation is in line with what was reported by Deng et al. [10].
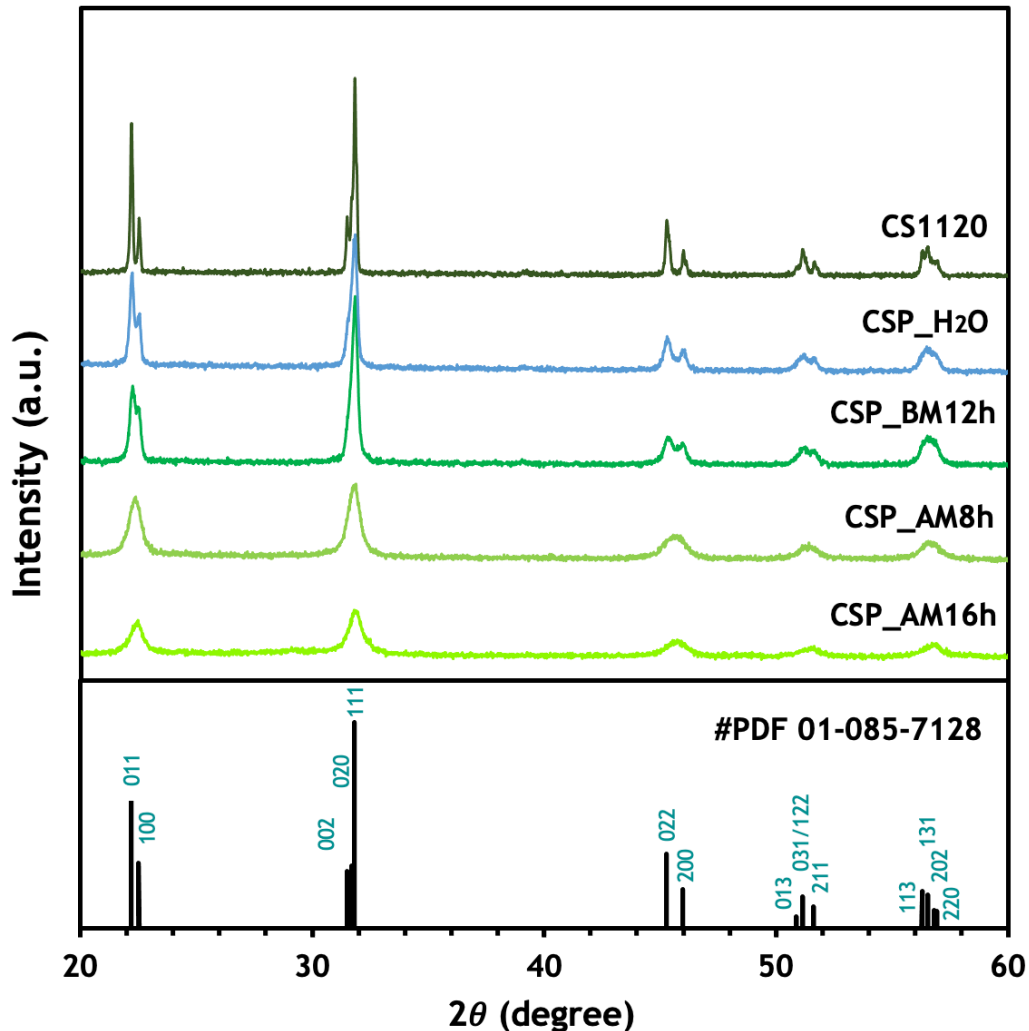
Figure 3.5. X-Ray diffraction patterns of conventionally sintered ceramics at 1120 °C (sample CS1120) and of cold sintered ceramics under the following conditions: (i) Cold sintered sample with H_2O using BM12h powders (5wt%., T=150 °C, t=1h, P=500 MPa)→ sample CSP_H2O; and (ii) cold sintered samples using using NaOH:KOH flux (5wt%, T=250 °C, t=2h, P=500 MPa) and the following powders: BM12h powders →sample CSP_BM12h; AM8h powders→ sample CSP_AM8h; AM16h powders → sample CSP_AM16h .

The influence of the two processing methods (conventional sintering and cold sintering) using different powders on ceramics final density and compressive strength is expressed in the bar graph of figure 3.6. To the best of our knowledge, it is the first time that mechanical properties of CSPed KNN are reported. It is

observed that conventional ceramics have a high relative density of ~94% and exhibit the highest compressive strength of ~90 MPa.
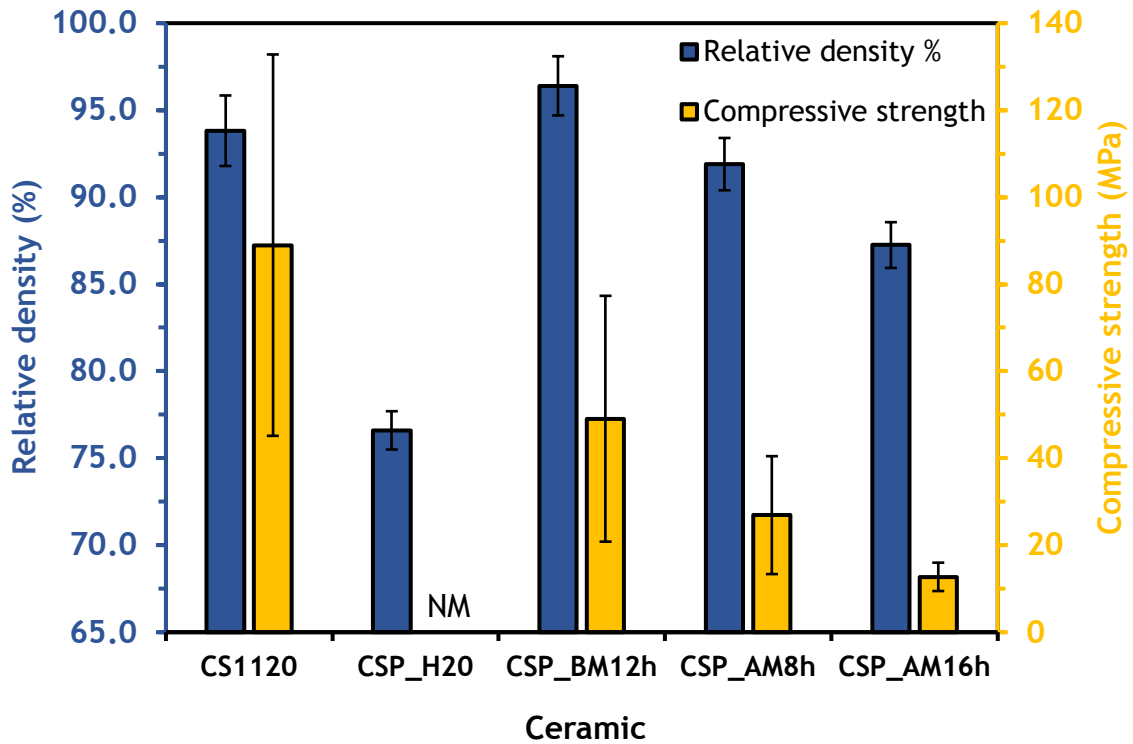
Figure 3.6. Relative density and compressive strength for conventional and cold sintered ceramics. CS1120: Conventional air sintering at 1120 °C; CSP_H$_2$O: Cold sintering using 5 wt% of H$_2$O (T=150 °C, P=500 MPa); NM: Not Measured; CSP_(BM12h, AM8h, AM16h): Cold Sintering Process using BM12h, AM8h and AM16h powders at 250 °C and 5wt% of NaOH:KOH flux (P=500 MPa).

Concerning CSPed ceramics, there is a clear decreasing trend in the relative density as we decrease the particle size of the starting powder: density decreases from ~96% for BM12h powder to ~92% for AM8h powder and reaches 87% for the finest AM16h powder. These density values are higher than that corresponding to the cold sintered sample using only water (ρ_r~76%). These results indicate that, as compared to water, the hydroxide flux was more effective in terms of the ceramic densification during CSP. Regarding the mechanical behavior of the CSPed ceramics, despite the high value of relative density (~96%) achieved when using BM12h powder, the final compressive strength is still modest (50 MPa) as compared to that of CS1120 ceramics (90 MPa). The compressive strength continues to decrease as the final density decreases, i.e. as the starting powder becomes finer.

To attempt establishing a processing-structure-property relationship, the microstructures of the ceramics under analysis were investigated. Scanning electron micrographs of fracture surfaces of the produced ceramics are depicted in figure 3.7.
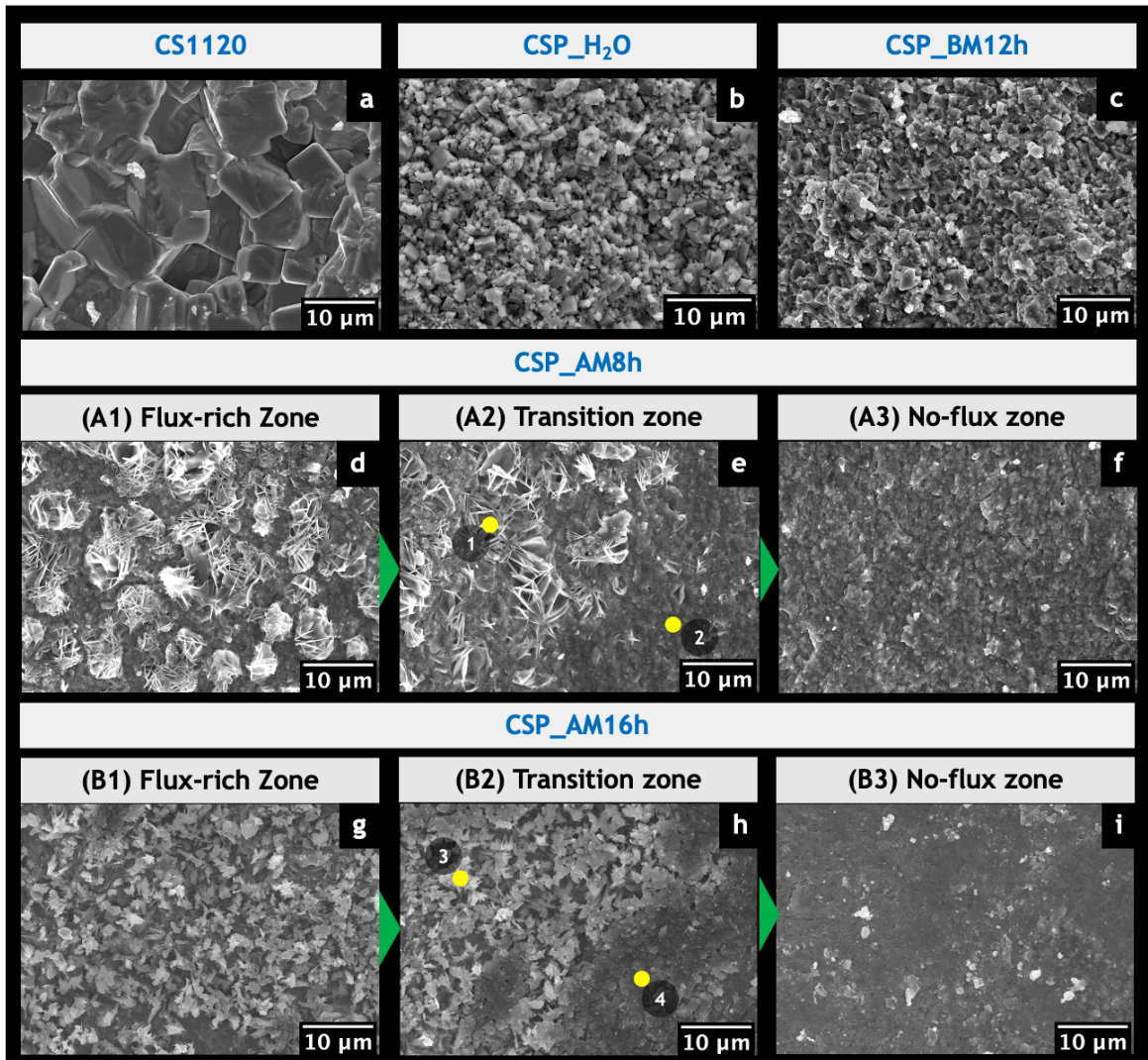
Figure 3.7. SEM micrographies of CS1120 (conventional sintered); CSP_H_2O: cold sintering using water; CSP_BM12h, CSP_AM8h and CSP_AM16 (Cold sintering using NaOH:KOH flux). In CSP_AM ceramics, there are 3 distinct zones: (A1 and B1) the one that reacted directly with the flux, (A2 and B2) the transition, and (A3 and B3) the zone with no Na&K hydroxide. The regions marked with numbers were subjected to chemical elemental quantification (spot) by EDS.

The CS1120 ceramic is characterized by a uniform microstructure composed of coarse cubic-shaped grains and well-defined grain boundaries (figure 3.7.a). The average grain size is around 10 µm, denoting that a noticeable grain growth

occurred during the sintering step. Despite the relatively dense ceramics obtained here, it has been referred that the cubic shape of the grains is one of the main reasons accounting for the poor sinterability of KNN [7]. Note that in this microstructure, no fine grains were detected.

The sample cold sintered with water, CSP_H$_2$O (figure 3.7.b) shows a microstructure composed of much finer grains, also cube-shaped, with a grain size apparently close to that of the starting powder. The microstructure of CSP_BM12h (figure 3.7.c) also shows fine grains but with a less regular shape as compared with the CSP_H$_2$O ceramic (CSP using only water). The grains appear to be less loose than when using only water, and extremely well compacted. Overall, it is clearly demonstrated the effectiveness of CSP to preserve the initial particle size.

Figure 3.8. shows a micrograph of CSP_BM12h obtained under a higher amplification. As observed the grains exhibit less sharp and regular edges as compared to the initial powder particles, suggesting that particle surface dissolution took take place under the used experimental conditions, i.e., the flux, the temperature, and the applied pressure cooperatively assisted the CSP. Also, large grains, with an average size around 2 μm, coexist with smaller grains that seem to have been deposited onto the larger grains' surfaces (blue arrows). It is here suggested that some of these small grains may result from a precipitation phenomenon allowed by the supersaturated flux in the vicinity of the grains. Such dissolution-precipitation mechanism is a typical feature of a cold sintering process [38]. Furthermore, there are a few areas showing sintering necks (yellow dotted circles) which suggest here and there the transport of matter after CSP.
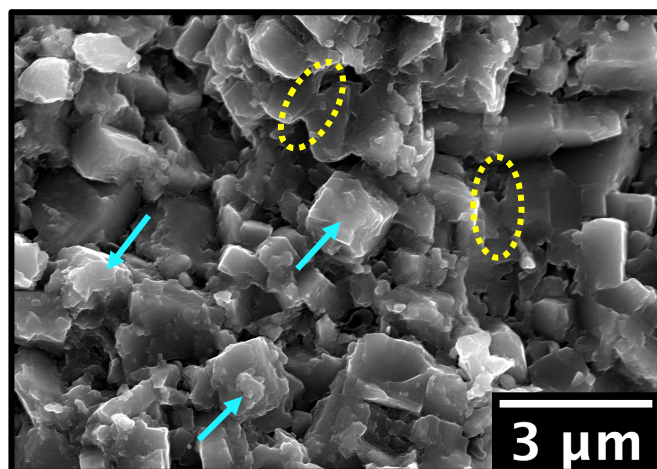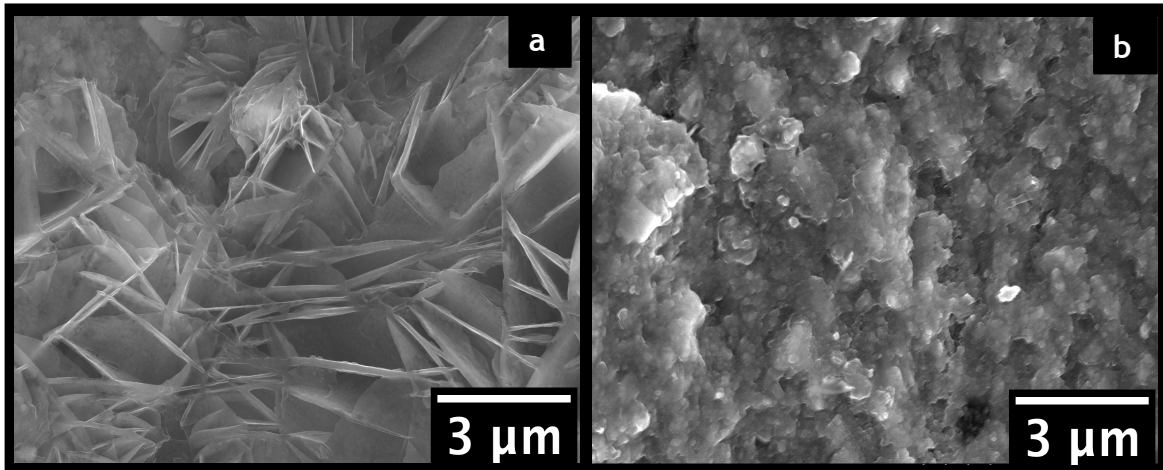

Figure 3.8. Microstructure of CSP_BM12h (fracture).

In the case of the ceramics produced with AM8h starting powder ("CSP_AM8h" in figure 3.7), their microstructure could be characterized by three distinct zones (zones (A1), (A2) and (A3)) as typified by the images (d), (e) and (f) in figure 3.7. In region (A1) there is a layer of flowers-like shaped material that covers the fine KNN grains, possibly resulting from precipitation of hydroxides and/or some chemical interaction of KNN with the locally abundant NaK flux. The local EDS analysis of the flower-like structures (indicated as point 1 in Figure 3.7 and Table 3.5) pointed out a poorer potassium content over sodium,i.e. an (K/Na) atomic ratio of ~0.22. The alkali content (K+Na) is ~3.5 times higher than that of niobium, indicating that the flower-shaped structures resulted from a chemical interaction between KNN and the hydroxide flux. In opposition to region (A1), the region (A3) appears to be dense and made up of fine grains, similar to the starting powder particles; region (A2) configures the transition between regions (A1) and (A3) . As shown in the table 3.5. the denser region of the transition zone (point 2) presents a more balanced stoichiometry of alkalis and niobium as compared to point 1.

Table 3.5. Elemental analysis carried out at different locals of the microstructures shown in figure 3.7 (points numbered 1 to 4) (atomic percentage).

| Point	K	Na	Nb	O	K/Na	(K+Na)/Nb
1 CSP_AM8h	5.3	24	8.4	62.3	0.22	3.49
2 CSP_AM8h	14.4	13.7	18.9	53	1.05	1.49
3 CSP_AM16h	4.9	23.6	7.6	63.9	0.21	3.75
4 CSP_AM16h	10.2	16.8	16.3	56.7	0.61	1.65

Looking closely at the zones (A1) and (A3) of CSP_AM8h (figure 3.9), the flower-like structures enriched in sodium are now seen to correspond to very thin and tangled platelets which development created a local porous region (figure

3.9.a) that contrasts with the very dense zone (A3) (figure 3.9.b). The existence of porous regions similar to zone (A1) may constitute a strong reason for the lower density value of CSP_AM8h as compared to CSP_BM12h.

Figure 3.9. SEM micrographs of a fractured surface of CSP_AM8h showing the amplified view of a a) region enriched in Na, and b) of another region with a more balanced stoichiometry of alkaline elements.

Similar to CSP_AM8h, the microstructure of CSP_AM16h ceramics is also characterized by 3 distinct zones (figure 3.7. (g),(h) and (i)): one flux-rich zone denoting a chemical interaction between KNN and the flux (B1), one "transition zone" (B2) and another zone where the flux presence is less obvious (B3). The flux-rich zone is morphologically different from the flower-like zone observed in CSP_AM8h, displaying a needle-like/lamellar appearance that overlaps one on top of the other. From the microstructure of figure 3.10.a), it appears that the needles-shaped region account for a less porous region than the equivalent region in CSP_AM8h (A1). Despite that, the K/Na ratio obtained from ESD results (point 3 in table 3.5) is close to that corresponding to the "flower-like structures" in CSP_AM8h. Additionally, the (alkali/Nb) ratio is also higher (3.75x) than that corresponding to the region free of "stuck lamellas" (point 4 in table 3.5).
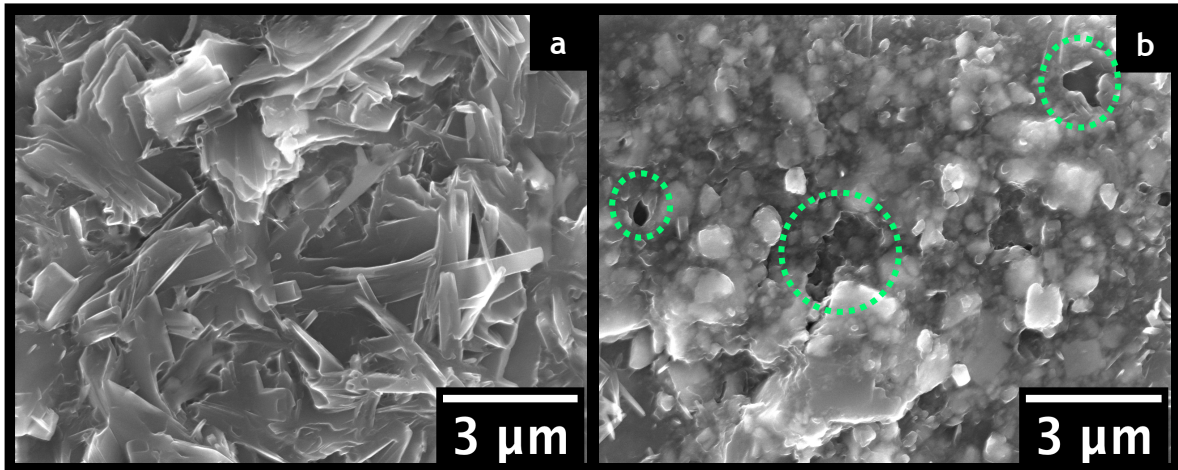
Figure 3.10. SE micrograph of the fractured surface of CSP_AM16h ceramic in the a) "Na-rich zone" and b) region adjacent to the presence of the hydroxide flux.

It was noticed in the figure 3.10.b) some porosity (green circles), thus explaining the lower measured density. In another analysis of the same ceramic (CSP_AM16h), a chemical etching was carried out with hydrofluoric acid (HF) at 40%VV (2 to 3 drops on the surface for 5s) and it was found an interface region of "(KNN grains)-(wires)-(KNN grains)" (figure 3.11), implying that the flux worked as a gluing agent (orange arrows) and did precipitated locally.
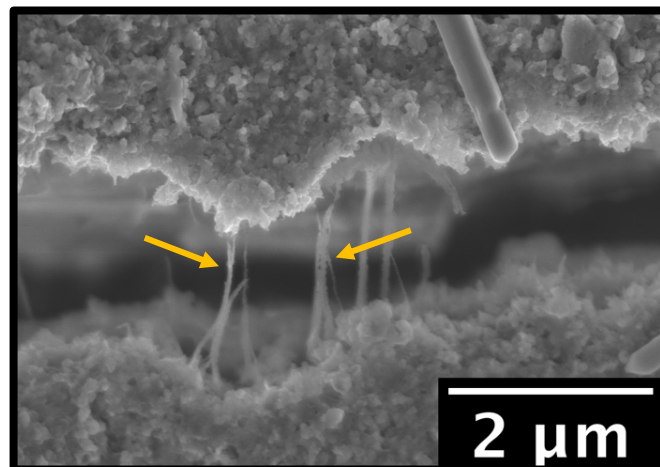
Figure 3.11. SE micrograph of HF-etched CSP_AM16h ceramic in the KNN/flux/KNN interface.

The relative density ρ_r of cold sintered ceramics follows the order $\rho_{CSP\_AM16h} < \rho_{CSP\_AM8h} < \rho_{CSP\_BM12h}$ and the same ordering applies to the ceramics mechanical resistance. The decrease in particle size did result in stronger

agglomeration phenomena (as previously referred) that limits liquid infiltration between particles and inter-agglomerate pores. Elsewhere, the accumulation of liquid may have melted the smaller particles, which in turn may have enhanced the amount of melt and provided local precipitation phenomena. Additionally, the uneven distribution of the flux may have originated areas depleted of flux where the accommodation and rearrangement of the particles became compromised [5]. Melting flux at the CSP temperature allows for rearrangement and compaction. This behavior is facilitated if an optimal particle distribution is present. From this set of results, it can be interpreted that the BM12h powder presented a better particle distribution (a bimodal one) when compared to the finer powder, thus providing better conditions for densification.

Regarding to flux-rich zones, their role in the CSP is not yet well understood and discussed in the literature [11,37,47,63]. At a preliminary stage it has been suggested that flux-rich regions would form hydroxide islands that segregate and precipitate at the grain boundaries. Such intermediate phase, often regarded as an amorphous phase, glues the particles together, and forms glass/crystal composites [37,47]. In an attempt to better understand the role of hydroxide flux, Ndayishimiye et al. [77] performed a simulation of the dynamics between sodium and potassium hydroxides and $BaTiO_3$ (BT) using the ReaxFF Molecular Dynamics software. Their previous finding through SEM images revealed residues of NaOH in greater abundance than KOH. Besides that, it was found through STEM-EDS observations K segregation at the grain boundaries and its incorporation up to 3-4 atomic layers of the BT surface. From ReaxFF simulations, it was shown that as soon as the temperature was increased, hydroxides could create both ionic clusters and poly nucleic complexes (e.g. nNaOH + mKOH $\rightarrow$Na$_n$K$_m$(OH)$_{n+m}$) or ionic dissociation on the surface of BT. KOH clusters are less stable than NaOH clusters and require lower temperatures for dissociation, therefore forming fewer KOH residues than NaOH. Nevertheless, dynamics occurring between the K^+ and Na^+ ions on the surface of the BT enabled subsequent dissolution-precipitation at a broader scale to densify the material.

The CSP reported here demonstrated that a good particle size distribution and a final high relative density (dense ceramics) did not provide a sufficient condition to obtain mechanically resistant ceramics, possibly because inter-grain-

precipitation at a large scale did not occur as extensively as required for obtaining a fully densified ceramic.

3.2.2. Electrical characterizations

The dielectric behavior as a function of temperature at 1 kHz and 1MHz, for CS1120 ceramic, was recorded during cooling from 500º C to room temperature and is graphically displayed in figure 3.12. From figure 3.12. a), at 1 kHz, the KNN CS1120 dielectric curve displays the two characteristic peaks of the phase transition, with a first peak located around ~175 ℃ attributed to the orthorhombic to tetragonal phase transition temperature, T_{O-T}, and the second peak close to 400 °C attributed to the tetragonal to cubic phase transition temperature, T_{T-C}, i.e. the Curie temperature (T_c). However, the presence of an intermediate peak around 270 °C, and the excessive values of permittivity and dielectric loss at the T_{T-C} transition temperature, are atypical of a conventionally sintered KNN [55,57,60,78].

In the case of figure 3.12. b) the graph plotted with results obtained at 1 MHz, reveals a different scenario where the two peaks referring to the typical phase transitions and the dielectric curve values already resemble those reported in the literature for KNN ceramics [60,78]. The relative permittivity at room temperature is ~325, reaching a maximum value of 5703 and losses less than 1 at T_{T-C} temperature.
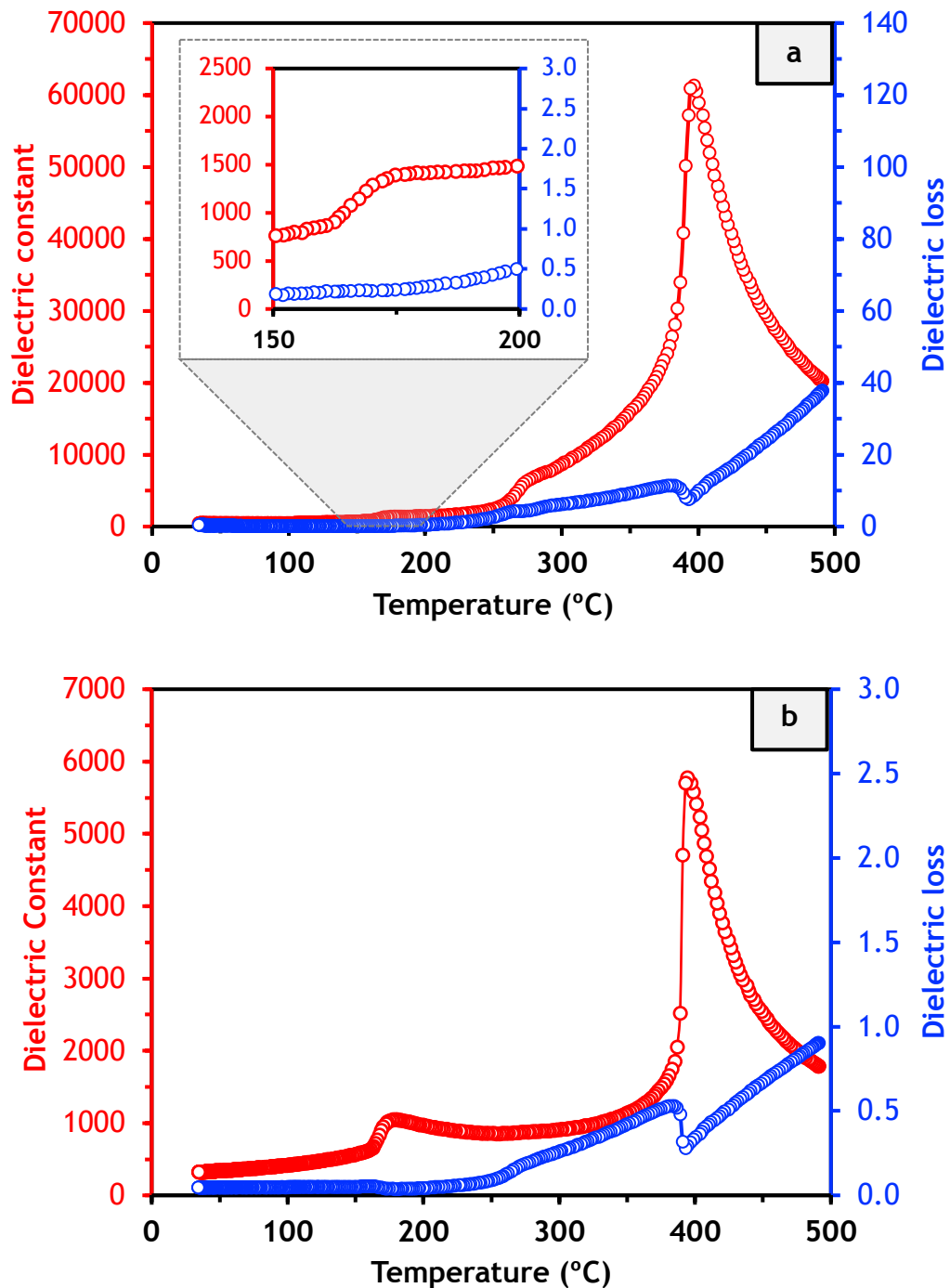
Figure 3.12. Temperature dependence of the dielectric properties of CS1120 ceramics at a) 1kHz and b) 1MHz.

In the context of the physical appearance of the tested samples, a color change was observed in the parallel faces of the ceramic pellet after the dielectric measurements. Before the dielectric measurement, the CS1120 had a beige-white color (figure 3.13.a), but after the dielectric measurement, the side section became grayish (figure 3.13.b). The silver used as electrode was suspended in a

solution of methyl isobutylketone (according to the *Agar Scientific* website [79]) and possibly silver diffusion to the interior of the ceramic took place, with subsequent deposition on the side faces of the ceramic pellet. To access this possibility, the lateral section of the pellet was taken for SEM-EDS analysis (3.13.c) and the presence of ~1 at. % of Ag element could be identified.

Given these results, it is proposed an interfacial polarization phenomenon accounting for the appearance of the peak between 200-300º C while raising very high permittivity values in the vicinity of the T_{T-C}. At a microscopic level, the total polarization (α_{Total}) of a dielectric corresponds to the sum of one or more polarization contributions, namely the electronic (or atomic), ionic, orientational (or dipole) and spatial charge (or interfacial) polarization [80].

$$\alpha_{Total} = \alpha_{electronic} + \alpha_{ionic} + \alpha_{orientational} + \alpha_{spatial\ charge}$$

The contribution of each polarization mechanism follows the order $\alpha_{electronic} < \alpha_{ionic} < \alpha_{orientational} < \alpha_{spatial\ charge}$. As the frequency of change in the electric field increases, there is a decrease in the ability of a material's dipoles to align, hence triggering drops in permittivity values with frequency [80].

Interface polarization is the one that hardly "follows" the frequency of change of the electric field direction, and only contributes to the total polarization at low frequencies ($<10^5$ Hz). This polarization is a result of the migration of charge carriers under an applied electric field, and its accumulation at the interfaces: grain boundaries, cracks, pores, electrode/dielectric material interface, and polyphase materials (i.e. more conductive and less conductive phases) [80]. In the present work, the silver deposited on the lateral surface potentially acted as a second (and more conductive) phase, which allowed the accumulation of charge carriers at "KNN grain-Ag" interface. As this process depends on the mobility of charge carriers, the polarization due to spatial charge is strongly dependent on the temperature and, therefore, unrealistic permittivity values at higher temperatures (T_C neighborhood) are observed. The presence of this type of polarization at low frequencies masks the real dielectric behavior of the material. The 1 MHz graph is thus considered as representative of the dielectric behavior for CS1120 ceramic.
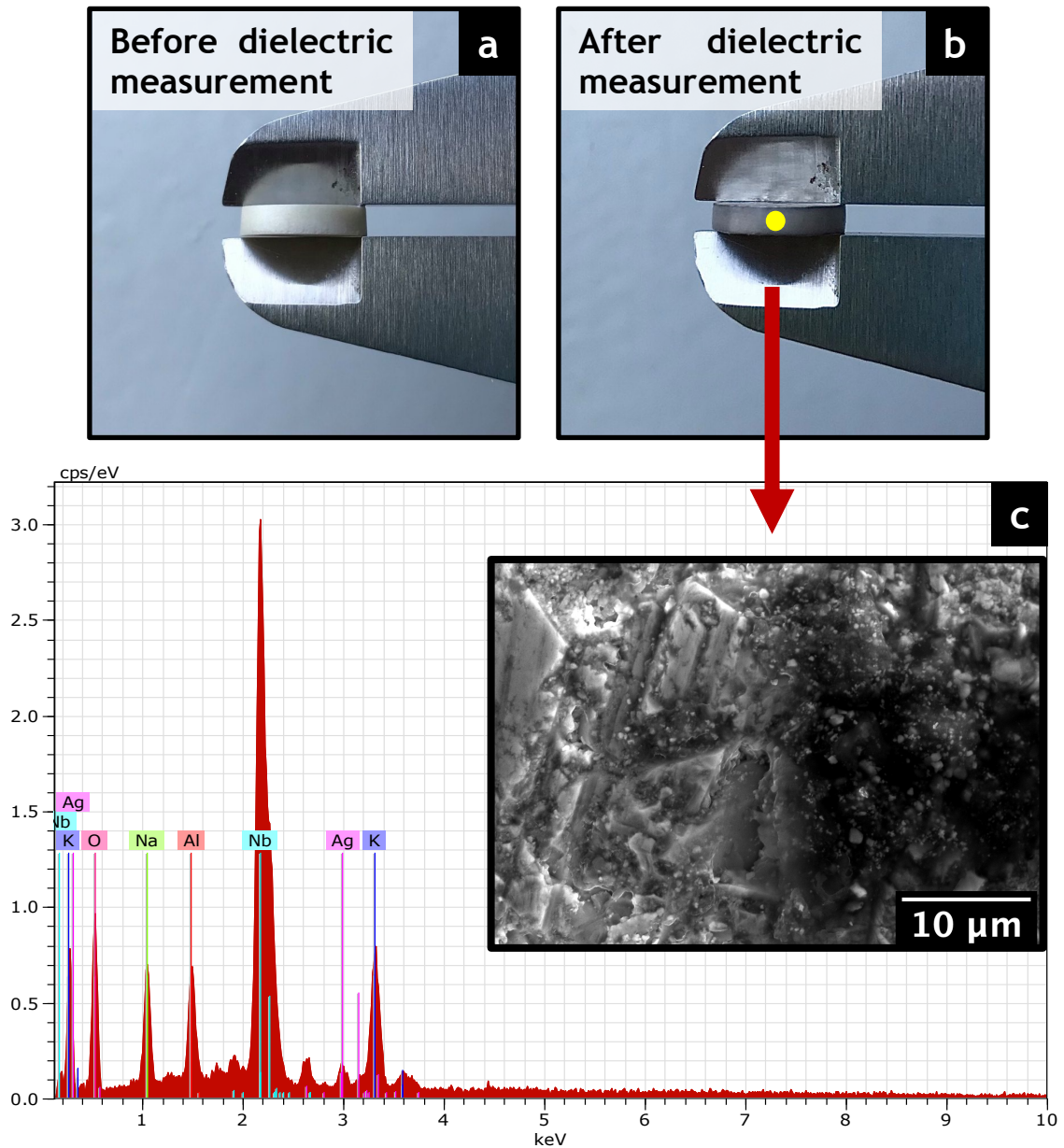
Figure 3.13. CS1120 ceramic pellet a) as-prepared, b) after dielectric measurement, and c) SE micrography of the lateral section right after dielectric measurement. The Al signal come from the SEM holder.

The temperature dependence of the dielectric constant and loss, at 1 kHz and 1 MHz, of cold sintered ceramics is plotted in the figures 3.14. to 3.16. The discussion of dielectric properties will be here centered on the frequency of 1 MHz, thus discarding the possible interfacial polarization phenomena due to silver, present at low frequency (1 kHz).
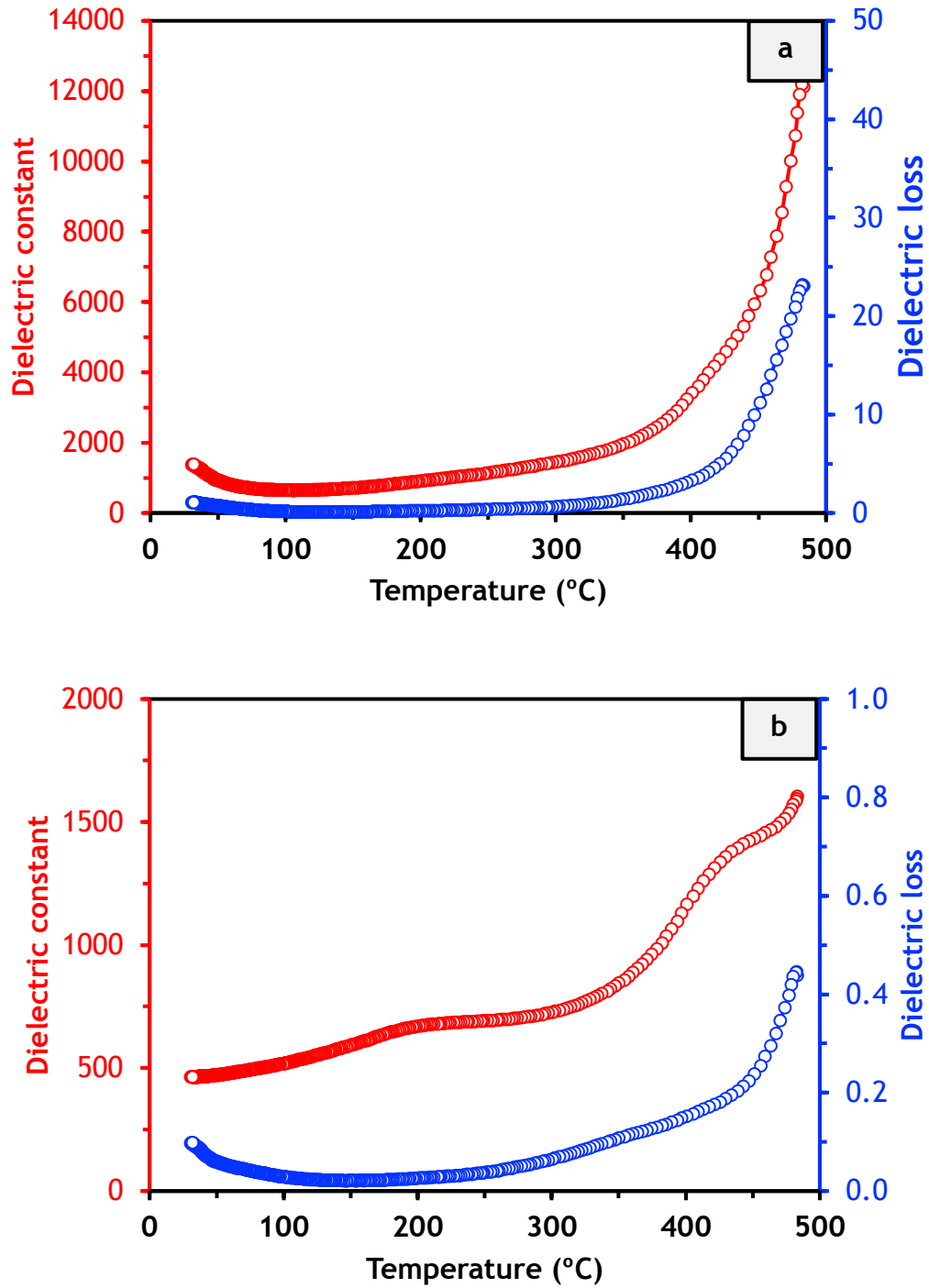
Figure 3.14. Temperature dependence of the dielectric properties of CSP_BM12h ceramics at a) 1kHz and b) 1MHz.
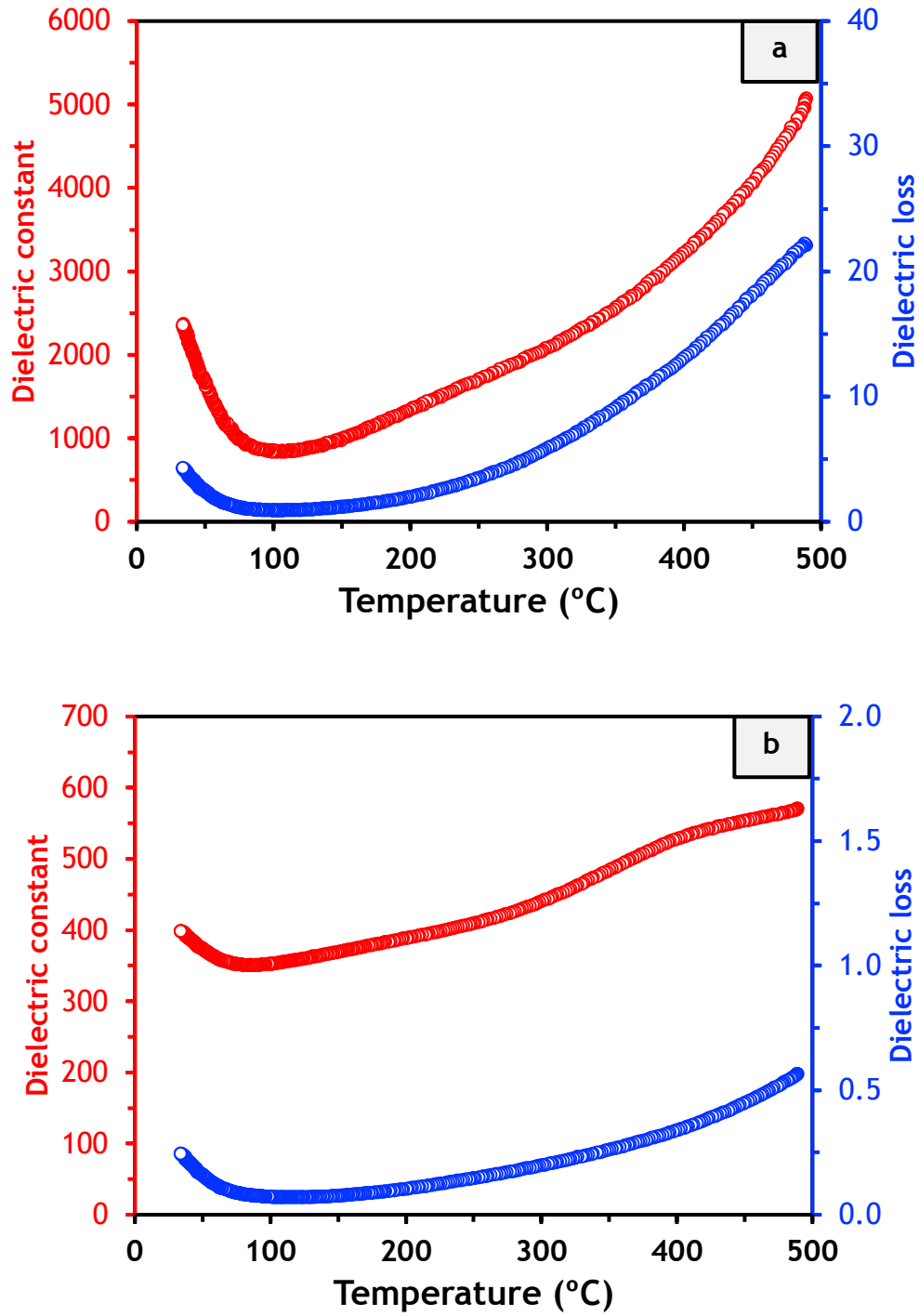
Figure 3.15. Temperature dependence of the dielectric properties of CSP_AM8h ceramics at a) 1kHz and b) 1MHz.
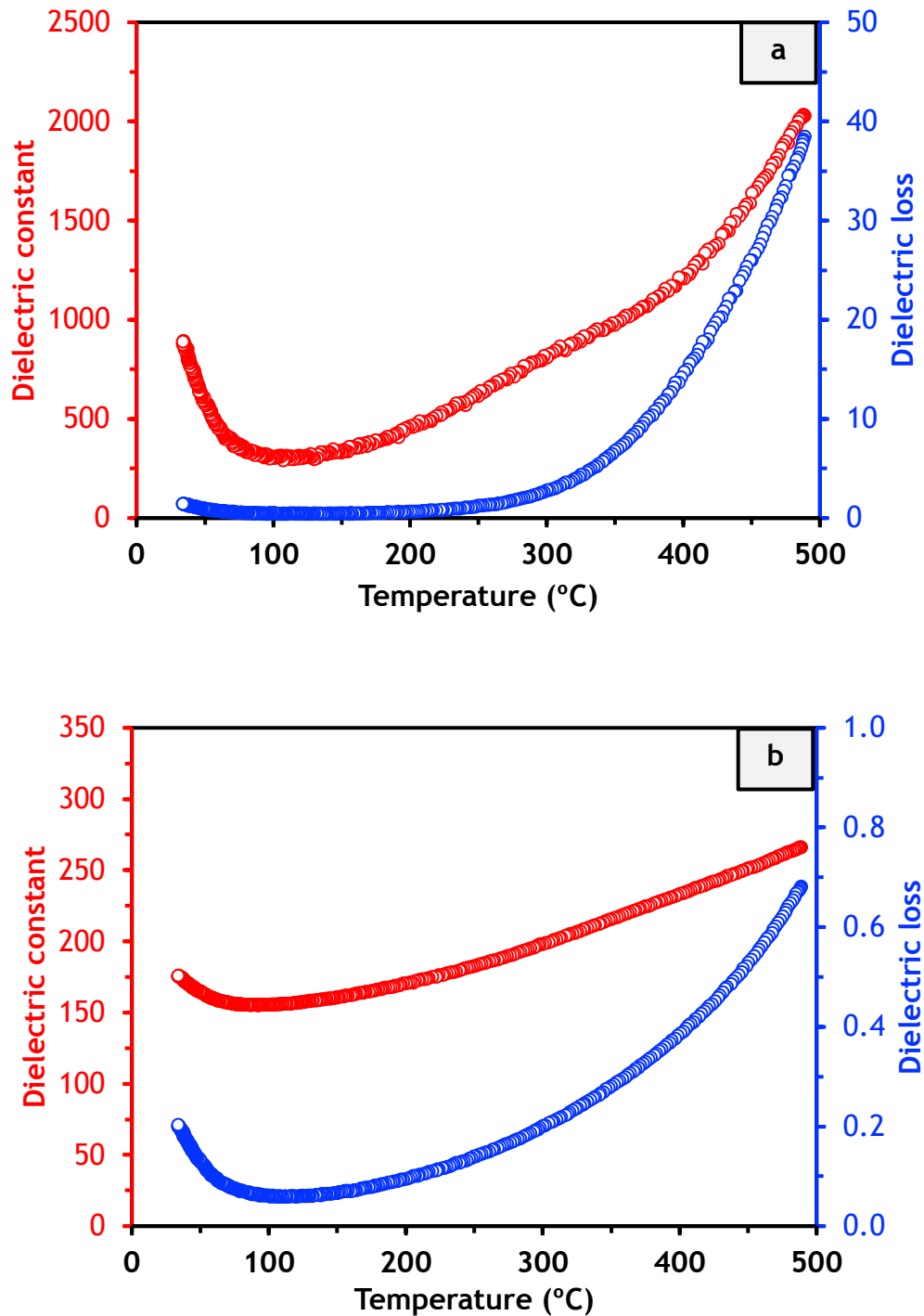
Figure 3.16. Temperature dependence of the dielectric properties of CSP_AM16h ceramics at a) 1kHz and b) 1MHz.

Figure 3.14.b) shows two shoulders at temperatures of ~200 °C and ~400 °C, coinciding with orthorrombic-tetragonal and tetragonal-cubic phase transitions temperatures. With the use of finer particles, the shoulders observed near the

phase transitions temperatures gradually disappear, and the permittivity values, at room temperature, decrease from 464 of CSP_BM12h to ~ 394 for CSP_AM8h (figure 3.15.b) and ~ 170 for CSP_AM16h (figure 3.16. b). This finding can be explained by the decrease of ceramics density (i.e. increase of porosity) as observed in the figure 3.9 a and 3.10.b. Additionally, it is referred in the literature that for ceramics with very small sized grains, the large amount of low-ε grain boundaries may dilute the effect of polarization of the ferroelectric domains [46]. [46]. Furthermore, the existence of NaK flux at the grain boundaries can mask and even negatively influence the dielectric constant. To date, the influence of hydroxide flux on the electrical properties of a CSPed ceramics is scarcely documented.

The piezoelectric properties of KNN prepared ceramics are presented in table 3.6. Under the poling conditions described in this study, CS1120 ceramic exhibited a d_{33} of 100 pC/N, while CSP_BM12h presented a value of 10 pC/N, and CSPed ceramics using AM powders do not show a piezoelectric response. CS1120 possesses a higher piezoelectric coefficient than CSPed ceramics, demonstrating that although through CSP it is possible to densify ceramics up to 95% (CSP_BM12h), the high-temperature conventional sintering did provide high densification associated with superior piezoelectric behavior than CSP ceramics.

Table 3.6. Piezoelectric coefficient d_{33} of the produced ceramics.

Ceramic	d_{33} (pC/N)
CS1120	100
CSP_BM12h	10
CSP_AM8h	0
CSP_AM16	0

Comparing the d_{33} values of the CSPed ceramics in the present work with the values reported by Chi et al. [9], there is a notable difference. The authors reported d_{33} values around 17 pC/N for KNN green compacts and 51 pC/N for CSPed ceramics (120 °C/aqueous NaCl solution), whereas the d_{33} herein presented

reaches only 10 pC /N for the highly dense CSP_BM12h ceramic. This observation suggests that the poling conditions used in the present study are not optimized yet. In this case, a more systematic investigation is needed.

For P-E studies, only conventional and CSP_BM12h samples were used, since the ceramics produced with AM powders did not present a relevant electrical behavior.

Preliminary studies were carried out to assess the adequacy of silver electrodes (either by painting or sputtering) to measure ferroelectric polarization hysteresis loops. It was observed that during the ferroelectric measurements, the surface adjacent to the silver electrode exhibited a grey color that resulted from silver ions migration through the CSP_BM12h ceramic, which led to extremely high polarization values for low electrical fields (see Appendix 1). Therefore, gold electrodes were used to avoid possible ions migration and interfacial polarization phenomena, thus enabling the results presented below.

Figure 3.17. ((a) and (b)) shows the P-E hysteresis loop, at 10 Hz, of CS1120 and CSP_BM12h ceramic (respectively). For CS1120 the remnant polarization P_r is 25.17 $\mu C/cm^2$ and the coercive field E_c is 24.54 kV/cm. Note that the P_r of CS1120 is higher than the polarization at higher fields and the polarization loop does not saturate, thus presenting a rounded shape. This reveals the leaky feature of the ceramic. It is mentioned in the literature that, at room temperature, conventional sintered KNN shows some electric conduction that can be slightly suppressed by doping with 0.5 mol % of manganese, thus improving its P-E loop [81]. Furthermore, it is also reported that, frequently, conductivity may coexist with the ferroelectric behavior of a sample, making its ferroelectric characterization difficult [82]. The CSP_BM12h ceramic presents a P-E loop denoting a leaky behavior too, with a P_r of 4.22 $\mu C/cm^2$, and a E_c of 21.3 kV/cm. Although presenting a lower polarization value, CSP_BM12h showed a lower coercive field than CS1120.
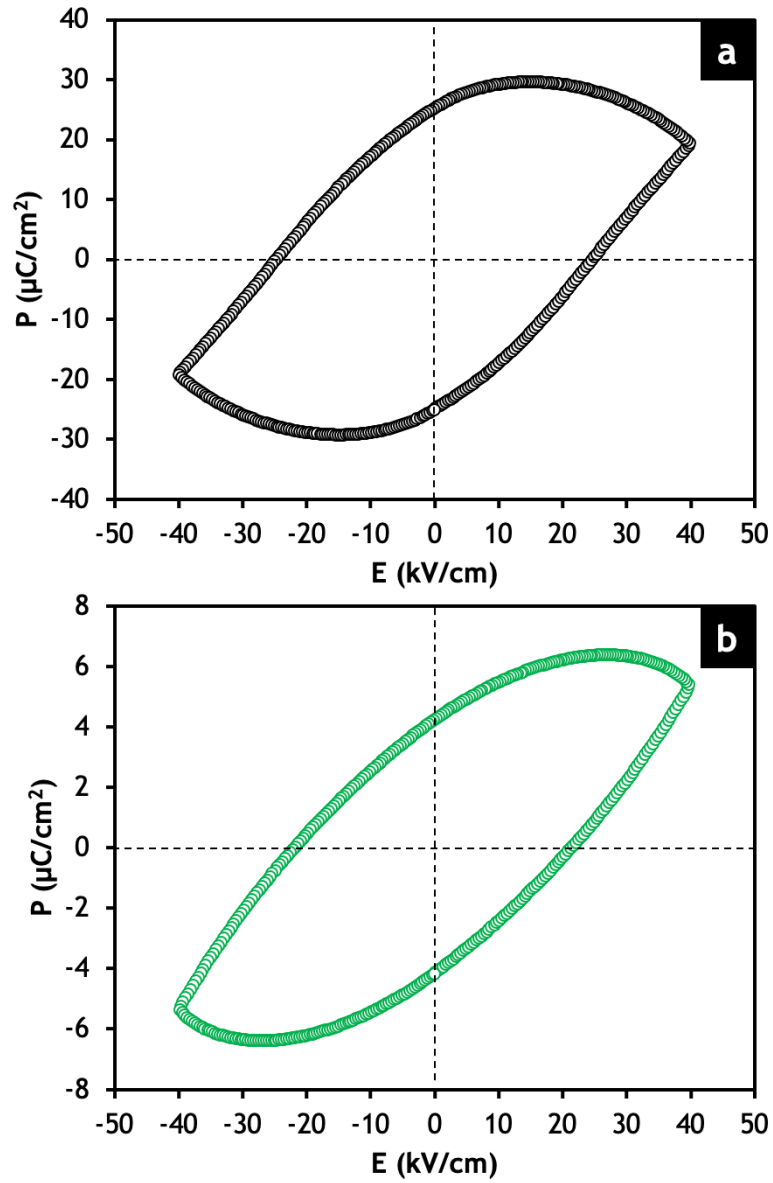
Figure 3.17. Room temperature hysteresis loop of a) CS1120 and b) CSP_BM12h ceramic (f=10 Hz).

The topographic and in/out-plane PFM images are shown below (figure 3.18).
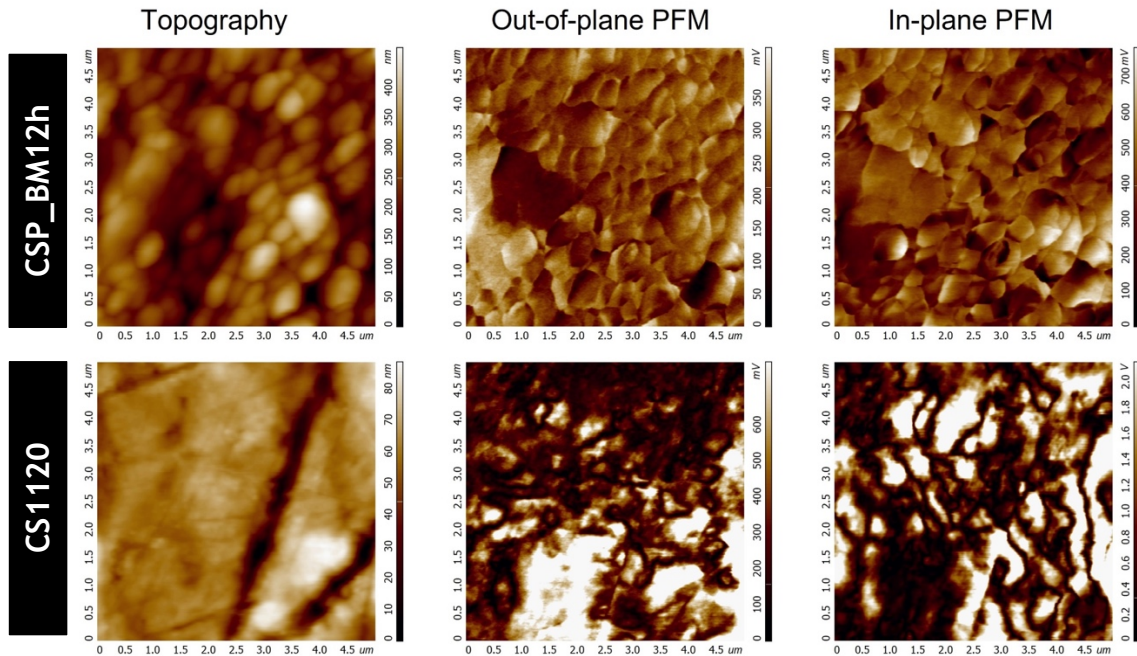
Figure 3.18. Topographic and PFM images of CS1120 and CSP_BM12h ceramics (5x5 μm).

The AFM/PFM scan done at 5 x 5 μm shows the distinct difference in grain size distribution. The CS1120 has larger grains with the signs related to the previous polishing procedure. The CSP_BM12h has smaller grain size with very dense packed grains. These results are in good agreement with the SEM analysis (figure 3.7.c). The PFM response from conventionally sintered sample revealed multidomain states within one grain, while the CSP_BM12h shows the monodomain state for each grain.

Figure 3.19. Topographic and PFM images of CS1120 and CSP_BM12h ceramics (2.5x2.5 μm).

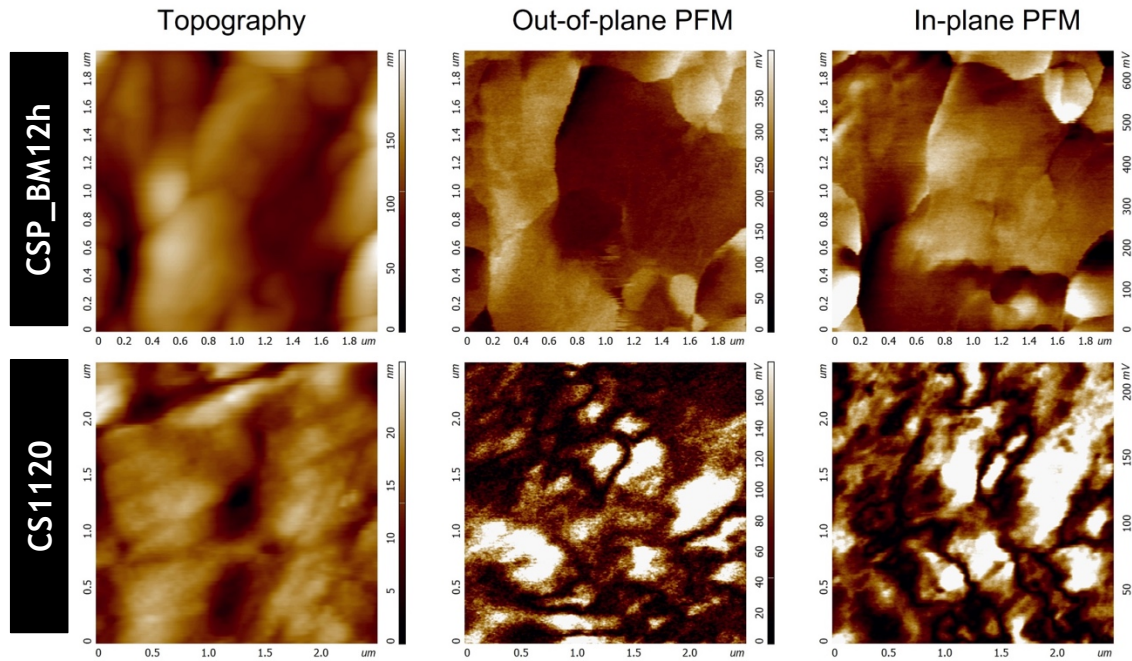The increased resolution of the AFM/PFM scan (figure 3.19) displays the principal difference between the two sintering methods. The conventional sintering method allows to obtain big-sized grains with complicated domain structures. These domain structures are cross-correlated in both out-of-plane and in-plane projections. This means a moderate piezoresponse due to the opposite orientation of each domain polarization. The CSP approach allowed the polarization from each grain to remain in a monodomain state and enabled a region where several grains have the same orientation of polarization. The polarization at this region is enhanced by multiple in-phase monodomains that would yield in higher piezoresponse at the macroscale. However, these monodomains do not constitute the majority of the ceramic, being located in punctual areas, which might explain the lower piezoelectric value for CSP_BM12h at the macroscopic level.

It should be noted that the present results allow expecting that, if ideal conditions are met so that dissolution-precipitation phenomena are triggered at a larger scale, i.e. filling in the inter-particle free spaces, then large amount of regions with multiple grains with the same orientation of polarization will form.

It is envisaged that this will contribute to a significant improvement in the piezoelectric coefficient at a macroscopic level.

4. Conclusions and Future work

In this work, the influence of the particle morphology of KNN powder was studied for a cold sintering system assisted by sodium and potassium hydroxide flux and compared step-step with a conventionally sintered ceramic. Some general conclusions and future work suggestions can be drawn from this work, which are summarized below.

KNN particles with different morphologies (shape, size and size distributions) were produced by combining ball milling and attrition milling proccesses. Under conventional sintering conditions, the finer the KNN particles (i.e. the larger its specific surface area) the lower would be their sintering temperature. However, when using the cold sintering process, and under the used cold sintering conditions (T=250 °C, t=2h and P=500 MPa) assisted by a NaK flux, the decrease of KNN particle size had detrimental consequences on the ceramic density with negative effects on the final mechanical and electrical performance of the CSPed ceramics. The reduction in particle size favored interparticle agglomeration that was thought to hinder the flux infiltration into pores. Consequently, the uneven distribution of the flux did result in local excess of melt in some regions where precipitation was favoured, sometimes accompanied by porosity development. The powder submitted to milder conditions (12 h of ball milling) was the one presenting larger particles coexisting with smaller sized ones, with a bimodal size distribution. This was the powder ensuring a good initial compaction of the particles and therefore facilitating densification. CSPed ceramics with a relative density as high as 96% were obtained.

Despite the obtained high densities (96%), the final properties of KNN CSPed ceramics such as compressive strength (here reported for the first time) or piezoelectric constant d_{33} are still very modest, not comparable to those exhibited by conventionally sintered ceramic. The high pressure combined with the presence of a liquid phase, and temperature allowed the densification of the material to occur. Nevertheless, the present results allow concluding that the CSP

succeeds to densify KNN but without triggering extensive dissolution-precipitation phenomena able to bind the particles. A better solvent distribution and/or a longer dwell time are variables to be further explored to enhance dissolution-precipitation phenomena on a wide scale. Furthermore, the composition of the flux is also an open variable to be considered as when local flux acumulation was enabled, a local excess of sodium was noticed. Also, the chemical condition of KNN particles surface which was not addressed in the present study, is also envisaged as a promising variable to be studied.

The piezoelectric behavior at the nanoscale reflects directly on the macroscale response. The preferential orientation of the domains verified in the ceramic CSP_BM12h might lead to high piezoelectric constant if regions of multiple grains having the same orientation of polarization are formed. However, such condition was not reached yet. It has been reported in the literature that post-annealing steps are effective to enhance the electrical characteristics of CSPed ceramics. This can be a path to be explored in a future work.

References

[1]   R.E. Newnham, T.R. Shrout, Advanced Ceramics, Electronic Ceramics, Kirk-Othmer Encycl. Chem. Technol. (2000). https://doi.org/10.1002/0471238961.0512050314052314.a01.

[2]   T. Ibn-Mohammed, C.A. Randall, K.B. Mustapha, J. Guo, J. Walker, S. Berbano, S.C.L. Koh, D. Wang, D.C. Sinclair, I.M. Reaney, Decarbonising ceramic manufacturing: A techno-economic analysis of energy efficient sintering technologies in the functional materials sector, J. Eur. Ceram. Soc. 39 (2019) 5213–5235. https://doi.org/10.1016/j.jeurceramsoc.2019.08.011.

[3]   J. Guo, R. Floyd, S. Lowum, J.-P. Maria, T. Herisson de Beauvoir, J.-H. Seo, C.A. Randall, Cold Sintering: Progress, Challenges, and Future Opportunities, Annu. Rev. Mater. Res. 49 (2019) 275–295. https://doi.org/10.1146/annurev-matsci-070218-010041.

[4]   H. Guo, A. Baker, J. Guo, C.A. Randall, Protocol for Ultralow-Temperature Ceramic Sintering: An Integration of Nanotechnology and the Cold Sintering Process, ACS Nano. 10 (2016) 10606–10614. https://doi.org/10.1021/acsnano.6b03800.

[5]   K. Nur, T.P. Mishra, J.G.P. da Silva, J. Gonzalez-Julian, M. Bram, O. Guillon, Influence of powder characteristics on cold sintering of nano-sized ZnO with density above 99 %, J. Eur. Ceram. Soc. 41 (2021) 2648–2662. https://doi.org/10.1016/j.jeurceramsoc.2020.11.007.

[6]   R. Zuo, J. Rödel, R. Chen, L. Li, Sintering and electrical properties of lead-free Na0.5K 0.5NbO3 piezoelectric ceramics, J. Am. Ceram. Soc. 89 (2006) 2010–2015. https://doi.org/10.1111/j.1551-2916.2006.00991.x.

[7]   C. Jiten, A.K. Nath, K.C. Singh, R. Laishram, O.P. Thakur, D.K. Bhattacharya, Electrical and Piezoelectric Properties of Lead-Free (K 0.5 Na 0.5)(Nb 0.9 Ta 0.1)O 3 Ceramics Prepared From Nanopowders, Integr. Ferroelectr. 118 (2010) 1–7. https://doi.org/10.1080/10584587.2010.489460.

[8]   J. Ma, H. Li, H. Wang, C. Lin, X. Wu, T. Lin, X. Zheng, X. Yu, Composition, microstructure and electrical properties of K0.5Na0.5NbO3 ceramics fabricated by cold sintering assisted sintering, J. Eur. Ceram. Soc. 39 (2019) 986–993. https://doi.org/10.1016/j.jeurceramsoc.2018.11.044.

[9]   M. Chi, W. Ma, J. Guo, J. Wu, T. Li, S. Wang, P. Zhang, Effect of NaCl on the microstructure and electrical properties of K0.5Na0.5NbO3 ceramics prepared by cold sintering process, J. Mater. Sci. Mater. Electron. 30 (2019) 21435–21443. https://doi.org/10.1007/s10854-019-02523-2.

[10]   B. Deng, Y. Ma, T. Chen, H. Wang, J. Lin, C. Lin, X. Wu, C. Zhao, T. Lin, M. Gao, X. Zheng, C. Fang, Elevating electrical properties of (K, Na)NbO 3 ceramics via cold sintering process and post-annealing, J. Am. Ceram. Soc.

(2021). https://doi.org/10.1111/jace.18103.

[11] L. Cong, W. Huajing, M. Jianzhang, D. Baoyu, W. Xiao, L. Tengfei, Z. Xinghua, Y. Xing, Effect of dwell time on cold sintering assisted sintering based highly transparent 0.9K0.5Na0.5NbO3-0.1LiBiO3 ceramics, J. Alloys Compd. 826 (2020) 154249. https://doi.org/10.1016/j.jallcom.2020.154249.

[12] M.N. Rahaman, Sintering of Ceramics, CRC Press, 2007. https://doi.org/10.1201/b15869.

[13] C. Baud, Sintering, Encycl. Phys. Sci. Technol. (Third Ed. (2003) 865–878. https://doi.org/https://doi.org/10.1016/B0-12-227410-5/00694-3.

[14] S.-J.L. Kang, Sintering Processes, in: Sinter. Densif. Grain Growth, Microstruct., Elsevier, 2005: pp. 3–8. https://doi.org/10.1016/b978-075066385-4/50001-7.

[15] M. Oghbaei, O. Mirzaee, Microwave versus conventional sintering: A review of fundamentals, advantages and applications, J. Alloys Compd. 494 (2010) 175–189. https://doi.org/10.1016/j.jallcom.2010.01.068.

[16] R.J. Brook, Sintering: An Overview, Concise Encycl. Adv. Ceram. Mater. (1991) 438–440. https://doi.org/10.1016/b978-0-08-034720-2.50121-0.

[17] P.M. Derlet, Sintering Theory, (2017). https://www.epfl.ch/labs/lmc/wp-content/uploads/2018/06/PowderTech-11.pdf (accessed November 21, 2020).

[18] W.D. Kingery, M.D. Narasimhan, Densification during sintering in the presence of a liquid phase. II. Experimental, J. Appl. Phys. 30 (1959) 307–310. https://doi.org/10.1063/1.1735156.

[19] R.M. German, P. Suri, S.J. Park, Review: Liquid phase sintering, J. Mater. Sci. 44 (2009) 1–39. https://doi.org/10.1007/s10853-008-3008-0.

[20] J.S. Moya, S. Lopez-Esteban, C. Pecharromán, The challenge of ceramic/metal microcomposites and nanocomposites, Prog. Mater. Sci. 52 (2007) 1017–1090. https://doi.org/10.1016/j.pmatsci.2006.09.003.

[21] J. Andrews, D. Button, I.M. Reaney, Advances in Cold Sintering : Improving energy consumption and unlocking new potential in component manufacturing, Johnson Matthey Technol. Rev. 64 (2020) 219–232. https://doi.org/10.1595/205651320X15814150061554.

[22] Tangram Technologies, Energy efficiency in ceramics processing Practical worksheets for industry, 2012. https://www.tangram.co.uk/TI-Energy Worksheets (Ceramics) - Tangram.pdf.

[23] WSP Parson Brinkerhoff and DNV GL, Industrial Decarbonisation & Energy Efficiency Roadmaps to 2050: Cross Sector Summary, Glass, Cement and Pulp and Paper Reports, (2015) 31. https://www.gov.uk/government/publications/industrial-decarbonisation-and-energy-efficiency-roadmaps-to-2050.

[24] E. Comission, The European Green Deal, (2019). https://ec.europa.eu/commission/presscorner/detail/e   n/ip_19_6691

(accessed November 14, 2020).

[25] R.M. German, Sintering With External Pressure, in: Sinter. from Empir. Obs. to Sci. Princ., Elsevier, 2014: pp. 305–354. https://doi.org/10.1016/B978-0-12-401682-8.00010-0.

[26] C. Hu, F. Li, D. Qu, Q. Wang, R. Xie, H. Zhang, S. Peng, Y. Bao, Y. Zhou, Developments in hot pressing (HP) and hot isostatic pressing (HIP) of ceramic matrix composites, Adv. Ceram. Matrix Compos. (2014) 164–189. https://doi.org/10.1533/9780857098825.1.164.

[27] L.A. Dobrzanski, A.D. Dobrzanska-Danikiewicz, A. Achtelik-Franczak, L.B. Dobrzanski, E. Hajduczek, G. Matula, Fabrication Technologies of the Sintered Materials Including Materials for Medical and Dental Application, Powder Metall. - Fundam. Case Stud. (2017). https://doi.org/10.5772/65376.

[28] E.A. Olevsky, D. V. Dudina, Field-assisted sintering: Science and applications, Springer, Switzerland, 2018. https://doi.org/10.1007/978-3-319-76032-2.

[29] A. Borrell, M.D. Salvador, Advanced Ceramic Materials Sintered by Microwave Technology, in: Sinter. Technol. - Method Appl., InTech, 2018. https://doi.org/10.5772/intechopen.78831.

[30] A.V. Ragulya, Fundamentals of Spark Plasma Sintering, Encycl. Mater. Sci. Technol. (2010) 1. https://doi.org/10.1016/b978-008043152-9.02249-1.

[31] U. Anselmi-Tamburini, Spark Plasma Sintering, Ref. Modul. Mater. Sci. Mater. Eng. d (2019) 1–17. https://doi.org/10.1016/b978-0-12-803581-8.11730-8.

[32] Diagram of spark plasma sintering plant | Download Scientific Diagram, (n.d.). https://www.researchgate.net/figure/Diagram-of-spark-plasma-sintering-plant_fig2_283790610 (accessed November 30, 2020).

[33] M. Cologna, B. Rashkova, R. Raj, Flash sintering of nanograin zirconia in <5 s at 850°C, J. Am. Ceram. Soc. 93 (2010) 3556–3559. https://doi.org/10.1111/j.1551-2916.2010.04089.x.

[34] M. Biesuz, V.M. Sglavo, Flash sintering of ceramics, J. Eur. Ceram. Soc. 39 (2019) 115–143. https://doi.org/10.1016/j.jeurceramsoc.2018.08.048.

[35] M. Yu, S. Grasso, R. Mckinnon, T. Saunders, M.J. Reece, Review of flash sintering: materials, mechanisms and modelling, Adv. Appl. Ceram. 116 (2017) 24–60. https://doi.org/10.1080/17436753.2016.1251051.

[36] J.A. Downs, V.M. Sglavo, Electric field assisted sintering of cubic zirconia at 390°C, J. Am. Ceram. Soc. 96 (2013) 1342–1344. https://doi.org/10.1111/jace.12281.

[37] H. Guo, J. Guo, A. Baker, C.A. Randall, Hydrothermal-Assisted Cold Sintering Process: A New Guidance for Low-Temperature Ceramic Sintering, ACS Appl. Mater. Interfaces. 8 (2016) 20909–20915. https://doi.org/10.1021/acsami.6b07481.

[38] H. Guo, A. Baker, J. Guo, C.A. Randall, Cold Sintering Process: A Novel Technique for Low-Temperature Ceramic Processing of Ferroelectrics, J. Am.

Ceram. Soc. 99 (2016) 3489–3507. https://doi.org/10.1111/jace.14554.

[39] J. Song, G. Zhu, H. Xu, W. Fu, J. Xu, J. Zhang, S. Huang, A. Yu, Preparation and properties of high-density Bi2O3 ceramics by cold sintering, Ceram. Int. 46 (2020) 13848–13853. https://doi.org/10.1016/j.ceramint.2020.02.177.

[40] J.P. Maria, X. Kang, R.D. Floyd, E.C. Dickey, H. Guo, J. Guo, A. Baker, S. Funihashi, C.A. Randall, Cold sintering: Current status and prospects, J. Mater. Res. 32 (2017) 3205–3218. https://doi.org/10.1557/jmr.2017.262.

[41] J. Guo, H. Guo, A.L. Baker, M.T. Lanagan, E.R. Kupp, G.L. Messing, C.A. Randall, Cold Sintering: A Paradigm Shift for Processing and Integration of Ceramics, Angew. Chemie - Int. Ed. 55 (2016) 11457–11461. https://doi.org/10.1002/anie.201605443.

[42] S. Funahashi, J. Guo, H. Guo, K. Wang, A.L. Baker, K. Shiratsuyu, C.A. Randall, Demonstration of the cold sintering process study for the densification and grain growth of ZnO ceramics, J. Am. Ceram. Soc. 100 (2017) 546–553. https://doi.org/10.1111/jace.14617.

[43] M.C. Blanco-Lopez, B. Rand, F.L. Riley, The Properties of Aqueous Phase Suspensions of Barium Titanate, J. Eur. Ceram. Soc. 17 (1997) 281–287. https://doi.org/10.1016/s0955-2219(96)00116-1.

[44] D. Wang, H. Guo, C.S. Morandi, C.A. Randall, S. Trolier-McKinstry, Cold sintering and electrical characterization of lead zirconate titanate piezoelectric ceramics, APL Mater. 6 (2018). https://doi.org/10.1063/1.5004420.

[45] V.R. Mudinepalli, L. Feng, W.C. Lin, B.S. Murty, Effect of grain size on dielectric and ferroelectric properties of nanostructured Ba0.8Sr0.2TiO3 ceramics, J. Adv. Ceram. 4 (2015) 46–53. https://doi.org/10.1007/s40145-015-0130-8.

[46] Y. Huan, X. Wang, J. Fang, L. Li, Grain size effects on piezoelectric properties and domain structure of BaTiO 3 ceramics prepared by two-step sintering, J. Am. Ceram. Soc. 96 (2013) 3369–3371. https://doi.org/10.1111/jace.12601.

[47] K. Tsuji, A. Ndayishimiye, S. Lowum, R. Floyd, K. Wang, M. Wetherington, J.P. Maria, C.A. Randall, Single step densification of high permittivity BaTiO3 ceramics at 300 °C, J. Eur. Ceram. Soc. 40 (2020) 1280–1284. https://doi.org/10.1016/j.jeurceramsoc.2019.12.022.

[48] H. Guo, J. Guo, A. Baker, C.A. Randall, Cold sintering process for ZrO2-based ceramics: significantly enhanced densification evolution in yttria-doped ZrO2, J. Am. Ceram. Soc. 100 (2017) 491–495. https://doi.org/10.1111/jace.14593.

[49] T. Sada, K. Tsuji, A. Ndayishimiye, Z. Fan, Y. Fujioka, C.A. Randall, Enhanced high permittivity BaTiO3-polymer nanocomposites from the cold sintering process, J. Appl. Phys. 128 (2020). https://doi.org/10.1063/5.0021040.

[50] S. Dursun, K. Tsuji, S.H. Bang, A. Ndayishimiye, C.A. Randall, A Route

towards Fabrication of Functional Ceramic/Polymer Nanocomposite Devices Using the Cold Sintering Process, ACS Appl. Electron. Mater. 2 (2020) 1917–1924. https://doi.org/10.1021/acsaelm.0c00225.

[51] X. Zhao, J. Guo, K. Wang, T. Herisson De Beauvoir, B. Li, C.A. Randall, Introducing a ZnO–PTFE (Polymer) Nanocomposite Varistor via the Cold Sintering Process, Adv. Eng. Mater. 20 (2018) 1–8. https://doi.org/10.1002/adem.201700902.

[52] S. Grasso, M. Biesuz, L. Zoli, G. Taveri, A.I. Duff, D. Ke, A. Jiang, M.J. Reece, A review of cold sintering processes, Adv. Appl. Ceram. 119 (2020) 115–143. https://doi.org/10.1080/17436753.2019.1706825.

[53] W.D. Callister, J. Wiley, Materials Science and Engineering An Introduction, 7th ed., John Wiley & Sons, Inc., New York, 2007.

[54] S. Zhang, R. Xia, T.R. Shrout, Lead-free piezoelectric ceramics vs. PZT?, IEEE Int. Symp. Appl. Ferroelectr. (2006). https://doi.org/10.1109/ISAF.2006.4349278.

[55] J.-F. Li, K. Wang, F.-Y. Zhu, L.-Q. Cheng, F.-Z. Yao, (K,Na)NbO 3 -Based Lead-Free Piezoceramics: Fundamental Aspects, Processing Technologies, and Remaining Challenges, J. Am. Ceram. Soc. 96 (2013) 3677–3696. https://doi.org/10.1111/jace.12715.

[56] D. 2002/95/EC, Restriction of the use of certain hazardous substances in electrical and electronic equipment, Off. J. Eur. Union. L37 (2003) 19–23.

[57] S. Gupta, D. Maurya, Y. Yan, S. Priya, Development of KNN-Based Piezoelectric Materials, in: Lead-Free Piezoelectrics, Springer New York, New York, NY, 2012: pp. 89–119. https://doi.org/10.1007/978-1-4419-9598-8_3.

[58] M. Kosec, B. Malič, A. Benčan, T. Rojac, KNN-Based Piezoelectric Ceramics BT - Piezoelectric and Acoustic Materials for Transducer Applications, in: A. Safari, E.K. Akdoğan (Eds.), Piezoelectric Acoust. Mater. Transducer Appl., Springer US, Boston, MA, 2008: pp. 81–102. https://doi.org/10.1007/978-0-387-76540-2_5.

[59] P. Bomlai, P. Wichianrat, S. Muensit, S.J. Milne, Effect of calcination conditions and excess alkali carbonate on the phase formation and particle morphology of Na0.5K0.5NbO 3 powders, J. Am. Ceram. Soc. 90 (2007) 1650–1655. https://doi.org/10.1111/j.1551-2916.2007.01629.x.

[60] Y. Lee, J. Cho, B. Kim, D. Choi, Piezoelectric Properties and Densification Based on Control of Volatile Mass of Potassium and Sodium in (K 0.5 Na 0.5)NbO 3 Ceramics, Jpn. J. Appl. Phys. 47 (2008) 4620–4622. https://doi.org/10.1143/JJAP.47.4620.

[61] Y.J. Dai, X.W. Zhang, K.P. Chen, Morphotropic phase boundary and electrical properties of K1-x Nax NbO3 lead-free ceramics, Appl. Phys. Lett. 94 (2009) 042905. https://doi.org/10.1063/1.3076105.

[62] O. Ozmen, C. Ozsoy-Keskinbora, E. Suvaci, Chemical stability of KNbO3, NaNbO3, and K0.5Na0.5NbO3 in aqueous medium, J. Am. Ceram. Soc. 101

(2018) 1074–1086. https://doi.org/10.1111/jace.15291.

[63] S. Lowum, R. Floyd, J.P. Maria, Hydroflux-assisted densification: applying flux crystal growth techniques to cold sintering, J. Mater. Sci. 55 (2020) 12747–12760. https://doi.org/10.1007/s10853-020-04926-7.

[64] A. Bishnoi, S. Kumar, N. Joshi, Wide-Angle X-ray Diffraction (WXRD), in: Microsc. Methods Nanomater. Charact., Elsevier, 2017: pp. 313–337. https://doi.org/10.1016/B978-0-323-46141-2.00009-2.

[65] S. Wilschefski, M. Baxter, Inductively Coupled Plasma Mass Spectrometry: Introduction to Analytical Aspects, Clin. Biochem. Rev. 40 (2019) 115–133. https://doi.org/10.33176/AACB-19-00024.

[66] G. Fagerlund, Determination of specific surface by the BET method, Matériaux Constr. 6 (1973) 239–245. https://doi.org/10.1007/BF02479039.

[67] M. Naderi, Surface Area, in: Prog. Filtr. Sep., Elsevier, 2015: pp. 585–608. https://doi.org/10.1016/B978-0-12-384746-1.00014-8.

[68] R.M. German, A measure of the number of particles in agglomerates, Met. Powder Rep. 52 (1997) 35. https://doi.org/10.1016/S0026-0657(97)86577-0.

[69] Piezoelectric Materials: Crystal Orientation and Poling Direction | COMSOL Blog, (n.d.). https://www.comsol.com/blogs/piezoelectric-materials-crystal-orientation-poling-direction/ (accessed July 26, 2021).

[70] M. Rotan, M. Zhuk, J. Glaum, Activation of ferroelectric implant ceramics by corona discharge poling, J. Eur. Ceram. Soc. 40 (2020) 5402–5409. https://doi.org/10.1016/J.JEURCERAMSOC.2020.06.058.

[71] I. Chilibon, J.N. Marat-Mendes, Ferroelectric ceramics by sol-gel methods and applications: A review, J. Sol-Gel Sci. Technol. 64 (2012) 571–611. https://doi.org/10.1007/S10971-012-2891-7.

[72] D. Johnson, N. Hilal, W.R. Bowen, Basic principles of atomic force microscopy, Elsevier Ltd, 2009. https://doi.org/10.1016/B978-1-85617-517-3.00001-8.

[73] E. Soergel, Piezoresponse force microscopy (PFM), J. Phys. D. Appl. Phys. 44 (2011). https://doi.org/10.1088/0022-3727/44/46/464003.

[74] J. Acker, H. Kungl, M.J. Hoffmann, Influence of Alkaline and Niobium Excess on Sintering and Microstructure of Sodium-Potassium Niobate (K 0.5 Na 0.5)NbO 3, J. Am. Ceram. Soc. 93 (2010) 1270–1281. https://doi.org/10.1111/j.1551-2916.2010.03578.x.

[75] R. Serrazina, C. Ribeiro, M.E. Costa, L. Pereira, P.M. Vilarinho, A.M.O.R. Senos, Particle characteristics' influence on FLASH sintering of potassium sodium niobate: A relationship with conduction mechanisms, Materials (Basel). 14 (2021). https://doi.org/10.3390/MA14051321.

[76] M.N. Rahaman, Ceramic Processing and Sintering, 1st ed., Marcel Dekker, Inc, New York, 1995. https://www.routledge.com/Ceramic-Processing-and-Sintering/Rahaman/p/book/9780824709884 (accessed August 13, 2021).

[77] A. Ndayishimiye, M.Y. Sengul, D. Akbarian, Z. Fan, K. Tsuji, S.H. Bang, A.C.T.

van Duin, C.A. Randall, Dynamics of the Chemically Driven Densification of Barium Titanate Using Molten Hydroxides, Nano Lett. 21 (2021) 3451–3457. https://doi.org/10.1021/acs.nanolett.1c00069.

[78] H. Birol, D. Damjanovic, N. Setter, Preparation and characterization of (K0.5Na0.5)NbO3 ceramics, J. Eur. Ceram. Soc. 26 (2006) 861–866. https://doi.org/10.1016/j.jeurceramsoc.2004.11.022.

[79] A. Scientific, Fast drying silver suspension from Agar, (n.d.). https://www.agarscientific.com/agar-fast-drying-silver-suspension (accessed August 31, 2021).

[80] P. Vilarinho, UC: Propriedades dos Materiais II, Aveiro, 2018.

[81] M.A. Rafiq, A. Tkach, M.E. Costa, P.M. Vilarinho, Defects and charge transport in Mn-doped K0.5Na0.5NbO3 ceramics, Phys. Chem. Chem. Phys. 17 (2015) 24403–24411. https://doi.org/10.1039/c5cp02883c.

[82] L. Jin, F. Li, S. Zhang, Decoding the fingerprint of ferroelectric loops: Comprehension of the material properties and structures, J. Am. Ceram. Soc. 97 (2014) 1–27. https://doi.org/10.1111/jace.12773.

Appendix 1